Development and application of synthetic turbulence methods for computational fluid dynamics

Dissertation
der Mathematisch-Naturwissenschaftlichen Fakultät
der Eberhard Karls Universität Tübingen
zur Erlangung des Grades eines
Doktors der Naturwissenschaften
(Dr. rer. nat.)

vorgelegt von
Dipl. Met. Torsten Auerswald
aus Leipzig

Tübingen
2017

Gedruckt mit Genehmigung der Mathematisch-Naturwissenschaftlichen Fakultät der Eberhard Karls Universität Tübingen.

Tag der mündlichen Qualifikation: 17.01.2018
Dekan: Prof. Dr. Wolfgang Rosenstiel
1. Berichterstatter: Prof. Dr. habil. Jens Bange
2. Berichterstatter: Prof. Dr. Rolf Radespiel

Contents

Acknowledgements v

Abstract vi

Zusammenfassung viii

List Of Publications x

1 Introduction 1

1.1 Numerical methods in Computational Fluid Dynamics 2

1.2 Synthetic turbulence 6

1.3 Objectives and outline of this thesis 8

2 Results 10

2.1 Generating 3D synthetic turbulence for initialising a Large-Eddy Simulation 11

2.2 Comparison of LES data from the atmospheric boundary layer with the synthetic turbulence method 15

2.3 Simulating the turbulent flow around a wing 19

2.4 An anisotropic synthetic turbulence method for Large-Eddy Simulation . 25

3 Discussion and outlook 34

A Publications 44

A.1 Large-Eddy Simulations of realistic atmospheric turbulence with the DLR-TAU-code initialized by in situ airborne measurements. 44

A.2 Comparison of two methods simulating highly resolved atmospheric turbulence data for study of stall effects 54

A.3 Evolution of turbulence in a simulation of the atmospheric boundary layer flow around a wing using synthetic turbulence. 65

A.4 An anisotropic synthetic turbulence method for Large-Eddy Simulation. . 94

Abbreviations

ABL	Atmospheric Boundary Layer
CBL	Convective Boundary Layer
CFD	Computational Fluid Dynamics
DES	Detached Eddy Simulation
DF-SEM	Divergence-Free Synthetic Eddy Method
DLR	German Aerospace Center
DNS	Direct Numerical Simulation
DVA	Disturbed Velocity Approach
LES	Large-Eddy Simulation
NS	Navier-Stokes
PALM	PArallelized Large-Eddy Simulation Model
PDF	Probability Density Function
RANS	Reynolds-Averaged Navier Stokes
RSM	Reynolds Stress Model
SBL	Stable Boundary Layer
SEM	Synthetic Eddy Method
TKE	Turbulence Kinetic Energy
URANS	Unsteady Reynolds-Averaged Navier Stokes

Symbols

δ	Channel half-height
$\Delta\lvert\vec{k}_{n,m,l}\rvert$	Interval of the absolute value of the wavenumber vector
Δk_x	Wavenumber interval in x-direction
$\Delta_{u_i u_j}$	Mean deviation of the absolute value of the components of the covariance
Δx	Grid spacing in x-direction
ν	Kolmogorov microscale
σ	Standard deviation
a_i	Signs of the spectral velocity
a_{ij}	Transformation matrix
c	Chord length
c_f	Skin friction coefficient
$\vec{C}_{n,m,l}$	Amplitude vector
E	Spectral energy per wavenumber interval
f	Frequency
i	Imaginary unit
$\vec{k}_{n,m,l}$	Wavenumber vector
K	Turbulence kinetic energy
l_{int}	Integral length scale
l_{ref}	Reference length
l_u	Integral length scale of the x-component of the velocity vector
l_v	Integral length scale of the y-component of the velocity vector
l_w	Integral length scale of the z-component of the velocity vector
L	Edge length of a cube
N	Total number of wavenumbers
R_{ij}	Correlation tensor
Re	Reynolds number
$\mathrm{Re}_{\mathrm{turb}}$	Reynolds number with respect to the friction velocity

S_i	Component of the 1D-model spectrum
t	Time
t^*	Dimensionless time
u	x-component of the velocity vector
$\tilde{u}_i$	Component of the spectral velocity vector
U	Reference velocity
v	y-component of the velocity vector
$\vec{v}$	Velocity vector
w	z-component of the velocity vector
$\vec{x}$	Position vector
y_1^+	Distance of the first wall-normal point
z_i	Boundary layer height
$Z_{n,m,l}$	Number of occurrence of the same absolute value of $\vec{k}$

Acknowledgements

I would like to thank everybody who supported me during the long journey my PhD project turned out to be. Especially, I would like to thank Prof. Jens Bange for his advice and help in all kinds of problems (scientifically and otherwise) that occurred during my work. Furthermore, I thank Prof. Rolf Radespiel for his support as the leader of the Research Unit FOR1066 and his valuable ideas and input. I also thank all my other colleagues from FOR1066 for their support.

Many thanks to my colleagues from the Airborne Meteorology group at TU Braunschweig and the Environmental Physics group at University of Tübingen: Jens, Aline, Sabrina, Yvonne, Thomas, Joe, Dani, Sridhar, Andy, Uwe, Asmae, Milad, Dave, Francesca and Norman. It was a lot of fun to work with you guys. I enjoyed your professional input as well as the good times we had during and after work. From the Institute of Aerodynamics and Flow Technology at the German Aerospace Center in Göttingen, I would like to thank Dr. Dieter Schwamborn for providing the opportunity to work in his group which was an important contribution to this thesis. Also, a special thanks to Axel, Silvia and Tobias for their support with the DLR-TAU code and their patience with my crazy simulations. From the University of Reading I would like to thank my colleague Denise for proof reading my thesis.

During the course of my PhD work I worked with two students, Patrick and Christina, who I would like to thank for their assistance.

Last but not least I would like to thank my family for their huge moral support during this whole endeavor and of course, Sonakshi for always being there for me, and patiently helping me through the frustrating times. Without you guys this project would have never been possible. Thank you!

Abstract

Synthetic turbulence methods are an important tool for the study of turbulent flows. They allow to reduce the computational effort of numerical simulations of fluid flows and thereby, improve the quality of simulations of complex flow problems. Contributing to the field of turbulence research, this thesis proposes two new methods of simulating turbulent flows using synthetic turbulence.

The methods developed in this work were tested for two scenarios of turbulent flow simulations. The first scenario was the numerical simulation of turbulent flow around a wing. For this simulation a synthetic turbulence method was developed, which generated an initial 3D turbulent wind field to initialise the simulation. Using a complex numerical setup it was possible to simulate the interaction of the synthetic turbulence field, representing atmospheric boundary layer (ABL) turbulence, with a wing on a relatively large range of scales. This method allows to simulate the influence of ABL turbulence on the aerodynamics of the wing, for example, at large angles of attack. In the second scenario a new method was developed to generate synthetic turbulence as inflow boundary condition for Large-Eddy Simulation (LES). A new method to generate anisotropy in the turbulence field was introduced, which allowed to prescribe 1D statistics of the turbulent flow independently. This method can be used, for example, for feeding synthetic turbulence into the interface between the Reynolds-Averaged Navier Stokes (RANS) and LES part of a hybrid RANS/LES.

For the first scenario, the generated turbulence was tested in a simple LES of decaying turbulence where it was found that the input statistics for the turbulence generator were reproduced very well. It was also shown that the statistical properties were maintained reasonably well during the simulation with the exception of fluctuations observed in the cross-correlations.

In order to investigate the quality of the turbulence generator further, the generated turbulence field was compared to data from an LES of the ABL. It was found that the synthetic turbulence was not able to represent the coherent structures present in a convective boundary layer, but apart from that the turbulence statistics from the synthetic turbulence and LES of the ABL agreed very well.

After studying the properties of the synthetic turbulence generator in detail, a synthetic turbulence field was generated for the initialisation of the simulation of the flow around a wing. In a complex setup of two different grid types (Cartesian and unstructured) and two different turbulence model types (LES and RANS), the development of the turbulence in the different numerical environments was studied. It was found that the change in grid characteristics led to a stronger dissipation of turbulence on the unstructured grid. No significant effect on the turbulence could be found when the turbulence model switched from LES to RANS mode, most likely due to the short time the turbulence was exposed to the RANS model.

For the second scenario, a new approach for generating anisotropic turbulence was developed. An extensive analysis of the statistics of the generated turbulence was carried out and the results showed very good agreement with the reference data from a Direct Numerical Simulation (DNS). The generated turbulence then served as inflow boundary condition in an LES of a channel flow. A strong influence of the statistical properties of the synthetic turbulence on the behaviour of the turbulence in the channel was found. Comparison to two established synthetic turbulence methods showed a similar performance of the new approach, which at the same time caused much less computational costs and allowed better control of the statistical parameters of the synthetic turbulence.

Zusammenfassung

Methoden zur Erzeugung synthetischer Turbulenz sind wichtige Werkzeuge bei der Simulation turbulenter Strömungen. Mit ihrer Hilfe ist es möglich, den Rechenaufwand numerischer Simulationen von turbulenten Strömungen zu verringern und dadurch die Qualität von Simulationen komplexer Strömungsprobleme zu verbessern. Die vorliegende Arbeit leistet einen Beitrag zu diesem Forschungsgebiet, indem zwei neue Methoden zur Simulation turbulenter Strömungen mit Hilfe von synthetischer Turbulenz vorgestellt werden.

Die in dieser Arbeit präsentierten Methoden wurden anhand zweier Anwendungsfälle getestet. Der erste Fall ist die numerische Simulation der turbulenten Umströmung eines Tragflügels. Hierfür wurde eine Methode zur Erzeugung synthetischer Turbulenz entwickelt, die ein turbulentes 3D-Strömungsfeld generiert, welches zur Initialisierung der Simulation verwendet wurde. Mit Hilfe eines komplexen numerischen Modells war es möglich, die Wechselwirkung zwischen dem Turbulenzfeld und einem Tragflügel in der atmosphärischen Grenzschicht für einen relativ großen Bereich turbulenter Skalen zu simulieren. Diese Methode erlaubt es den Einfluss von Grenzschichtturbulenz auf einen Tragflügel, z.B bei großen Anstellwinkeln, zu simulieren. Für den zweiten Anwendungsfall wurde eine neue Methode entwickelt, um synthetische Turbulenz als Einströmrandbedingung für eine Grobstruktursimulation (LES) zu generieren. Diese Methode ist in der Lage, anisotrope Turbulenzfelder zu erzeugen und dabei verschieden Parameter der 1D-Turbulenzstatistik unabhängig voneinander zu realisieren. Anwendung kann solch eine Methode z.B. im Übergangsbereich zwischen einer Reynolds-Averaged Navier Stokes (RANS) Rechnung und einer LES in einer hybriden RANS/LES finden.

Für den ersten Anwendungsfall wurde die generierte synthetische Turbulenz in einer einfachen LES-Rechnung zerfallender Turbulenz getestet. Dabei konnte gezeigt werden, dass die vorgegebene Turbulenzstatistik vom Turbulenzgenerator sehr gut wiedergegeben wurde. Die LES der zerfallenden Turbulenz hat auch gezeigt, dass die Turbulenzstatistik während der Simulation relativ gut erhalten blieb (mit Ausnahme von Fluktuationen in den Kreuzkorrelationen).

Um die Qualität der erzeugten synthetischen Turbulenz besser beurteilen zu können, wurden die synthetischen Turbulenzfelder mit Daten einer LES der atmosphärischen

Grenzschicht verglichen. Dabei zeigte sich, dass die synthetische Turbulenz die kohärenten Strukturen, die typischerweise in der konvektiven Grenzschicht vorhanden sind, nicht reproduzieren kann. Ansonsten konnte aber eine gute Übereinstimmung zwischen den Statistiken der synthetischen Turbulenz und der LES festgestellt werden.

Nachdem die Eigenschaften der synthetischen Turbulenz ausführlich untersucht wurden, wurde ein synthetisches Turbulenzfeld als Anfangsfeld für die Simulation der turbulenten Umströmung eines Tragflügels generiert. Unter Verwendung einer Kombination aus zwei verschiedenen Gittertypen (kartesisch und unstrukturiert) und zwei verschiedenen Turbulenzmodelltypen (LES und RANS) wurde die Entwicklung der turbulenten Strömung in den verschiedenen Bereichen untersucht. Dabei wurde gezeigt, dass beim Wechsel vom kartesischen zum unstrukturierten Gitter die numerische Dissipation deutlich zunahm. Allerdings konnte in diesem Anwendungsfall kein signifikanter Einfluss auf die Turbulenz beim Wechsel von LES auf RANS festgestellt werden, da hier die Zeit, in der die turbulente Strömung dem RANS-Modell ausgesetzt war, zu kurz war.

Für den zweiten Anwendungsfall wurde ein neuer Ansatz zum Erzeugen anisotroper synthetischer Turbulenz entwickelt. In einer ausführliche Analyse konnte gezeigt werden, dass die Statistik der synthetischen Turbulenz gut mit der Referenzstatistik aus einer direkten numerischen Simulation (DNS) übereinstimmt. Anschließend wurde der Turbulenzgenerator als Einströmrandbedingung in einer LES einer Kanalströmung eingesetzt. Dabei wurde ein starker Einfluss der statistischen Eigenschaften der synthetischen Turbulenz auf das Verhalten der turbulenten Strömung im Kanal festgestellt. In einem Vergleich mit zwei etablierten Methoden zur Erzeugung synthetischer Turbulenz, konnte die neue Methode vergleichbare Ergebnisse erzielen, hat dabei allerdings deutlich weniger Rechenzeit benötigt und eine bessere Kontrolle der generierten Turbulenzstatistik erlaubt.

List Of Publications

This thesis is presented as an integrated accumulation of four scientific publications. The first three manuscripts have been published in peer-reviewed journals and the fourth one has been submitted for publication to a peer-reviewed journal.

Published manuscript

- **Auerswald, T.**, **Bange, J.** and **Knopp, T.** and **Weinman, K.** and **Radespiel, R.**, **2010**: Large-Eddy Simulations of realistic atmospheric turbulence with the DLR-TAU-code initialized by in situ airborne measurements. *Computers & Fluids*, **66**, 121–129.
- **Knigge, C.**, **Auerswald, T.** and **Raasch, S.** and **Bange, J.**, **2015**: Comparison of two methods simulating highly resolved atmospheric turbulence data for study of stall effects. *Computers & Fluids*, **108**, 57–66.
- **Auerswald, T.**, **Probst, A.** and **Bange, J.**, **2016**: An anisotropic synthetic turbulence method for Large-Eddy Simulation. *Int. J. of Heat and Fluid Flow*, **62**, 407–422.

Submitted manuscript

- **Auerswald, T.** and **Bange, J.**, **2017**: Evolution of turbulence in a simulation of the atmospheric boundary layer flow around a wing using synthetic turbulence. *Journal of Wind Engineering and Industrial Aerodynamics*, under review.

Other publications not included in the thesis

- **Chlond, A.**, **Böhringer, O.** and **Auerswald, T.** and **Müller, F.**, **2014**: The effect of soil moisture and atmospheric conditions on the development of shallow cumulus convection: A coupled large-eddy simulation-land surface model study. *Meteorologische Zeitschrift*, **23**, 491–510.

Conference contributions

- **Auerswald, T.** and **Bange, J.**, Methode zum Generieren dreidimensionaler turbulenter Windfelder für Large-Eddy Simulationen. In *DACH Tagung*, Hamburg, Germany, 10 – 14 September **2007**.

- **Auerswald, T.** and **Bange, J.**, Generation of a three-dimensional turbulent initial wind field for large-eddy simulation. In *7th European Meteorological Society Annual Meeting*, San Lorenzo de El Escorial, Spain, 1 – 5 October **2007**.

- **Auerswald, T.** and **Bange, J.**, Generation of a three-dimensional turbulent initial wind field for large-eddy simulation. In *Joint Symposium of DFG PAK 136 and DLR Airbus $C^2A^2S^2E$: ”Simulation of Wing and Nacelle Stall”*, Braunschweig, Germany, 18 - 19 June **2008**

- **Auerswald, T.** and **Bange, J.**, Comparison of Synthetic Turbulent Wind Fields with Large-Eddy Simulation of the Atmospheric Boundary Layer. In *9th European Meteorological Society Annual Meeting*, Toulouse, France, 28 September - 2 October **2009**

- **Auerswald, T.** and **Bange, J.**,. Comparison of High-Resolution Large-Eddy Simulation and Synthetic Turbulent Wind Fields. In *48th AIAA Aerospace Sciences Meeting*, Orlando, USA, 4 - 7 January **2010**

- **Auerswald, T.** and **Bange, J.**, Large-Eddy Simulation of realistic atmospheric turbulence with the DLR TAU-code initialised by in-situ airborne measurements. In *Joint Symposium of DFG FOR 1066 and DLR-Airbus $C^2A^2S^2E$: ”Simulation of Wing and Nacelle Stall”*, Braunschweig, Germany, 22 - 23 June **2010**

- **Auerswald, T.** and **Bange, J.**, Large-Eddy Simulation of the atmospheric boundary layer initialised with synthetic turbulence. In *19th Symposium on Boundary Layers and Turbulence*, Keystone, USA, 2 - 6 August **2010**

- **Auerswald, T.** and **Bange, J.**, Simulating the turbulent flow around an airfoil. In *Workshop of the Network of Airborne Environmental Research Scientists*, Garmisch-Partenkirchen, Germany, 14 - 16 February **2012**

- **Auerswald, T.** and **Bange, J.**, Numerical Simulation of the Turbulent Flow Around a Wing. In *Joint Symposium of DFG FOR 1066 and DLR-Airbus $C^2A^2S^2E$: ”Simulation of Wing and Nacelle Stall”*, Braunschweig, Germany, 21 - 22 June **2012**

- **Radespiel, R.**, **Francois, D.-G.**, **Hoppmann, D.**, **Klein, S.**, **Scholz, P.**, **Wawrzinek, K.**, **Lutz, T.**, **Auerswald, T.**, **Bange, J.**, **Knigge, C.**, **Raasch, S.**, **Kelleners, P.**, **Heinrich, R.**, **Reuß, S.**, **Probst, A.** and **Knopp, T.**, Simulation of Wing Stall. In *43rd AIAA Fluid Dynamics Conference*, San Diego, USA, 24 - 27 June **2013**

- **Auerswald, T.** and **Bange, J.**, Numerical Simulation of the Turbulent Flow Around a Wing. In *European Geosciences Union General Assembly*, Vienna, Austria, 27 April - 2 May **2014**

- **Auerswald, T.** and **Bange, J.**, Numerical Simulation of the Turbulent Flow Around a Wing. In *21st Symposium on Boundary Layers and Turbulence*, Leeds, UK, 9 - 13 June **2014**

- **Auerswald, T.** and **Bange, J.**, Numerical Simulation of the Turbulent Flow Around a Wing. In *Joint Symposium of DFG FOR 1066 and DLR-Airbus $C^2A^2S^2E$: ”Simulation of Wing and Nacelle Stall”*, Braunschweig, Germany 1 -2 December **2014**

1 Introduction

Turbulence is a property of fluid flows which is characterised by chaotic fluctuations and is effective on a large range of scales. In the atmosphere, for example, turbulence controls the fluxes of sensible heat, latent heat and momentum between the Earth's surface and the atmosphere. These turbulent fluxes are several orders of magnitude larger than the fluxes caused by molecular diffusion, which is why they are fundamental for many atmospheric processes and in consequence, for our weather and climate. Turbulence plays a key role not only in meteorology but also in many other fields of natural science and engineering. For example, there are studies on the deposition of aerosols in turbulent flows which helps e.g. improving the drug delivery to the lungs (Crowder *et al.*, 2002). In microbial suspensions, the self-propulsion and mutual interaction of microorganisms is affecting turbulence which in turn affects e.g. the mixing of nutrients (Wensink *et al.*, 2012). In engineering, turbulent flows are affecting the efficiency of sophisticated filter systems in coal plants (Ahmadi and Smith, 1998) or the combustion process in fuel engines (Zhang *et al.*, 2005). In wind farms noise is generated predominantly due to the interaction of the trailing edge of the turbine blades with their turbulent boundary layer. Using active flow control the turbulent boundary layer features can be manipulated in order to reduce the generated noise (Wolf *et al.*, 2015). It is clear from this short and non-exhaustive list, that proper understanding of turbulence is crucial when studying flows in a large variety of scientific fields.

Mathematically, the behaviour of fluids can be described by the Navier-Stokes (NS) equations (e.g. Davidson, 2015). This set of differential equations can be used to describe the balance of forces in a fluid and therefore, allows to predict the future behaviour of a fluid. Unfortunately, until today, the NS equations cannot be solved analytically for most applications. So far, the only way to solve the NS equations for most applications is by applying numerical methods. For the numerical solving of the NS equations, the differentials in the equations are transformed to differences leading to an approximation of the solution for a discrete space and time and therefore, can be calculated using computers. The analysis of fluid flows using numerical computation is called Computational Fluid Dynamics (CFD).

Since the first numerical weather forecast, published by Richardson (1922), enormous progress has been made in both accuracy and speed of numerical simulations of fluid flows. It took Richardson 6 weeks to calculate a 6 hour forecast for Europe. He estimated that, using a time step of 3 hours, 32 human computers (people who compute the model solution by hand) would be needed to calculate the weather in real time (meaning the time in the numerical computation would progress at the same speed as the real time). For his weather model 64000 human computers would have been needed to compute a global forecast in real time. Today global weather forecasts are performed within a few hours for forecasting periods of several days. This has been made possible by the introduction of super computers and the rapid increase in their computational performance. One of the first super computers, the Atlas from 1962 was able to perform one million operations per second. The fastest super computer today, the Tianhe-2 from the National Super Computer Center in Guangzhou in China, is able to perform 10^{15} floating point operations per second. Despite this incredible increase in computer performance, CFD still relies on simplifications and parameterisations. The turbulent flows in most applications cover such a wide range of scales that today's computers are not powerful enough to fully resolve those turbulent scales.

1.1 Numerical methods in Computational Fluid Dynamics

A number of methods have been proposed in order to simulate turbulent flows despite the lack of computational power. A very popular method is based on the Reynolds-Averaged Navier Stokes (RANS) equations. Already in 1895, Osborne Reynolds developed the Reynolds-averaging method, in which a time-dependent quantity is split into a mean and the deviation of that mean (Reynolds, 1895). In the same publication he applied this averaging method to the NS equations, which led him to the now famous RANS equations. These equations are a set of differential equations for the time-averaged flow where the influence of the turbulence is entirely represented by the Reynolds stress term. All time dependency is removed by the averaging process. Therefore, the RANS equations describe a stationary process. To solve these equations, a formulation for the Reynolds stress tensor has to be found. For the application of the RANS equations in CFD, RANS turbulence models were developed (e.g. Spalart and Allmaras, 1992) which estimate the Reynolds stress term, and thereby, the interaction of turbulence with the mean flow, by using the averaged quantities of the flow. This method is much faster than solving the full unaveraged NS equations. Since turbulence is parameterised and not explicitly resolved, coarser time steps and spatial resolutions can be applied. In order to simulate unsteady flows, the unsteady RANS (URANS) method introduces two time scales, the turbulent and the mean flow time scale. It is assumed that the turbulent time scale is much smaller than the mean flow time scale (which is not the case in all applications). Then the Reynolds-averaging is only applied on the time interval representing the turbulent time scale and therefore, provides an unsteady solution for the mean flow. Until today RANS and URANS are popular tools for simulating flows when an explicit resolution of turbulence is not necessary or possible (e.g. Lyu and Martins, 2013, Wu *et al.*, 2016, Mannini *et al.*, 2010).

In 1970, computer performance had increased so much that simulations became possible in which a part of the turbulence spectrum could be resolved explicitly. The so called Large-Eddy Simulation (LES), first applied by Deardorff (1970), uses spatially averaged Navier-Stokes equations on a grid and with a timestep, fine enough to resolve the largest scales of the turbulent flow. The turbulence models for LES only account for the part of the turbulence which cannot be resolved explicitly by the grid (Smagorinsky, 1963). Since the largest scales of the turbulence carry the most energy, turbulent effects can be simulated much better with LES than RANS or URANS. This method is used, for example, for simulating the flow inside cities (Chung and Liu, 2013, Letzel *et al.*, 2012) which can help architects and city planners to improve the air quality in a city. In aerospace engineering LES is used, for example, to study the flow around airfoils (Lehmkuhl *et al.*, 2013) or to simulate the heat transfer between cooling ducts and blades in gas turbines (Tyacke and Tucker, 2015). Many more applications prove LES to be a powerful tool when studying all kinds of turbulent flows.

Another method for solving the NS equations numerically is to avoid parameterising turbulence altogether. This can be achieved by using grid resolutions so high that the turbulence can be resolved explicitly on all scales. This method is called Direct Numerical Simulation (DNS) and requires to resolve the whole spectrum of turbulent scales from the energy containing range down to the dissipation range. First attempts towards DNS were made as early as 1972 (Orszag, 1972). In this work isotropic turbulence with a microscale Reynolds number (the Reynolds number with respect to the Kolmogorov microscale) of 35 was simulated on a cube with 32^3 grid points using DNS.

The size of the smallest eddies in a turbulent flow (represented by the Kolmogorov microscale ν) is related to the Reynolds number as:

$$\nu = \mathrm{Re}^{-3/4} l_{\mathrm{int}}, \tag{1}$$

where Re is the Reynolds number and l_{int} is the integral length scale, representing the largest scales of the turbulent flow. Therefore, the larger the Reynolds number of a flow, the smaller the size of the smallest eddies. This means that for the simulation of a flow with high Reynolds numbers, a very fine resolution is needed (which is the case for many turbulent flows of interest in applied physics). DNS provides the most accurate solution of the NS equations. Unfortunately, today's computers are still not powerful enough to apply this technique for most real flows. Since the first DNS in 1972 the maximum microscale Reynolds number achieved in DNS has approximately doubled each decade (Davidson, 2015). Reynolds numbers in the atmospheric boundary layer (ABL), for example, can reach 10^8 or more, values far out of reach for today's DNS. Therefore, DNS is a very useful tool mainly for fundamental turbulence research (e.g. Coceal *et al.*, 2014, Druzhinin and Ostrovsky, 2015, Poroseva *et al.*, 2015, Bouali *et al.*, 2016).

Fig. 1 visualises the differences between the three methods described above. It shows the vorticity field in the simulation of flow around an infinitely long cylinder for DNS (a), LES (b) and RANS (c). For the DNS, detailed structures of eddies in the wake of the cylinder are visible, while in the LES less detail and only large structures can be seen. In the RANS simulation no turbulent structures are visible in the wake of the cylinder and only the stationary shear layers at the sides are visible. All the turbulent structures missing in the LES and RANS simulation (compared to the DNS) have to be modelled by the respective turbulence models. Since the properties of turbulence can be very different depending on the scenario (different Reynolds numbers, stratifications, turbulence statistics etc.), this can only be achieved approximately.

In order to combine the advantages of URANS (computationally efficient) and LES (resolves parts of the turbulence explicitly), a hybrid URANS/LES method called Detached Eddy Simulation (DES) was first proposed by Spalart *et al.*, 1997. In DES parts of the flow which are known to be well predicted by URANS (like attached boundary layers) are simulated with URANS, while in regions where large eddies occur, the flow is simulated using LES (e.g. where massive separation occurs). In that way the costs of the simulation can be reduced significantly, while still having the advantages of an LES in

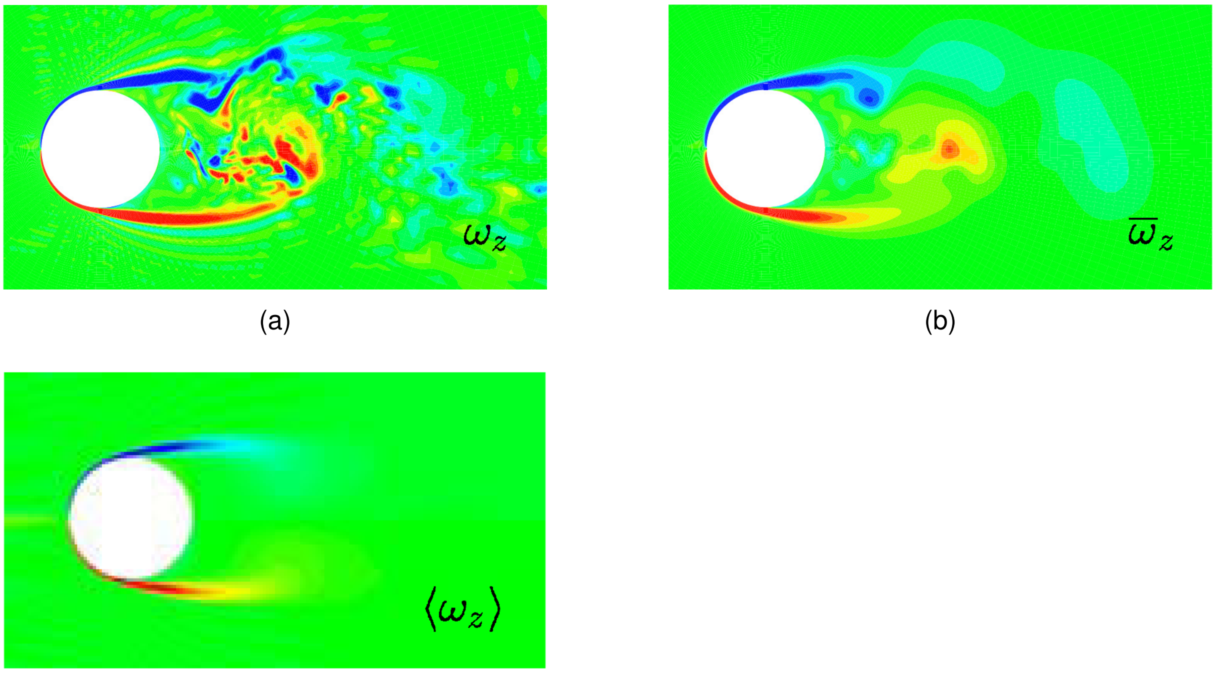

(a)

(b)

(c)

Figure 1: *Vorticity field for the flow around an infinitely long cylinder as simulated with DNS (a), LES (b) and RANS (c), taken from Froehlich (2006).*

the relevant part of the flow. The switching between URANS and LES model is either done during the simulation by evaluating e.g. length scales of the turbulence and the grid spacing, or the URANS and LES parts of the domain are defined a priori based on previous experience. Using DES it is possible to study high-Reynolds number, massively separated flows, which is e.g. important in aerodynamics of cars and airplanes (Spalart, 2009, Deck *et al.*, 2014).

A problem that arises in DES is that in the flow entering the LES domain from the URANS domain, turbulence information is missing. Since the RANS models are designed to account for the complete turbulent spectrum, only the mean flow is resolved in the URANS domain. Therefore, the development of resolved turbulence in the LES domain is often delayed, leading to unrealistic results. In order to improve simulation results in DES, synthetic turbulence can be injected at the interface region between the URANS and LES domain. This synthetic turbulence is an artificial random signal constructed to contain certain statistical features of realistic turbulence. In DES applications input statistics for synthetic turbulence are provided by the RANS turbulence model.

1.2 Synthetic turbulence

In an LES of turbulent flow it is often the case that it takes a long time for turbulence to develop from a non-turbulent initial state. Therefore, several methods have been proposed for speeding up the development of turbulence. One approach is to make use of periodic boundary conditions in order to provide inflow data for the model domain (Spalart and Watmuff, 1993). This allows to reduce the domain size and thereby, save computation time. However, corrections have to be applied in the case of spatially developing boundary layers and the method is only applicable in relatively simple scenarios like a fully developed channel flow.

Another approach is to run a precursor simulation in which a turbulence field develops and use that field at the inflow boundary of the original simulation (Piomelli *et al.*, 2000). This method has the advantage that it provides a turbulence field which is in agreement with the physics of the flow solver and can be reused for many simulations. However, it is often too expensive to run a precursor simulation and in cases such as hybrid URANS/LES it is not applicable at all.

As an alternative to the methods mentioned above, in this thesis the method of synthetic turbulence is used. The main goal of synthetic turbulence methods is to reduce the amount of simulation time needed for realistic turbulence to develop inside the LES domain. This is achieved by replacing the simulation of the development of turbulence by the generation of synthetic turbulence. Since synthetic turbulence is not produced by the computationally expensive solving of the NS equations, but by statistical algorithms, computation time can be saved and complex problems can be solved using less resources. Synthetic turbulence methods produce random fields with certain statistical properties in order to either reduce the amount of simulated time or the domain size necessary to study a certain phenomenon (an extensive overview over initialisation methods in general can be found in Keating *et al.*, 2004).

First efforts towards synthetic turbulence were made for the simulation of diffusion processes by random fields (Kraichnan, 1970, Khan *et al.*, 2003) where the random field was generated using random Fourier modes with a given energy spectrum. Later, studies were carried out where synthetic turbulence was used to simulate the dispersion of particles in a turbulent flow by simulating the flow with URANS. The diffusion process was simulated by applying the synthetic turbulence to the trajectories of the particles in the flow (Li and Ahmadi, 1995, Ahmadi and Smith, 1998). In LES, synthetic turbulence can be used as inflow boundary condition or as initial solution of the flow. In Polacsek *et al.* (2011), for example, synthetic turbulence was used in an aeroacoustic study to investigate the reduction of noise produced by an airfoil using hybrid URANS/LES. Troldborg *et al.* (2007) generated synthetic turbulence to superimpose it to the mean flow and study the effects of ABL turbulence on a wind turbine. And in Petronio *et al.* (2013) an LES of the ocean flow in a bay area was performed where turbulence development inside the LES domain was triggered by synthetic turbulence.

Several methods for generating synthetic turbulence have been proposed in the past. Methodologies include the generation of random noise which is filtered in such a way that given correlations are reproduced (Klein *et al.*, 2003). Instead of filtering, Kempf *et al.* (2005) applied a diffusion process to white noise in order to produce turbulence with given length scales. This method has the advantage that it can also be used on unstructured grids and is therefore available for a large variety of applications.

A very common approach is the superposition of Fourier modes whose amplitudes are designed in such a way that they reproduce a given power spectrum. Performing an inverse Fourier transform on the spectral field results in a turbulence field with the given spectral distribution of energy (Smirnov *et al.*, 2001, Batten *et al.*, 2004, Batten *et al.*, 2012, Adamian and Travin, 2011).

An algorithm that follows a very different approach is the synthetic-eddy method (SEM) by Jarrin *et al.* (2006) and the related divergence-free SEM (DF-SEM) by Poletto *et al.* (2011). Both approaches use shape functions to construct eddies geometrically in space, to match given autocorrelation functions and Reynolds stresses.

Depending on the method, further steps can be taken to modify the synthetic turbulence field to yield more realistic results. Common to most methods is that they generate proper one-point correlations by applying the Cholesky decomposition to the turbulent velocity field (e.g. Lund *et al.*, 1998, Batten *et al.*, 2012 and Jarrin *et al.*, 2006). This approach calculates a transformation matrix based on the given correlation matrix which is applied to each vector in the vector field. In consequence, each vector is transformed in such a way that the given correlations are met.

1.3 Objectives and outline of this thesis

The main objective of this thesis was to develop and test synthetic turbulence methods for the following two scenarios.

Scenario 1: Simulation of the turbulent ABL flow around a wing

In the first scenario a method to simulate the turbulent ABL flow around a wing was developed. The only other method which has investigated the interaction of ABL turbulence with a wing in a numerical simulations was published by Kelleners and Heinrich (2015). In their study two approaches for simulating the turbulent flow around a wing were presented. The first was the disturbed velocity approach (DVA; Heinrich, 2014), which allows to simulate the influence of turbulence on a wing with little computational costs. The disadvantage of this approach is that the development of the turbulence field in time is not calculated. Furthermore, the feedback from the wing on the turbulent flow cannot be taken into account. The second approach made use of LES data from a simulation of the complete ABL. This approach is very precise since high resolution LES data from a simulation of the complete ABL is used. However, computationally it is very expensive to run a simulation which develops a realistic ABL before feeding the turbulence into the flow solver. Therefore, in this thesis, an alternative approach was used. It falls in between the two approaches suggested by Kelleners and Heinrich (2015) in terms of computational effort and accuracy of the simulation. The present approach is computationally more expensive than the DVA, but is able to simulate the temporal behaviour of turbulence and the feedback of the wing on the turbulent flow. In comparison to the approach using the LES of the whole ABL, it is much cheaper but is only using an approximation of ABL turbulence generated by a synthetic turbulence method. This approach aims at allowing to study several different ABL scenarios with much less computational effort. This goal was achieved in the following way:

- Development of a Fourier method for the initialisation of a 3D turbulence field which possesses prescribed statistics of an ABL flow (Sec. A.1). It was used in an LES of decaying turbulence to demonstrate the general applicability of the method.
- Comparison between LES data from the ABL and the synthetic turbulence in

order to investigate the quality of the generated turbulence (Sec. A.2).

- Application of the synthetic turbulence method in the simulation of the turbulent ABL flow around a wing using hybrid URANS/LES (Sec. A.3).

Scenario 2: An anisotropic synthetic turbulence method for LES

In the second scenario a novel approach for generating anisotropic synthetic turbulence as inlet boundary condition for LES is presented (Sec. A.4). It was shown that the Cholesky method creates a sometimes unwanted side effect. It modifies the 1D statistics of the generated field. In cases of inhomogeneous turbulence this can be disadvantageous. An alternative approach was developed that overcomes these negative effects and allows to prescribe turbulence properties independently. The performance of the method was demonstrated using the test case of an LES of a turbulent channel flow and the results were compared to the SEM and DF-SEM.

2 Results

In this section an overview over the most important findings of the following papers is presented (the full papers are attached in Sections A.1 to A.4):

- Section A.1:
  Auerswald, T., **Bange, J.**, **Knopp, T.**, **Weinman, K.** and **Radespiel, R.**, **2010**: Large-Eddy Simulations of realistic atmospheric turbulence with the DLR-TAU-code initialized by in situ airborne measurements. *Computers & Fluids*, **66**, 121–129.

- Section A.2:
  Knigge, C., **Auerswald, T.**, **Raasch, S.** and **Bange, J.**, **2015**: Comparison of two methods simulating highly resolved atmospheric turbulence data for study of stall effects. *Computers & Fluids*, **108**, 57–66.

- Section A.3:
  Auerswald, T. and **Bange, J.**, **2016**: Evolution of turbulence in a simulation of the atmospheric boundary layer flow around a wing using synthetic turbulence. *Journal of Wind Engineering and Industrial Aerodynamics*, under review.

- Section A.4:
  Auerswald, T., **Probst, A.** and **Bange, J.**, **2016**: An anisotropic synthetic turbulence method for Large-Eddy Simulation. *Int. J. of Heat and Fluid Flow*, **62**, 407–422.

In the papers in sec. A.1 to A.3 a methodology to simulate the turbulent ABL flow around a wing was developed and tested. First the synthetic turbulence generator for initialising the simulation with a turbulent flow and a simple test scenario is presented in A.1. The turbulence fields generated by this method are then compared to LES data of the ABL in A.2. In A.3 the application of that method inside the simulation of the flow around a wing is presented. Sec. A.4 describes a novel synthetic turbulence generator method which serves as inflow boundary condition for LES and investigates its performance. A detailed summary of the four papers is given in the following subsections.

2.1 Generating 3D synthetic turbulence for initialising a Large-Eddy Simulation

For the simulation of the turbulent ABL flow around a wing, presented in Sec. A.3, an initial turbulent wind field was needed. Simulating the development of the complete ABL as part of the simulation of the flow around the wing was unrealistic given the limitations of available computational resources. Likewise, a standalone simulation of the whole ABL to generate an initial turbulence field for the simulation around the wing, would have been too expensive and is in general not practical, for example, if several different weather scenarios need to be studied. Therefore, a method to generate a three-dimensional turbulent wind field for initialising the simulation was developed. This method is presented in the paper in Sec. A.1 and is summarised in this section. The method developed makes use of measurements from the ABL taken by the Helipod system (Bange *et al.*, 2007) which provides high-resolution data for different weather scenarios. However, the measurement data consisted of 1D-timeseries of the wind field. Therefore, this data could not be used directly, but instead the turbulence statistics from the measurements were used as input for the synthetic turbulence generator, which produced a three-dimensional turbulent wind field containing the measured statistics.

The core equation of the turbulence generator is a three-dimensional Fourier series which is a sum over waves with different wavenumbers and amplitudes that creates a velocity field with a given power spectrum:

$$\vec{v}(\vec{x}) = \sum_{n=1}^{N} \sum_{m=1}^{N} \sum_{l=1}^{N} \Big(\vec{C}_{n,m,l} \big(\cos(2\pi \cdot \vec{k}_{n,m,l} \cdot \vec{x}) + i \sin(2\pi \cdot \vec{k}_{n,m,l} \cdot \vec{x}) \big) \Big), \qquad (2)$$

where $\vec{v}$ is the velocity vector, $\vec{x}$ is the position vector, N is the total number of wavenumbers in every direction of the wavenumber space, $\vec{k}_{n,m,l}$ are the wavenumber vectors and $\vec{C}_{n,m,l}$ the complex amplitude vectors.

The resulting velocity field is divergence-free, isotropic and represents the measured energy spectrum E by defining the amplitudes of the Fourier modes according to:

$$|\vec{C}_{n,m,l}| = \sqrt{\frac{1}{Z_{n,m,l}} \cdot E(|\vec{k}_{n,m,l}|) \cdot \Delta|\vec{k}_{n,m,l}|}, \qquad (3)$$

where $Z_{n,m,l}$ is the number of occurrence of the same absolute values of $\vec{k}_{n,m,l}$ for all given combinations of n, m and l and $\Delta|\vec{k}_{n,m,l}|$ is the interval of the absolute value of $\vec{k}$. The measured correlations can be reproduced by applying the Cholesky decomposition which applies a transformation matrix a_{ij} to the isotropic turbulence field:

$$v(\vec{x})_i^{\text{aniso}} = a_{ij} \cdot v(\vec{x})_j^{\text{iso}}. \tag{4}$$

The transformation matrix a is defined as:

$$a = \begin{pmatrix} \sqrt{R_{11}} & 0 & 0 \\ R_{21}/a_{11} & \sqrt{R_{22} - a_{21}^2} & 0 \\ R_{31}/a_{11} & (R_{32} - a_{21}a_{31})/a_{22} & \sqrt{R_{33} - a_{31}^2 - a_{32}^2} \end{pmatrix}, \tag{5}$$

where R_{ij} is the given correlation tensor, for example obtainable from measurements, that is imposed on the velocity field. The correlations of the resulting velocity field v_i^{aniso} are equal to R_{ij}.

When initialising an LES with the velocity field described above, an initial state for the density and pressure needs to be prescribed as well. In this work a simple assumption was used based on the Bernoulli equations which gives a relationship between velocity field and density or pressure.

The measurement data for the initialisation were taken from a convective boundary layer case measured by the Helipod during the LITFASS03 campaign in Lindenberg, Germany on June, 2nd in 2003. The simulation was performed using the CFD solver DLR-TAU (Schwamborn *et al.*, 2006), developed by the German Aerospace Center (DLR). It used a k-ω LES model to model the subgrid scale turbulence. The simulated time was 3 s which corresponds to the anticipated time it would take the wing to fly through the turbulence field in the simulation of the turbulent flow around the wing in Sec. A.3. The development of turbulence in the LES was investigated in order to understand the behaviour that is to be expected in the simulation of the turbulent flow around the wing.

Fig. 2 shows the power spectrum normalised by the reference velocity U and the reference length l_{ref} at time $t = 0$ s and $t = 3$ s (for this simulation the reference velocity was equal to the standard deviation of the initial turbulent velocity field $\sigma = 1.50$ m/s and the reference length was equal to the side length of the cubic domain $L = 349.26$ m). It can be seen that after 3 s the power spectrum is shifted towards lower energies over the whole wavenumber range. This is caused by the absence of any source for turbulence

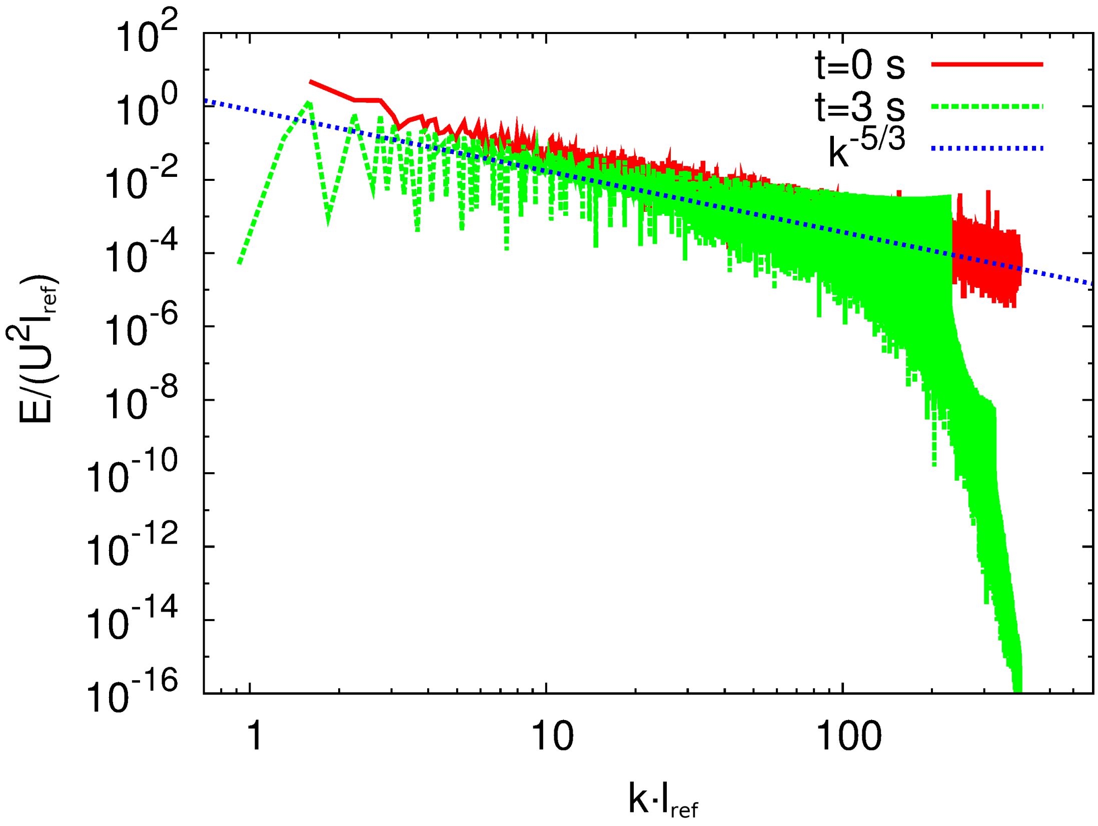

Figure 2: *Normalised energy spectra of turbulence in the simulations with DLR-TAU. Depicted is the spectrum of the initial wind field (red line) and after 3 seconds simulation time (green, dashed). For comparison the $k^{-5/3}$ slope is included (blue, dotted).*

energy, leading to a decay of turbulence energy during the simulation. Additionally, a strong energy drop-off can be seen in the small scales. This drop caused by the numerical dissipation of the flow solver ranges from the smallest resolvable scale to around 4 times the grid spacing ($\Delta x/l_{\text{ref}} = 0.002$). Scales larger than that were preserved very well as well as the $k^{-5/3}$ slope, typical to the inertial subrange of the turbulence spectrum. In the wavenumber range between 40 and 200 the energy spectrum exhibits local maxima at constant energy levels which are due to the low artificial dissipation chosen in this simulation. This was necessary in order to preserve the small scale turbulence energy as much as possible. Since one important property of atmospheric turbulence is the wide range of scales, this trade-off had to be made.

In Fig. 3 the longitudinal probability density function (PDF) of the increments of the x-component of velocity (normalised by the reference velocity) is shown for times $t = 0$ s

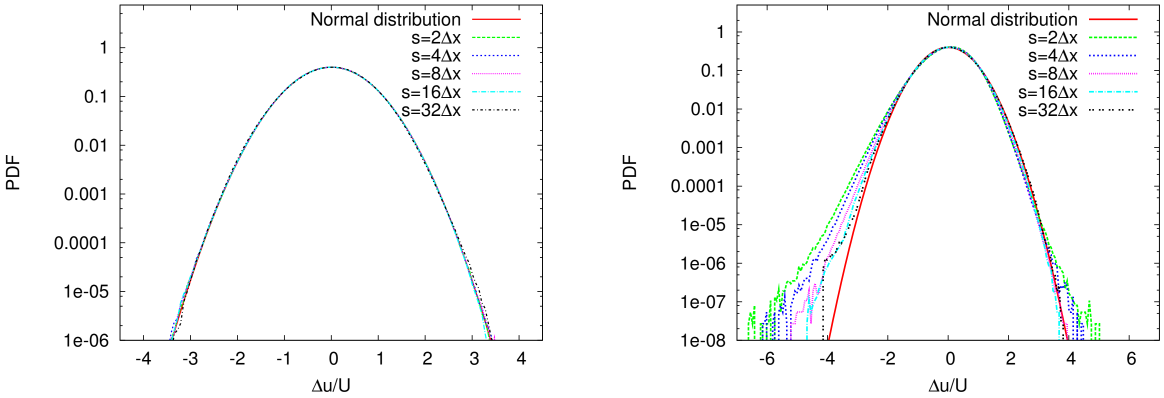

Figure 3: *Normalised longitudinal PDF of the increments of the x-component of the velocity (normalised by the reference velocity) calculated from the initial wind field (left) and the DLR-TAU result after 3 s (right) for separation distances s=$2\Delta x$ (green), s=$4\Delta x$ (blue), s=$8\Delta x$ (purple), s=$16\Delta x$ (light blue) and s=$32\Delta x$ (black). For comparison the PDF of the normal distribution is plotted in red.*

(left) and $t = 3$ s (right). The PDF of the difference of the velocity over a certain separation distance gives insight into the intermittency of the turbulent flow (Sreenivasan, 1999). Intermittent events are bursts in the turbulent flow which create a sudden and relatively strong change in the turbulence signal. Because of that the PDF of the increments of the velocity shows tails at the left and right end of the distribution compared to the normal distribution. The tails are most pronounced for the smallest separation distances and become shorter as the integral length scale is approached. Fig. 3 shows that the PDF of the increments follows a normal distribution for all separation distances initially. After 3 s, however, the flow solver had modified the PDF of the increments to a more realistic shape. It exhibits tails which become longer with decreasing separation distance, as predicted by theory and confirmed by many experimental results (Sreenivasan and Antonia, 1997).

In summary, it was shown that the synthetic turbulence worked well within an LES of decaying turbulence. The initial power spectrum was well maintained in terms of its shape. The overall energy dissipation was in the expected range and the numerical dissipation only affected scales smaller than four times the grid spacing. Even though not present in the synthetic turbulence, the velocity developed intermittency during the LES, making the turbulence more realistic. The synthetic turbulence generated by this method was further studied and compared to LES data from the ABL in sec. A.2 in order to evaluate its suitability for the application presented in sec. A.3.

2.2 Comparison of LES data from the atmospheric boundary layer with the synthetic turbulence method

In the paper presented in sec. A.2, results from the synthetic turbulence method presented in sec. A.1 were compared to results from an LES of the whole ABL. The LES of the ABL was performed by the PArallelized LES Model (PALM, Raasch and Schröter, 2001). During the simulation of the ABL, virtual flights were performed in order to record time series of the velocity vector comparable to flight measurements. The statistics of the measured time series were used as input for the synthetic turbulence method which then produced a 3D synthetic turbulent wind field based on the measured statistics. The generated wind field was compared to the original wind field from the PALM simulation. Virtual measurements in the PALM simulations were taken in three different scenarios:

- buoyancy-driven convective boundary layer (CBL) without mean wind,
- CBL with 5 m/s geostrophic wind at the top of the ABL,
- shear-driven stably stratified boundary layer (SBL).

Simulations were performed for a period of 6 h. After 1 h the turbulent flow reached a quasi-steady state and the virtual measurements were started. For the convective boundary layer cases a model domain of 4 x 4 x 1.7 km^3 with a total number of 2049 x 2049 x 450=1.89$\cdot$10^9 grid points and a cell size of 2 m was used. The domain for the SBL scenario had a size of 800 x 800 x 800 m^3. The total number of points was 0.5$\cdot$10^9 and the cell size was 1 m.

The virtual flight measurements for each scenario were taken at 10 different heights simultaneously. The virtual measurement flight was carried out with a ground speed of 62.5 m/s, which corresponds to a distance between the measurement points of 10 and 5 m for the CBL and SBL cases, respectively. The flight path had an angle of 30° with the x-axis. Since periodic boundary conditions were used, this ensured that the virtual flight was not passing the same turbulent structures more than once. At the beginning of the simulation the heights of the flight paths were between 50 m and 500 m (CBL cases) and 50 m and 300 m (SBL case). During the simulation the ratio between boundary layer height and flight height was kept constant. A detailed analysis was carried out to guarantee the statistical significance of the measured statistics.

For the input of the synthetic turbulence method, the energy spectrum, correlation matrix and variances were taken from the the virtual flight measurements. An initial flight height of 400 m was chosen for the CBL cases. This height was at about half of the boundary layer height (z_i) and within the mixing layer. For the SBL case an initial flight height of 125 m was chosen.

The PALM results of the CBL case without wind showed the typical boundary layer structure where small regions of updrafts are surrounded by larger regions of downdrafts, arranged in a hexagonal pattern (Schmidt and Schumann, 1989). The updraft regions have larger absolute values of vertical velocity than the downdraft regions and the vertical velocity shows a non-Gaussian distribution. This typical behaviour can be recognised in the PDF of the vertical velocity in Fig.4. Depicted is the PDF of the vertical velocity calculated from the virtual time series (dotted-dashed), the horizontal plane in which the timeseries was recorded (line) and the synthetic turbulence based on the statistics from the virtual time series (dotted). The PDFs calculated from the PALM data both show a significant skewness. The maximum of the PDF is shifted towards negative values, indicating that areas of downdrafts have a larger extent than regions of updrafts. The tail on the positive end of the distribution is extending to larger values than on the negative end, representing the larger absolute values of vertical velocity of the updrafts. The PDF of the vertical velocity from the synthetic turbulence has a Gaussian shape. The different characteristics of the up- and downdrafts are not reflected in the synthetic turbulence.

Nevertheless, the synthetic turbulence was able to reproduce some of the important statistics of the measured turbulence. In Tab. 1 it can be seen that the input statistics taken from the virtual flight measurements are in very good agreement with the statistics from the synthetic turbulence.

For the case of a CBL with geostrophic wind at the top of the ABL, the results were qualitatively similar to the ones without wind presented above. More details about that case are presented in the paper in Sec. A.2.

In the SBL case the turbulent boundary layer in PALM was characterised by smaller

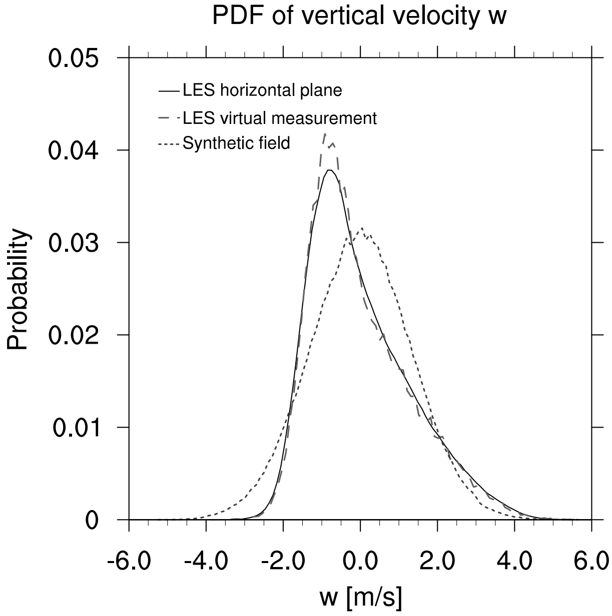

Figure 4: *CBL without mean background wind: probability density function of the vertical velocity w at height 0.46 z_i for the LES field (line), the virtual measurement (dashed) and the synthetic field (dotted).*

	LES horizontal plane	LES virtual measurement	Synthetic field
σ_u^2 (m^2/s^2)	0.72	0.73	0.74
σ_v^2 (m^2/s^2)	0.70	0.73	0.70
σ_w^2 (m^2/s^2)	1.61	1.67	1.68
cor(u,w)	0.01	-0.001	0.01
cor(v,w)	0.01	0.03	0.01
cor(u,v)	-0.01	-0.03	-0.002

Table 1: *CBL without mean background wind: variances and correlation coefficients of the velocity components are given for the LES field (spatial average), the virtual time series (time average) and the synthetic field (spatial average).*

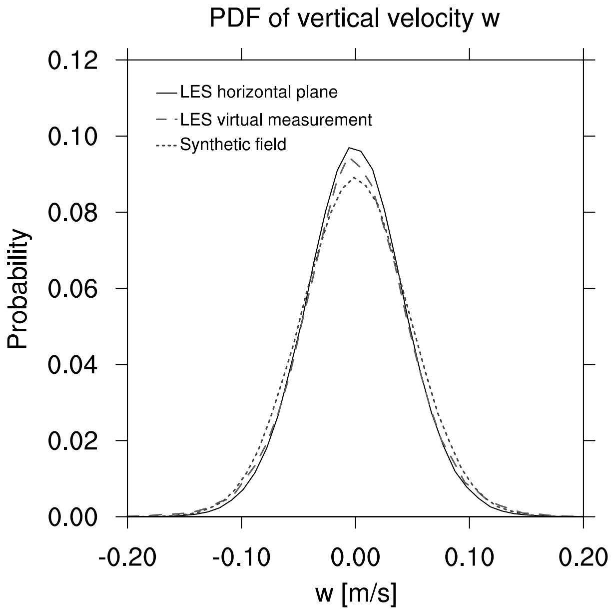

Figure 5: *SBL: probability density function of the vertical velocity w at height 125 m for the LES field (line), the virtual measurement (dashed) and the synthetic field (dotted).*

eddies. Due to the stable stratification, vertical upward displacement of air parcels was suppressed which led to smaller eddies than in the CBL case. The turbulence in this scenario was generated by the shear of the mean wind. The resulting boundary layer has a smaller depth than in the CBL case. In SBLs small scale flow structures are dominating and coherent structures are mostly absent. Therefore, the PDF of the vertical velocity exhibits very different features than in the CBL case (see Fig. 5). Both the PDF from the horizontal plane and from the virtual measurement in PALM show a Gaussian-like distribution and agree well with the PDF from the synthetic turbulence. It can be seen that in all three data sets up- and downdrafts are equally distributed which leads to a better match between the synthetic turbulence and the PALM results compared to the CBL case.

Tab. 2 shows the input statistics of the synthetic turbulence for the SBL case. Like for the CBL it shows very good agreement with the statistics of the generated synthetic turbulence.

Additionally, it should be mentioned that the synthetic turbulence did not contain any vertical change in the turbulence statistics, since the statistics from the measured time series is projected onto the 3D domain to produce homogeneous turbulence. This had

	LES horizontal plane	LES virtual measurement	Synthetic field
σ_u^2 (m^2/s^2)	0.006	0.006	0.006
σ_v^2 (m^2/s^2)	0.01	0.01	0.01
σ_w^2 (m^2/s^2)	0.002	0.002	0.002
cor(u,w)	0.04	0.02	0.04
cor(v,w)	-0.24	-0.24	-0.24
cor(u,v)	-0.14	-0.16	-0.16

Table 2: *SBL: variances and correlation coefficients of the velocity components are given for the LES field (spatial average), the virtual time series (time average) and the synthetic field (spatial average).*

to be done since the input statistics were taken from one flight level and therefore, did not provide any information about the vertical profiles. However, since the flight level was within the mixing layer, the vertical change of the turbulence statistics could be assumed to be very small.

In summary, the generated synthetic turbulence was able to capture many statistical features of ABL turbulence, but was not able to reproduce coherent structures in the CBL. This might be a drawback for the simulation of the flow around the wing since these coherent structures are creating stronger gradients between the areas of up- and downdrafts and therefore, might have a different influence on the wing than the synthetic turbulence field. Due to the limited computational power available it is not practical to run an LES for the whole ABL for each simulation of the turbulent flow around a wing. Therefore, a trade-off had to be made between the availability of computational resources and the quality of the turbulence field. And since the input statistics were captured very well with the synthetic turbulence, a simulation of the turbulent flow around a wing using the synthetic turbulence field is still very insightful.

2.3 Simulating the turbulent flow around a wing

The paper in Sec. A.3 presents the simulation of the turbulent flow around a wing. The simulation was conducted by using the DLR-TAU flow solver and applying a hybrid URANS/LES technique on two grids. The first grid was an unstructured body-

fitted grid around the wing and the second a Cartesian grid in front of the wing which was initialised with the turbulence field. During the simulation the Cartesian grid was moved towards the wing. In a short distance in front of the wing the Cartesian grid was stopped, allowing the turbulence field to leave the grid and flow onto the unstructured grid where it could interact with the wing.
The model domain is depicted in Fig. 6. The wing is located in the center of the figure. It was so small, compared to the model domain that it can only be seen in the zoomed view shown in the top right corner of the figure. The wing had a chord length of $c = 3$ m and a wing span of 15 m. An ONERA-A airfoil was chosen which was stretched in spanwise direction. In order to reduce the disturbance of the flow, round wing tips were added. The distance of the first wall-normal point ranged from $y1^+ = 0.1$ to $y1^+ = 1$. Next to the surface of the wing 74 wall-normal layers of hexahedrical elements were included in the primary grid. In total the wing had about 70000 surface points and 150 cells resolving the spanwise direction.
The primary grid was an unstructured grid body-fitted around the wing with extremely small grid cells close to the wing (about $\Delta x/c = 1.6 \cdot 10^{-6}$) and increasing grid cell size towards the outer boundary of the domain, reaching a maximum of $\Delta x/c = 13.3$. The sector upstream of the wing on the unstructured grid was refined to around $5\Delta x$ of the Cartesian grid. This was necessary to ensure proper interpolation between the two grids further away from the wing. In a radius around the wing of around $4c$ the resolution of the unstructured grid was increased to $\Delta x/c = 0.23$ (the same as in the Cartesian grid). This radius is the distance at which the turbulence field was passed from the Cartesian grid to the unstructured grid during the simulation.
In front of the wing a grey block can be seen which represents the secondary grid. It is a Cartesian grid with a constant cell size of $\Delta x/c = 0.23$ and a normalised cube edge length of $L/c = 66.3$. On the Cartesian grid the turbulent flow was simulated while it approached the wing. The synthetic turbulence from sec. A.1 was used to initialise the turbulence field. During the simulation the Cartesian grid was transported towards the wing until the cell size of both grids was roughly equal. At that point, in short distance to the wing, the Cartesian grid was stopped and the turbulence moved out of the Cartesian grid onto the body-fitted grid where it could interact with the wing. Communication between the two grids was achieved by using the Chimera technique (Schwamborn *et al.*, 2006)

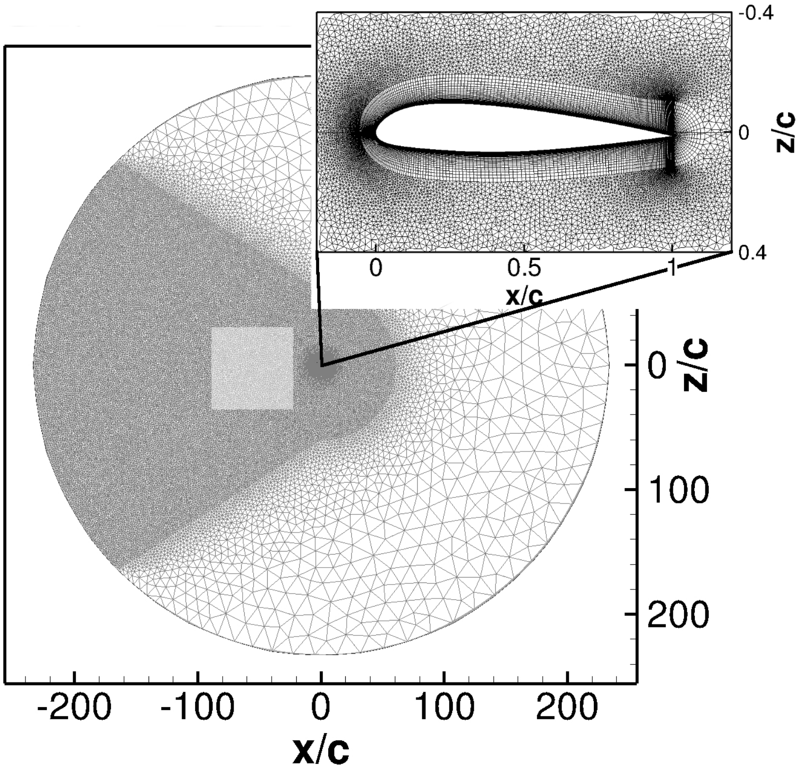

Figure 6: *Model domain for the Chimera simulations with DLR-TAU. The domain consists of two grids. The primary grid was body-fitted around the wing. The secondary Cartesian grid (grey block) was used to simulate the turbulent flow in front of the wing.*

For the turbulence modelling a DES model was used which switches between URANS and LES behaviour depending on the RANS length scale and the grid cell size. If the grid was coarse compared to the turbulent length scale, URANS was used. If the turbulent length scale was large compared to the grid cell size, the model switched into LES mode. In order to guarantee URANS behaviour in the boundary layer of the wing, a volume was defined which enclosed the wing and its boundary layer. Inside this volume the use of the URANS turbulence model was enforced. The grid spacing in the Cartesian grid was fine enough to operate the DES model in LES mode for the simulation of the turbulence field. Once the turbulence field entered the body-fitted grid, the turbulence mode depended on the grid resolution. Close to the center (in terms of y and z), where the wing was located, LES was used while for larger distances from the wing the model was in URANS mode. The timestep size of the simulation was set to $1.25 \cdot 10^{-4}$ s or $t^* = U/c \cdot t = 2.54 \cdot 10^{-3}$ in dimensionless units. The total simulation time was 4 s ($t^* = 81.40$).

The main objective of this study was to investigate the behaviour of the turbulence during the simulation. Therefore a relatively small angle of attack was chosen to avoid complications from instationary effects developing at the wing. While approaching the wing the turbulence field faced many different kinds of numerical conditions. It changed from a Cartesian grid to an unstructured grid and from a full LES to a hybrid URANS/LES. At the same time the grid resolution kept changing while the turbulence was approaching the wing. In the following the main results of that investigation are presented.

In order to study the influence of different turbulence models and grid characteristics, time series from two points on the unstructured grid were analysed and compared to the space series from the turbulence field at 0.89 s ($t^* = 18.1$, when the Cartesian grid was stopped). Fig. 7 shows the location of the two points and the path along which the space series were taken. Point 1 was chosen to be in front of the wing in x-direction but far above it outside the influence of the wing. In that part of the grid the turbulence model operated in URANS mode. Point 2 was in front of the wing and at the same altitude. This location was influenced by the flow field of the wing. Close to the wing (in terms of y and z) the turbulence model was in LES mode while further away from the wing, it was in URANS mode. The lines which represent the space series of the turbulence field on the Cartesian grid are inclined by the angle of attack of the wing. During the simulation the signal on those lines traveled through point 1 and 2, respectively.

Fig. 8 shows the normalised 1D power spectra of the time series in point 1 and 2 compared to the 1D power spectra from the space series along the lines depicted in Fig. 7. In order to get significant statistics the power spectra were averaged in y-direction over all points within the extent of the Cartesian grid. For a better comparison the wavenumber spectra from the space series were converted into frequency spectra by using the velocity of the mean flight speed. As mentioned above, the power spectrum at position 1 is representing the resolved turbulence in the URANS domain. At position 2 the turbulence model was either in LES mode (closer to the wing in y-direction) or URANS mode (further away from the wing in y-direction). Therefore, for each turbulence model mode, one power spectrum was calculated to study the difference between URANS and LES modelling. The spectra from both space series are almost identical. This is a result of the initialisation with the synthetic turbulence which is homogeneous by

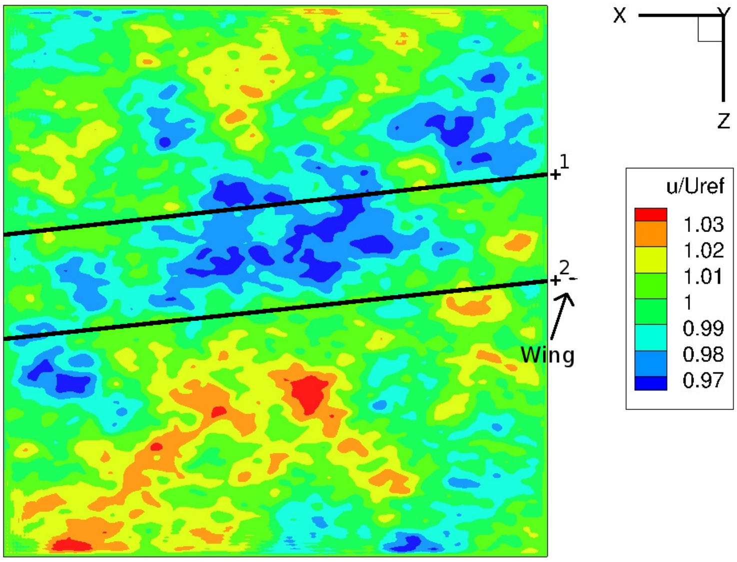

Figure 7: *Paths through the Cartesian grid from which the space series were extracted (black lines). The crosses mark the position on the unstructured grid from which the time series were taken. In front of the turbulence field the wing can be seen as a black dot near position 2. The colors in the turbulence field are representing the normalised velocity in* x*-direction.*

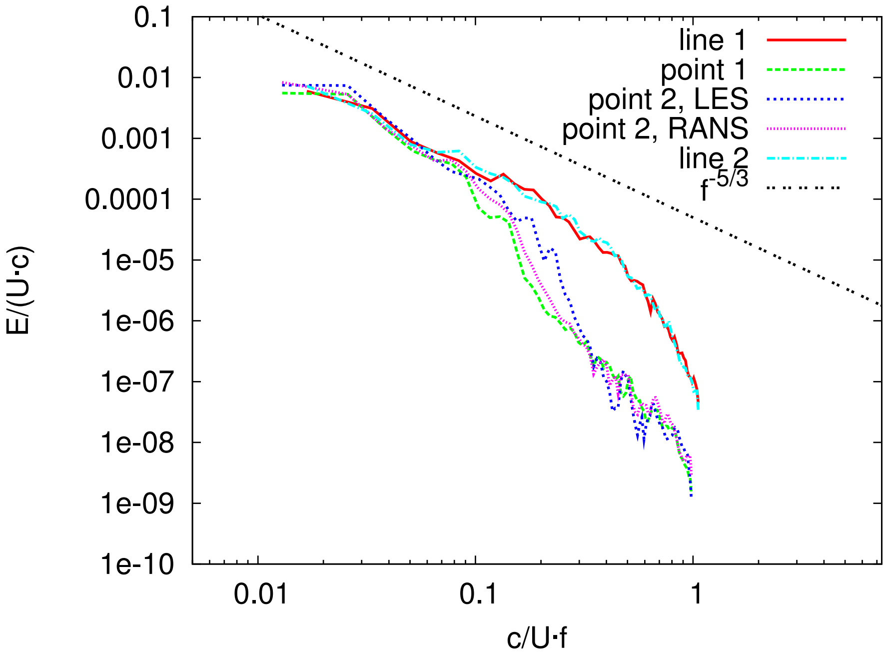

Figure 8: *Normalised 1D energy spectra (summation of the spectra for u, v and w) in x-direction for the space series for position 1 (red, solid line), the time series for position 1 (green, long dashed), the time series for position 2 in the LES part (blue, short dashed), the time series in the URANS part (pink, dotted) and the space series for position 2 (light blue, dash-dotted). For comparison the $f^{-5/3}$-slope of the inertial subrange is plotted in black (double dotted).*

design. In the large scales the spectra from the time series and space series are almost the same. At those frequencies almost no dissipation effects are visible when comparing the space and time series. However, in the smaller scales a significant drop in the power spectra derived from the time series is visible. Apparently, there was a much stronger dissipation on the unstructured grid compared to the Cartesian grid. When comparing the spectra in the LES and URANS domain on the unstructured grid, almost no difference can be seen. It seems that in that short time, the larger grid cells and the turbulence model in the URANS part of the domain were not affecting the flow in a negative way compared to LES.

Table 3 shows the normalised turbulence kinetic energy (TKE) for the URANS and LES parts of the domain at position 1 and 2 for the time and space series, respectively. It shows that in general the variances in the time series of point 1 and 2 are smaller than

	position 1	position 2
point URANS	$0.35 \cdot 10^{-3}$	$0.48 \cdot 10^{-3}$
point LES	-	$0.46 \cdot 10^{-3}$
line	$0.56 \cdot 10^{-3}$	$0.68 \cdot 10^{-3}$

Table 3: *Normalised TKE K/U^2 for the time and space series in position 1 and 2.*

in the space series from the Cartesian grid. The values for the URANS and LES part in position 2 show no significant difference in resolved TKE.

It was shown that the complex numerical setup of this simulation was affecting the turbulent flow. The change from the Cartesian grid to the unstructured grid caused a significant drop in energy in the small scales. Therefore, it would be advisable to keep the turbulent flow on the Cartesian grid for as long as possible and stop the Cartesian grid only in a very short distance in front of the wing. The change between turbulence modes, however, had almost no effect on the turbulence. In the short time simulated in this case, adaption of the flow to the URANS mode was too slow to dissipate the resolved turbulence in a significant way.

2.4 An anisotropic synthetic turbulence method for Large-Eddy Simulation

While in Sec. A.1 to A.3 a synthetic turbulence method for initialising a 3D turbulent flow was developed and applied, in Sec. A.4 synthetic turbulence for the inflow boundary condition of an LES domain was developed and tested. The generated turbulence did not serve as a 3D initial field, but as a time series of 2D turbulence fields which were fed into the LES domain through the inflow boundary. This technique can be very useful, for example, for hybrid URANS/LES where the flow coming from the URANS domain into the LES domain lacks resolved turbulence. In that case synthetic turbulence can be injected into the interface between the URANS and LES domain to trigger realistic resolved turbulence in the LES domain. The statistical properties of the generated turbulence were based on the statistics given by a Reynolds stress model (RSM). It uses the Reynolds stresses and the dissipation rate to parameterise the turbulence for URANS.

The test case chosen for generating and testing the synthetic turbulence was a turbulent channel flow at a turbulent Reynolds number of $\mathrm{Re}_{\mathrm{turb}} = 395$. The channel had an inflow and outflow boundary in x-direction. The upper and lower boundary condition was a viscous wall and in z-direction periodic boundary conditions were applied. The case was simulated using the DNS data by Moser *et al.* (1999). Therefore, the Reynolds stresses and dissipation rate, which in a hybrid URANS/LES would be provided by the RSM, could be taken from the DNS results and used as input for the synthetic turbulence method.

Like the approach in Sec. A.1 this synthetic turbulence method was also based on Fourier modes. But unlike in the method described before a 1D power spectrum was used. Taking the Reynolds stresses and dissipation rate as input, a 1D model spectrum $S_i(k_x, y, z)$ was calculated for each point y and z following Kamruzzaman *et al.* (2012). By applying the following equation, spectral velocities could be calculated from the model spectrum:

$$\tilde{u_i}(k_x, y, z) = a_i(k_x, y, z) \cdot \frac{1}{2}\sqrt{(S_i(k_x, y, z)) \cdot \Delta k_x}, \tag{6}$$

where Δk_x is the wave number interval in x-direction and $a_i(k_x, y, z)$ are the signs of the spectral velocities for each wave number k_x and position y and z. They can take the values -1 or 1. By performing an inverse 1D Fourier transform on the spectral velocities for each y and z, a 3D velocity field was generated in which the x-dimension can be interpreted as the time dimension. The resulting turbulence followed the given model spectrum. As a consequence, it showed the correct normal stresses which resulted from the integral over the model spectrum. Furthermore, the integral length scales in x-direction, adjusted by the correct position of the transition between energy producing range and inertial subrange in the model spectrum, were realistic as well.

To also gain control over the shear stresses, usually the Cholesky decomposition is applied. One disadvantage of this approach is however, that this method applies a transformation matrix to the velocity field in order to produce the correct shear stresses. This procedure leads to significant changes in the 1D statistics. Since the synthetic turbulence method presented here was based on prescribing 1D statistics, a new procedure to produce correct shear stresses, independently from the other statistical parameters, was proposed. It could be shown that by proper choice of the signs of the spectral velocities a_i, the given shear stresses can be reproduced. Since only the signs of the spectral velocities were changed, other statistical parameters remained mainly unchanged.

Synthetic turbulence generated through this method would reproduce correct Reynolds stresses, integral length scales in x-direction and power spectra. However, if the inverse 1D Fourier transform was performed at each point y and z the 1D turbulence signals would not be correlated in y and z direction. Such a turbulence field would quickly dissipate in an LES, since the turbulent scales in y and z direction would be of the size of the grid cells and therefore, much too small.

To find a remedy for this problem, the 1D turbulence signals in x-direction were not calculated for each point in the y-z-plane. Instead a certain number of grid cells in y- and z-direction were skipped and the values in between these points were interpolated. That way a correlation between the points was enforced and, by properly choosing the number of grid cells to be skipped, the integral length scale in y- and z-direction could be set to more realistic values. The method of interpolation was affecting the accuracy of the results significantly. While the original turbulence without interpolation reproduced the input statistics almost without any deviations, the interpolated turbulence showed deviations to varying degrees, depending on how the velocities were interpolated. Three different methods were investigated.

The first and simplest method was a linear interpolation of the velocities. Since the deviations from the given Reynolds stresses were in the order of 50%, another interpolation was applied which guaranteed the linear interpolation of the normal stresses. This could be achieved by linear interpolation of the squares of the velocities and subsequent root taking (called square interpolation in the following). The resulting positive velocity value was given the sign of the velocity value of the point closest to the interpolated point. This method reduced the deviations in the normal stresses to about 3% to 6% and for the shear stress to 24%. Since the sign of the interpolated velocity was assigned after the linear interpolation of the squares of the velocities, jumps occurred in the velocity field which led to strong gradients whenever the velocity changed signs. Therefore, a third method was developed, where the signs of the velocities were already assigned to the squares of the velocities inside the interpolation equation (called smooth square interpolation in the following). This approach led to smooth velocity fields. However, whenever the velocity changed sign, larger deviations from the normal stresses were introduced, leading to values of around 22%. For the shear stress 35%

	Δ_{uu}	Δ_{vv}	Δ_{ww}	Δ_{uv}
linear	51.0 %	51.9 %	51.3 %	55.7 %
square	5.9 %	3.5 %	3.9 %	24.3 %
square smooth	21.4 %	22.7 %	21.8 %	34.9 %

Table 4: *Mean deviation of the absolute values of the covariances from the synthetic turbulence from the DNS data in percent.*

was reached. A summary of the deviations is given in Tab. 4.

In Fig. 9 vertical profiles of the integral length scales in x-direction for the three velocity components are shown for all three interpolation methods and the DNS data (the channel height is given in terms of the dimensionless length y/δ, where δ is the channel half-height). The length scales for all three interpolation methods are very similar. They are also in good agreement with the DNS data with only the integral length scale from the square interpolation being a bit smaller than the integral length scales from the other interpolation methods.

The big advantage of the synthetic turbulence method with interpolation over the method without interpolation can be seen in Fig. 10 where the integral length scales in z-direction are shown for the three velocity components for all three interpolation methods and the data from the DNS. In the synthetic turbulence without interpolation these integral length scales were all equal to the grid cell size. Due to the interpolation applied, an autocorrelation of the velocity components was introduced and therefore, larger integral length scales could be achieved. By choosing the number of cells to skip and interpolating in accordance with the given integral length scale in x-direction from the DNS, profiles of the length scales could be achieved which are roughly reproducing the DNS length scale in x-direction with small values towards the walls and increasing values towards the middle of the channel. For simplicity the same length scale was set in all three directions and therefore, the profiles in y- and z-direction were overestimating the length scales in these directions. For the linear and smooth square interpolation the length scales were similar while for the square interpolation the length scales were significantly smaller.

All three interpolation methods were tested in an LES of a channel flow at $\mathrm{Re}_{\mathrm{turb}} = 395$ using the flow solver DLR-TAU. Several convective time units (the average time it takes

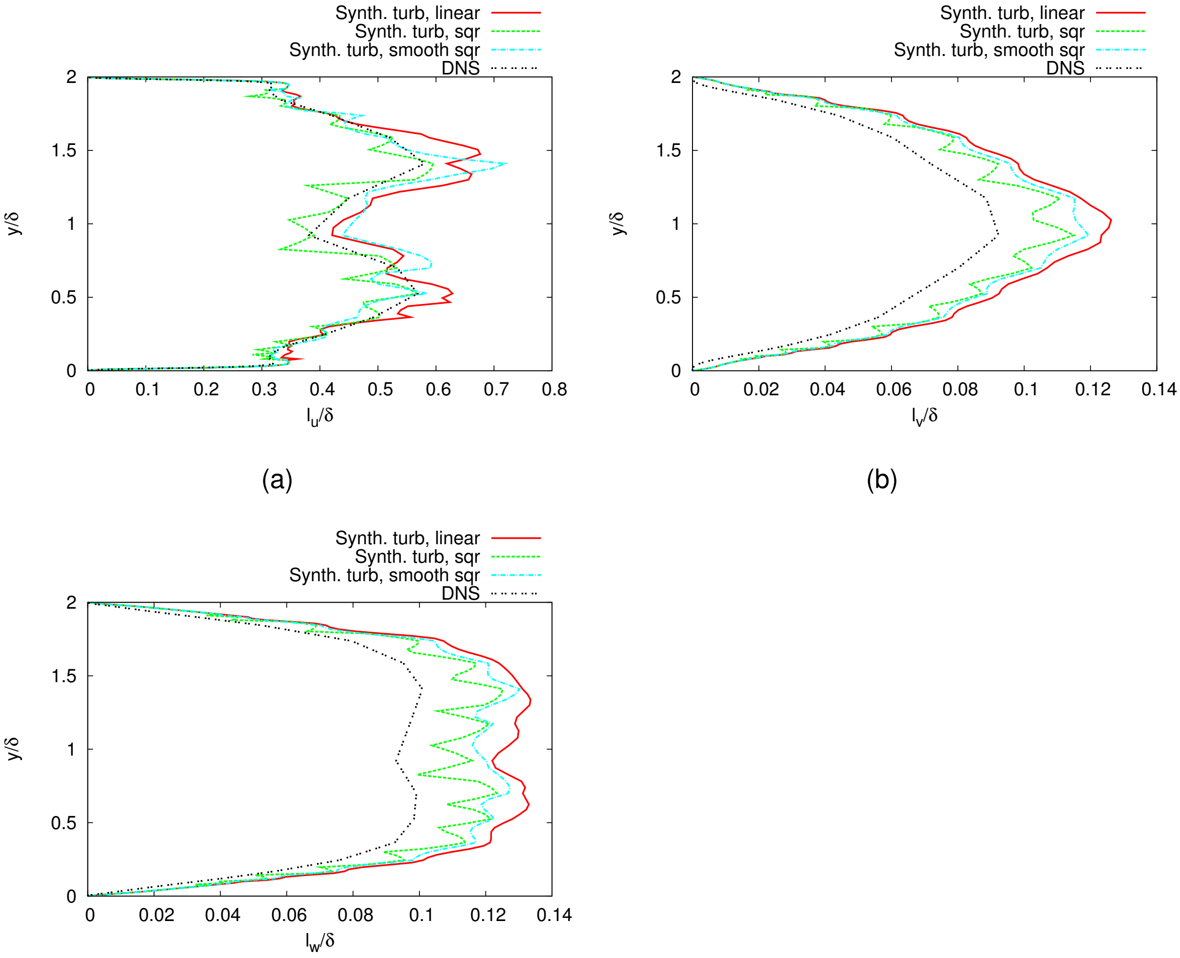

(a)

(b)

(c)

Figure 9: *Vertical profiles of the normalised integral length scales of (a) u, (b) v and (c) w in x-direction estimated from the DNS data (black, double dotted) and calculated from the synthetic turbulence with linear interpolation (red, line), square (green, dashed) and smooth square (blue, dot-dashed).*

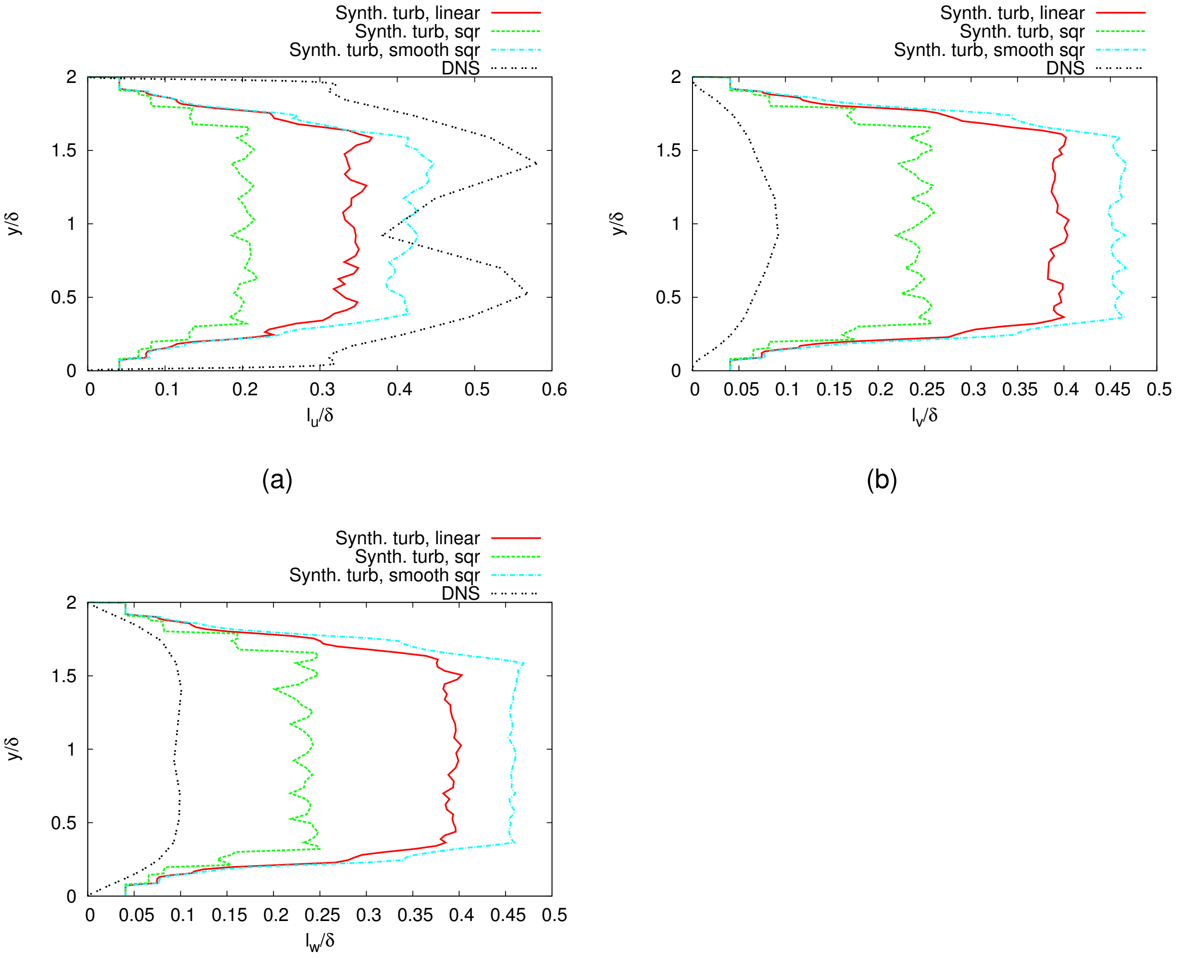

(a)

(b)

(c)

Figure 10: *Vertical profiles of the normalised integral length scales of (a)* u*, (b)* v *and (c)* w *in* z*-direction estimated from the DNS data (black, double dotted) and calculated from the synthetic turbulence with linear interpolation (red, line), square (green, dashed) and smooth square (blue, dot-dashed).*

the flow to travel through the channel) were simulated in order to calculate significant statistics. The skin-friction coefficient at the channel wall c_f can be used as an indicator for the quality of the synthetic turbulence. It depends on the Reynolds stress profiles and therefore, indicates how realistic the development of the turbulence in the channel is. It also provides the adjustment length, which is the distance it takes for the turbulence in the channel to recover to the original value of c_f from the DNS. The values of c_f along the channel for the three interpolation methods can be seen in Fig. 11. For all interpolation methods c_f drops immediately after the inlet. In case of the linear interpolation the drop is strongest. It takes around 18 channel half heights (δ) to recover to a constant value of about $c_f = 5.9 \cdot 10^{-3}$, which is significantly lower than the reference value of $c_f = 6.27 \cdot 10^{-3}$ from the DNS. An improvement in performance can be seen with the square interpolation. Even though it introduced unnatural jumps in the velocity field, the drop in c_f after the inlet is smaller and the adjustment length is shorter (around 17 δ). The value to which it recovers is also larger, reaching $c_f = 6.1 \cdot 10^{-3}$, but still smaller than the reference value. Another improvement can be seen when applying the smooth square interpolation. The drop after the inlet is reduced compared to the square interpolation and the adjustment length is shorter (about 16 δ). The constant level reached towards the end of the channel is slightly larger than in the square interpolation.

Since the model spectrum used for generating the synthetic turbulence was designed for large Reynolds numbers, it looks quite different from the original spectrum in the DNS, which had a rather low Reynolds number. Therefore, a fourth simulation was performed using the smooth square interpolation. To account for the low Reynolds number, the synthetic turbulence was generated using the DNS spectrum as input (since there are no model spectra for low Reynolds numbers available in the literature). In Fig. 11 it can be seen that this change adds a further improvement to the simulation. The value for c_f drops much less than in the previous simulations and also recovers already after 15 δ. The value to which it recovers is almost identical to the reference value from the DNS. The shape of the power spectrum apparently had a strong influence on the performance of the synthetic turbulence in the LES of the channel flow.

The synthetic turbulence method presented in Sec. A.4 showed good results when used as inflow boundary condition in an LES of a channel flow. Especially, when using an energy spectrum fitting the Reynolds number of the simulated case, the adjustment

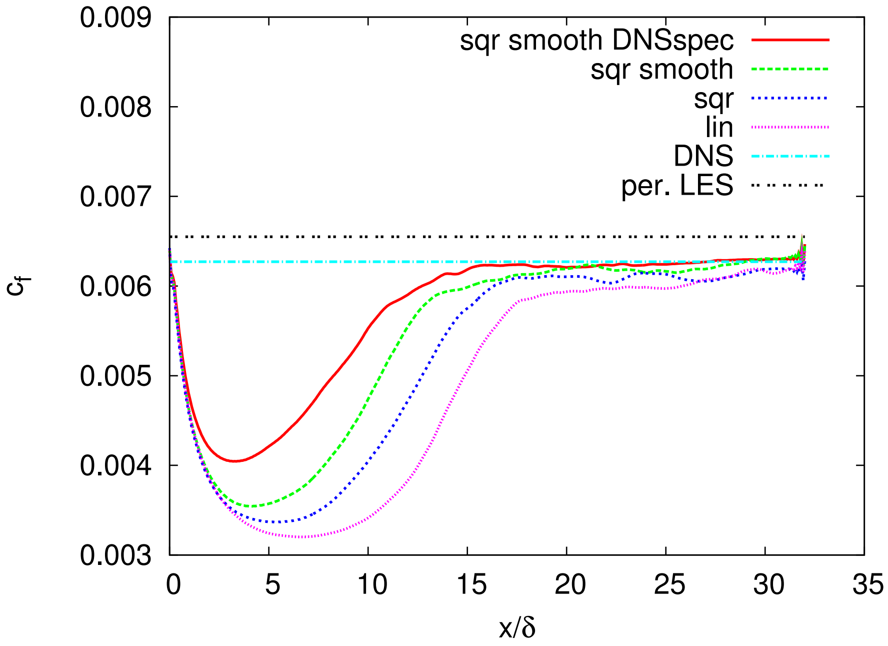

Figure 11: *Time and span-averaged skin-friction coefficient along the channel from LES with synthetic turbulence using linear (pink, dotted), square (blue, short dashed) and smooth square (green, dashed) interpolation. Additionally, the result for the run with smooth square interpolation and DNS-spectra is depicted in red (solid line). For comparison the* c_f *value from the DNS and periodic LES is shown in light blue (dash-dotted) and black (double dotted), respectively.*

length was reasonably short and the skin-friction coefficient recovered to the reference value from the DNS. With this method it is possible to set a variety of statistical parameters of the generated turbulence independently. Therefore, this new synthetic turbulence method is not only suitable as an inflow boundary condition for LES but also provides a tool to study the influence of different statistical parameters of the synthetic turbulence on the turbulent flow in an LES.

3 Discussion and outlook

Turbulence is a phenomenon that is fundamental to most cases of fluid flows and crucial for a large variety of research fields in engineering and natural science. With the strong increase in available computational power since the first supercomputers, solving those flow problems by CFD has become the natural choice and a vast number of studies are available tackling all kinds of turbulent flows with flow solvers using different degrees of parameterisations. In this spectrum of available CFD techniques, synthetic turbulence has its place as a possibility to speed up simulations and reduce numerical costs.

The current trend towards turbulence-resolving techniques like hybrid RANS/LES will continue and, despite the limited computational power available, allow to simulate complex flows more accurately in the future. For many scenarios the quality of the simulation will be crucially affected by the quality of the synthetic turbulence introduced in the transition region between the RANS and LES domain. Therefore, further improvement of synthetic turbulence generation is the subject of ongoing research. For example, Yin *et al.* (2016) have recently proposed a wavelet-based synthetic turbulence method which is able to introduce intermittency to the turbulence signal. This development is of great importance for future applications, e.g. the interaction of turbulent flow with solid structures, since intermittent velocity bursts can be stronger than expected from a non-intermittent signal and thereby, cause increased loads on structures. Achievements like these will make it more feasible in the future to carry out hybrid RANS/LES studies of large and complex configurations of e.g. aircrafts operating at high angles of attack (Luckring *et al.*, 2015) or dispersion of pollutants in urban environments (Jadidi *et al.*, 2016), allowing to increase our knowledge in a large variety of fields.

This thesis contributes to the progress in the field of synthetic turbulence by focusing on the development of efficient and flexible methods and their application. Two scenarios for the application of synthetic turbulence were presented. The performance of the presented synthetic turbulence methods and their potential for future work will be discussed in the following sections.

Scenario 1: Simulation of the turbulent ABL flow around a wing

The first method was developed based on the well-known Fourier approach in order to generate a 3D initial turbulent wind field for the simulation of a turbulent flow around a wing (Sec. A.1). For this simulation (presented in Sec. A.3) it was crucial that the statistical properties of the turbulent wind field would be maintained well during the simulation until the turbulence interacts with the wing inside the model domain. This was achieved by initialising the model with synthetic turbulence that possessed realistic statistics derived from measurement data. The turbulence generator was first tested in an LES of decaying turbulence, where it was found that the input statistics could be maintained well. However, the generation of a matching density and pressure field was challenging. The simple approach used in this thesis triggered sound waves during the simulation of the turbulent flow around the wing (see Fig. 5 in Sec. A.3) and changed the turbulence field in the early phase of that simulation. This could mostly be seen in the cross-correlations of the velocity components (Tab. 1 in Sec. A.3). Therefore, developing a more sophisticated approach to generate matching pressure and density fields with the synthetic turbulence would be desirable.

In a comparison of the synthetic turbulence field with LES data from the ABL (see Sec. A.2), it was shown that the synthetic turbulence represents the input statistics very well. However, the approach is unable to represent coherent structures present in a CBL. For a more realistic simulation of the turbulent ABL flow around a wing, an addition to the turbulence generator, which produces coherent structures based on measurements, would be a desirable improvement. A possible approach would be to take measurements from several simultaneous flights (e.g. from a swarm of unmanned aerial vehicles) and use a method like Druault *et al.* (2004) to estimate the points in between the flight paths. The estimated coherent structures could then be added to the generated synthetic turbulence field creating a turbulence field containing coherent structures and statistics from flight measurements.

Apart from the initialisation problem, the modelling strategy for the turbulent flow around the wing created challenges as well (Sec. A.3). The turbulent flow in the ABL covers a large range of scales and therefore, the computational demands for the simulation of the interaction of the ABL flow with a wing were very high. To be able to simulate such a case on today's computers, a mix of RANS and LES turbulence models had to be used in order to save computational time in the URANS domain but still be able to resolve turbulence by applying an LES turbulence model where necessary. Changing grid resolutions and grid types as well as changing turbulence model types during the simulation were expected to have an influence on the turbulent flow. In this thesis it was found that the main properties of the turbulent flow could be maintained during the simulation. However, the change in grid resolution and the change from a Cartesian to an unstructured grid caused stronger dissipation of the small scales of the turbulence field. The change from LES to URANS did not affect the turbulent flow significantly, due to the short simulated time the turbulence was exposed to the different turbulence models. Therefore, the present method to simulate a turbulent flow around a wing was found to work well for studying the interaction between turbulence and a wing. In the future and with an improved turbulence generator, this method could be used to study the turbulent flow around a wing at high angles of attack. This would allow to study the influence of turbulence on the aerodynamics, and specifically on the separation of the flow. The influence of different weather scenarios could be studied, for example, by generating turbulence for stable and convective cases.

Scenario 2: An anisotropic synthetic turbulence method for LES

The second application presented in this work, used a modification of the Fourier approach in order to generate a time series of inflow planes for a simulation of a turbulent channel flow (Sec. A.4). This method used 1D model spectra and a new method to generate the correct shear stress profiles independently from the other turbulence statistics. The new turbulence generator was able to reproduce well matching normal and shear stress profiles while at the same time giving realistic turbulent length scales in all three directions and 1D spectra. The ability to set so many different statistical parameters independently, is a clear advantage of the presented method.

In comparison to the established SEM and DF-SEM a good performance of the new method was found while requiring less computation time. Nevertheless, there is still potential for improvement. For a more realistic behaviour, the length scales for the different velocity components could be set independently. This could be achieved by a simple change to the interpolation method. Also, a more realistic model spectrum for low Reynolds numbers would improve the results significantly. Additionally, the method should also be applied to high Reynolds number cases, where a better performance is expected, since the model spectrum in use was designed for high Reynolds number flows. For future studies this method could be used to systematically investigate the influence of statistical parameters of the synthetic turbulence on the developing turbulent flow in the simulation. This method is especially useful for this purpose, since it is able to control many statistical properties independently. A test matrix could be run where only one statistical property at a time is changed and the effect of this change on the developing flow in the simulation is studied. This could help to improve existing synthetic turbulence methods or design better methods in the future.

References

Adamian, D. and **Travin, A.**, **2011**: An Efficient Generator of Synthetic Turbulence at RANS–LES Interface in Embedded LES of Wall-Bounded and Free Shear Flows. In: A. Kuzmin (editor), *Computational Fluid Dynamics 2010*, Springer Berlin Heidelberg, pp. 739–744.

Ahmadi, G. and **Smith, D. H.**, **1998**: Particle transport and deposition in a hot-gas cleanup pilot plant. *Aerosol science and technology*, **29**(3), 183–205.

Bange, J., **Spieß, T.** and **van den Kroonenberg, A.**, **2007**: Characteristics of the Early-Morning Shallow Convective Boundary Layer from Helipod Flights during STINHO-2. *Theor. Appl. Climatol.*, **90**, 113–126.

Batten, P., **Goldberg, U.** and **Chakravarthy, S.**, **2004**: Interfacing statistical turbulence closures with large-eddy simulation. *AIAA journal*, **42**(3), 485–492.

Batten, P., **Goldberg, U.**, **Chakravarthy, S.** and **Batista de Jesus, A.**, **2012**: Large eddy stimulation using simple eddy-viscosity RANS data. In: *Eberhardsteiner, J., Böhm, H.J., Rammerstorfer, F.G (eds.) CD-ROM Proceedings of the 6th European Congress on Computational Methods in Applied Sciences and Engineering (ECCO-MAS 2012), September 10-14, 2012, Vienna, Austria*.

Bouali, Z., **Duret, B.**, **Demoulin, F.-X.** and **Mura, A.**, **2016**: DNS analysis of small-scale turbulence-scalar interactions in evaporating two-phase flows. *International Journal of Multiphase Flow*, **85**, 326–335.

Chung, T. N. and **Liu, C.-H.**, **2013**: On the mechanism of air pollutant removal in two-dimensional idealized street canyons: a large-eddy simulation approach. *Boundary-layer meteorology*, **148**(1), 241–253.

Coceal, O., **Goulart, E. V.**, **Branford, S.**, **Thomas, T. G.** and **Belcher, S. E.**, **2014**: Flow structure and near-field dispersion in arrays of building-like obstacles. *Journal of Wind Engineering and Industrial Aerodynamics*, **125**, 52–68.

Crowder, T. M., **Rosati, J. A.**, **Schroeter, J. D.**, **Hickey, A. J.** and **Martonen, T. B.**, **2002**: Fundamental effects of particle morphology on lung delivery: predictions of

Stokes' law and the particular relevance to dry powder inhaler formulation and development. *Pharmaceutical research*, **19**(3), 239–245.

Davidson, P. A., **2015**: *Turbulence: an introduction for scientists and engineers*. Oxford University Press.

Deardorff, J. W., **1970**: A Numerical Study of Three-Dimensional Turbulent Channel Flow at Large Reynolds Numbers. *J. Fluid Mech.*, **41**, 453–480.

Deck, S., **Gand, F.**, **Brunet, V.** and **Khelil, S. B.**, **2014**: High-fidelity simulations of unsteady civil aircraft aerodynamics: stakes and perspectives. Application of zonal detached eddy simulation. *Philosophical Transactions of the Royal Society of London A: Mathematical, Physical and Engineering Sciences*, **372**(2022), 20130,325.

Druault, P., **Lardeau, S.**, **Bonnet, J.-P.**, **Coiffet, F.**, **Delville, J.**, **Lamballais, E.**, **Largeau, J. F.** and **Perret, L.**, **2004**: Generation of three-dimensional turbulent inlet conditions for large-eddy simulation. *AIAA Journal*, **42**, 447–456.

Druzhinin, O. and **Ostrovsky, L.**, **2015**: Dynamics of turbulence under the effect of stratification and internal waves. *Nonlinear Processes in Geophysics*, **22**(3), 337–348.

Froehlich, J., **2006**: *Large Eddy Simulation turbulenter Strömungen*. Teubner, 1 edn.

Heinrich, R., **2014**: Simulation of Interaction of Aircraft and Gust Using the TAU-Code. *New Results in Numerical and Experimental Fluid Mechanics IX, Notes on Numerical Fluid Mechanics and Multidisciplinary Design.*, **124**, 503–511.

Jadidi, M., **Bazdidi-Tehrani, F.** and **Kiamansouri, M.**, **2016**: Embedded large eddy simulation approach for pollutant dispersion around a model building in atmospheric boundary layer. *Environmental Fluid Mechanics*, **16**(3), 575–601.

Jarrin, N., **Benhamadouche, S.**, **Laurence, D.** and **Prosser, R.**, **2006**: A synthetic-eddy-method for generating inflow conditions for large-eddy simulations. *International Journal of Heat and Fluid Flow*, **27**(4), 585 – 593, special Issue of The Fourth International Symposium on Turbulence and Shear Flow Phenomena - 2005 Special Issue of The Fourth International Symposium on Turbulence and Shear Flow Phenomena - 2005.

Kamruzzaman, M., **Lutz, T.**, **Herrig, A.** and **Krämer, E.**, **2012**: Semi-Empirical Modeling of Turbulent Anisotropy for Airfoil Self-Noise Predictions. *AIAA journal*, **50**(1), 46–60.

Keating, A., **Piomelli, U.**, **Balaras, E.** and **Kaltenbach, H.-J.**, **2004**: A priori and a posteriori tests of inflow conditions for large-eddy simulation. *Physics of Fluids (1994-present)*, **16**(12), 4696–4712.

Kelleners, P. and **Heinrich, R.**, **2015**: Simulation of Interaction of Aircraft with Gust and Resolved LES-Simulated Atmospheric Turbulence. In: R. Radespiel, R. Niehuis, N. Kroll and K. Behrends (editors), *Advances in Simulation of Wing and Nacelle Stall*, Springer, vol. 131.

Kempf, A., **Klein, L.** and **Janicka, J.**, **2005**: Efficient generation of initial- and inflow-conditions for transient turbulent flows in arbitrary geometries. *Flow, Turbulence and Combustion*, **74**, 67–84.

Khan, M., **Pumir, A.** and **Vassilicos, J.**, **2003**: Kinematic simulation of turbulent dispersion of triangles. *Physical Review E*, **68**(2), 026,313.

Klein, M., **Sadiki, A.** and **Janicka, J.**, **2003**: A digital filter based generation of inflow data for spatially developing direct numerical or large eddy simulations. *J. Comp. Phys.*, **186**, 652–665.

Kraichnan, R. H., **1970**: Diffusion by a Random Velocity Field. *The Physics of Fluids*, **13**, 22–31.

Lehmkuhl, O., **Rodríguez, I.**, **Baez, A.**, **Oliva, A.** and **Pérez-Segarra, C.**, **2013**: On the large-eddy simulations for the flow around aerodynamic profiles using unstructured grids. *Computers & Fluids*, **84**, 176–189.

Letzel, M. O., **Helmke, C.**, **Ng, E.**, **An, X.**, **Lai, A.** and **Raasch, S.**, **2012**: LES case study on pedestrian level ventilation in two neighbourhoods in Hong Kong. *Meteorologische Zeitschrift*, **21**(6), 575–589.

Li, A. and **Ahmadi, G.**, **1995**: Computer Simulation of Particle Deposition in the Upper Tracheobronchial Tree. *Aerosol Science and Technology*, **23**(2), 201–223.

Luckring, J. M., **Park, M. A.**, **Hitzel, S. M.**, **Jirasek, A.**, **Lofthouse, A. J.**, **Morton, S. A.**, **McDaniel, D. R.** and **Rizzi, A. M.**, **2015**: A synthesis of hybrid RANS/LES CFD results for F-16XL aircraft aerodynamics.

Lund, T. S., **Wu, X.** and **Squires, K. D.**, **1998**: Generation of Turbulent Inflow Data for Spatially-Developing Boundary Layer Simulations. *J. Comput. Phys.*, **140**, 233–258.

Lyu, Z. and **Martins, J.**, **2013**: RANS-based aerodynamic shape optimization of a blended-wing-body aircraft. In: *43rd AIAA Fluid Dynamics Conference and Exhibit*.

Mannini, C., **Šoda, A.** and **Schewe, G.**, **2010**: Unsteady RANS modelling of flow past a rectangular cylinder: Investigation of Reynolds number effects. *Computers & fluids*, **39**(9), 1609–1624.

Moser, R. D., **Kim, J.** and **Mansour, N. N.**, **1999**: Direct numerical simulation of turbulent channel flow up to Re_τ=590. *Physics of Fluids*, **11**, 943–945.

Orszag, G. A. P., S. A., **1972**: Numerical simulation of three-dimensional homogeneous isotropic turbulence. *Phys. Rev. Letter*, **28**, 76–79.

Petronio, A., **Roman, F.**, **Nasello, C.** and **Armenio, V.**, **2013**: Large eddy simulation model for wind-driven sea circulation in coastal areas. *Nonlinear Processes in Geophysics*, **20**(6), 1095–1112.

Piomelli, U., **Balaras, E.** and **Pascarelli, A.**, **2000**: Turbulent structures in accelerating boundary layers. *Journal of Turbulence*, **1**(1), 001–001.

Polacsek, C., **Reboul, G.**, **Clair, V.**, **Le Garrec, T.** and **Deniau, H.**, **2011**: Turbulence-airfoil interaction noise reduction using wavy leading edge: An experimental and numerical study. In: *Proc. of Inter-Noise*.

Poletto, R., **Revell, A.**, **Craft, T. J.** and **Jarrin, N.**, **2011**: Divergence free synthetic eddy method for embedded LES inflow boundary conditions. In: *Seventh International Symposium On Turbulence and Shear Flow Phenomena (TSFP-7)*, Begell House Inc.

Poroseva, S., **Kaiser, B.**, **Sillero, J.** and **Murman, S.**, **2015**: Validation of a closing procedure for fourth-order RANS turbulence models with DNS data in an incompressible zero-pressure-gradient turbulent boundary layer. *International Journal of Heat and Fluid Flow*, **56**, 71–79.

Raasch, S. and **Schröter, M.**, **2001**: PALM – A large-eddy simulation model performing on massively parallel computers. *Met. Zeitschrift*, **10**, 363–372.

Reynolds, O., **1895**: On the dynamical theory of incompressible viscous fluids and the determination of the criterion. *Philosophical Transactions of the Royal Society of London. A*, 123–164.

Richardson, L., **1922**: Weather prediction by numerical process.

Schmidt, H. and **Schumann, U.**, **1989**: Coherent structure of the convective boundary layer derived from large-eddy simulations. *Journal of Fluid Mechanics*, **200**, 511–562.

Schwamborn, D., **Gerhold, T.** and **Heinrich, R.**, **2006**: The DLR TAU-Code: Recent Applications in Research and Industry. In: *ECCOMAS CFD, P. Wesseling, E. Oñate, J. Périaux (Eds), TU Delft, The Netherlands*.

Smagorinsky, J., **1963**: General circulation experiments with the primitive equations: I. the basic experiment*. *Monthly weather review*, **91**(3), 99–164.

Smirnov, A., **Shi, S.** and **Celik, I.**, **2001**: Random Flow Generation Technique for Large Eddy Simulations and Particle-Dynamics Modeling. *Journal of Fluids Engineering*, **123**, 359–371.

Spalart, P. R., **2009**: Detached-eddy simulation. *Annual review of fluid mechanics*, **41**, 181–202.

Spalart, P. R. and **Allmaras, S. R.**, **1992**: A one-equation turbulence model for aerodynamic flows. *AIAA, Aerospace Sciences Meeting and Exhibit, 30th*.

Spalart, P. R. and **Watmuff, J. H.**, **1993**: Experimental and numerical study of a turbulent boundary layer with pressure gradients. *Journal of Fluid Mechanics*, **249**, 337–371.

Spalart, P. R., **Jou, W.-H.**, **Strelets, M.** and **Allmaras, S. R.**, **1997**: Comments on the feas1ibility of LES for wings, and on a hybrid RANS/LES approach. *Proceedings of first AFOSR international conference on DNS/LES*.

Sreenivasan, K. R., **1999**: Fluid turbulence. *Rev. Modern Phys.*, **71**, 383–395.

Sreenivasan, K. R. and **Antonia, R. A.**, **1997**: The phenomenology of small-scale turbulence. *Annu. Rev. Fluid Mech.*, **29**, 435–472.

Troldborg, N., **Sørensen, J. N.** and **Mikkelsen, R.**, **2007**: Actuator line simulation of wake of wind turbine operating in turbulent inflow. *Journal of Physics: Conference Series*, **75**(1), 012,063.

Tyacke, J. and **Tucker, P.**, **2015**: Large eddy simulation of turbine internal cooling ducts. *Computers & Fluids*, **114**, 130–140.

Wensink, H. H., **Dunkel, J.**, **Heidenreich, S.**, **Drescher, K.**, **Goldstein, R. E.**, **Löwen, H.** and **Yeomans, J. M.**, **2012**: Meso-scale turbulence in living fluids. *Proceedings of the National Academy of Sciences*, **109**(36), 14,308–14,313.

Wolf, A., **Lutz, T.**, **Würz, W.**, **Krämer, E.**, **Stalnov, O.** and **Seifert, A.**, **2015**: Trailing edge noise reduction of wind turbine blades by active flow control. *Wind Energy*, **18**(5), 909–923, wE-13-0068.R1.

Wu, J., **Liu, X.** and **Radespiel, R.**, **2016**: RANS simulations of a tandem nozzle supersonic wind tunnel. *Aerospace Science and Technology*, **49**, 215–224.

Yin, C., **Wu, T.** and **Kareem, A.**, **2016**: Synthetic turbulence: A wavelet based simulation. *Probabilistic Engineering Mechanics*, **45**, 177–187.

Zhang, Y., **Kung, E.** and **Haworth, D.**, **2005**: A PDF method for multidimensional modeling of HCCI engine combustion: effects of turbulence/chemistry interactions on ignition timing and emissions. *Proceedings of the combustion institute*, **30**(2), 2763–2771.

A Publications

A.1 Large-Eddy Simulations of realistic atmospheric turbulence with the DLR-TAU-code initialized by in situ airborne measurements.

Computers & Fluids 66 (2012) 121–129

Contents lists available at SciVerse ScienceDirect

Computers & Fluids

journal homepage: www.elsevier.com/locate/compfluid

Large-Eddy Simulations of realistic atmospheric turbulence with the DLR-TAU-code initialized by in situ airborne measurements

Torsten Auerswald [a,*], Jens Bange [a], Tobias Knopp [b], Keith Weinman [b], Rolf Radespiel [c]

[a] Center for Applied Geoscience, Universität Tübingen, Germany
[b] Institute of Aerodynamics and Flow Technology, German Aerospace Center, Germany
[c] Institute of Fluid Mechanics, Technische Universität Braunschweig, Germany

ARTICLE INFO

Article history:
Received 17 May 2011
Received in revised form 11 May 2012
Accepted 12 June 2012
Available online 21 June 2012

Keywords:
Large-Eddy Simulation
Atmospheric boundary layer
Synthetic turbulence

ABSTRACT

In this paper the numerical simulation of a turbulent flow in the atmospheric boundary layer (ABL) with a Large-Eddy Simulation (LES)-model is discussed. The results of this work are intended to be used for the numerical simulation of turbulent flows around an airfoil. To simulate the characteristics of the ABL flow and its influence on the airfoil realistically the flow upstream of the airfoil has to be turbulent with statistical properties that are comparable to those found in atmospheric measurements. To achieve this goal, a method to generate synthetic turbulent wind fields was used to initialize an LES model which is able to simulate the turbulent flow around an airfoil.

For the initial turbulent wind field to contain realistic statistics of atmospheric turbulence, data taken with the Helipod system are used. The Helipod is a helicopter-borne measurement probe that is able to take high-resolution measurements of temperature, wind vector and humidity. The statistical properties that are used as input parameters for the turbulence generator are the spectral energy, the correlation matrix and the variances of the three components of the wind vector.

The LES model used in this project is the flow solver TAU developed by the German Aerospace Center (DLR). TAU is a compressible computational fluid dynamics (CFDs) tool that is able to compute the flow around obstacles (e.g. parts of aircrafts or even whole aircrafts) on an unstructured grid. Calculations with TAU can be performed in Reynolds-Averaged Navier–Stokes-, LES- or Detached Eddy Simulation-mode using different sub-grid scale models.

1. Introduction

When simulating the flow around obstacles (e.g. aeroplanes or parts of aeroplanes) it is common to perform these simulations on unstructured grids [17]. These grids consist of an irregular pattern of geometrical shapes, e.g. tetrahedra, that is fitted to the shape of the obstacle around which the flow is simulated. The grid usually gets finer towards the obstacle. In particular when small radii of curvature occur a very high resolution is needed to represent the shape of the obstacle on the grid properly (see e.g. [18], for simulations of the flow around a wing-body configuration on an unstructured grid). In meteorological simulations of the atmospheric boundary layer (ABL), however, much coarser structured grids are used which allow for the coverage of a much larger domain. These simulations are usually performed from the earth surface up to an altitude of several kilometers for an area of several square kilometers with a grid spacing of a few 10 m (e.g. [10]).

The main interest of the work in this paper is to be able to simulate the interaction of the ABL with an airfoil. The problem occurring here is that the simulation of the flow around the airfoil alone needs too much resources for today's computers to perform a simulation of the whole ABL at the same time. To circumvent this problem not the full ABL is simulated. Instead only a small volume of the actual ABL is simulated within the computational fluid dynamics (CFDs)-model. To be able to simulate the influence of the ABL flow nevertheless a realistic 3D initial wind field is calculated. For the generation of this wind field statistical properties of measured data are taken as input for a synthetic turbulence generator. These statistical properties are the energy spectrum, the correlation tensor and the variances of wind speed. Even though this is, of course, not a complete representation of the statistics of the flow, some very important properties are considered. The resulting wind field is then used for the initialization of the CFD-simulation in which the flow around the airfoil is simulated. By using this method it is possible to simulate a turbulent flow and its influence on an airfoil at numerical costs that take into account the limitations of today's computers.

---

* Corresponding author. Address: Center for Applied Geoscience, Universität Tübingen, Sigwartstr. 10, 72076 Tübingen, Germany.
E-mail address: torsten.auerswald@uni-tuebingen.de (T. Auerswald).

0045-7930/$ - see front matter © 2012 Elsevier Ltd. All rights reserved.
http://dx.doi.org/10.1016/j.compfluid.2012.06.013

There are several studies addressing the problem of generating synthetic turbulence. Among these are Klein et al. [13] who developed a method for the generation of inflow data for LES. In their work a field with white noise is generated which is filtered in such a way that the resulting synthetic turbulence has a given length scale and correlation matrix. A method which is very similar is the one implemented by Kempf et al. [12]. This method also starts with the generation of white noise. Subsequently, a diffusion equation is applied until the synthetic turbulence has a given length scale. The resulting field can be modified in the same way as in Klein et al. [13] to obtain a given correlation matrix. Both methods are able to produce isotropic as well as anisotropic and inhomogeneous turbulent wind fields by spatial variation of the given length scale. The resulting turbulent velocity fields are not divergence-free which can lead to problems in compressible flow solvers. Furthermore, these two methods are not able to generate wind fields with a prescribed energy spectrum.

Druault et al. [6] suggested another algorithm for the generation of synthetic turbulence. In their paper a method for generating realistic inflow conditions for numerical models was presented that is based on proper orthogonal decomposition and linear stochastic estimation. This algorithm expects simultaneous measurements at several points in space. From these measurements the instantaneous wind field is reconstructed by inter- and extrapolations, respectively, and used as inflow data for a numerical flow solver. Unfortunately, simultaneous measurements at several points in space are rarely available in atmospheric measurements. Also, this method reconstructs only larger eddies (depending on the distance between the measurements), therefore the full spectrum of turbulent scales is not present in the synthetic turbulent wind field.

In the present work the method chosen is based on a Fourier approach where several waves with different wavenumbers are combined to build a random velocity field. This technique was first used by Kraichnan [15] and later adapted by e.g. Fung and Vassilicos [8] or Smirnov et al. [21]. The resulting velocity field is isotropic, Gaussian and reproduces a given energy spectrum. It can be further modified by applying the method by Lund et al. [16] to obtain a given anisotropic correlation matrix. Another work by Rosales and Meneveau [19] provides an algorithm to yield realistic non-Gaussian statistics while conserving the isotropy and energy spectrum of the velocity field.

2. Method

2.1. Generating the synthetic turbulent wind field

In this section the basic concept of the turbulence generator is presented. The velocity field is generated by calculating a Fourier series. In Fourier space several spectral velocity vectors are combined to build a turbulent vector field in position space. The basic equation is written as follows:

$$\vec{v}(\vec{x}) = \sum_{n=1}^{N}\sum_{m=1}^{N}\sum_{l=1}^{N}\left(\vec{C}_{n,m,l}\left(\cos(2\pi\cdot\vec{k}_{n,m,l}\cdot\vec{x}) + i\sin(2\pi\cdot\vec{k}_{n,m,l}\cdot\vec{x})\right)\right), \qquad (1)$$

where $\vec{v}$ is the velocity vector, $\vec{x}$ is the position vector, N is the total number of wavenumbers in every direction of the wavenumber space (due to the Nyquist-Theorem N should be chosen half the number of grid points M in one direction), $\vec{k}_{n,m,l}$ are the wavenumber vectors and $\vec{C}_{n,m,l}$ the complex amplitude vectors.

Unlike in earlier works using the Fourier approach (e.g. [8]), the direction of the wavenumber vectors are not random. Rather, every resolvable wavenumber vector is used to build the turbulent velocity field. By using only wavenumber vectors with resolvable components instead of wavenumber vectors with random directions any problems occurring with aliasing effects are eliminated. The randomness of the velocity field results only from the random direction of the Fourier coefficients. Furthermore, the complex Fourier series was chosen to allow for a faster calculation of the field with the help of a Fast Fourier Transform algorithm.

The amplitude vectors represent the spectral velocities for the corresponding wavenumber. The absolute values of these vectors are calculated from $E(|\vec{k}_{n,m,l}|)$, the spectral energy per wavenumber interval $\Delta|\vec{k}_{n,m,l}|$, which, e.g., can be calculated from measured time series:

$$|\vec{C}_{n,m,l}| = \sqrt{\frac{1}{Z_{n,m,l}}\cdot E(|\vec{k}_{n,m,l}|)\cdot\Delta|\vec{k}_{n,m,l}|}, \qquad (2)$$

where $Z_{n,m,l}$ is the number of occurrence of the same absolute values of $\vec{k}_{n,m,l}$ for all given combinations of n, m and l. The formulation in Eq. (2) applies for the general case of a 3D spectrum. In case of an 1D spectrum from e.g. time series measurements from an aircraft the $E(|\vec{k}_{n,m,l}|)$ is replaced by $E(k_{int})$. To calculate the wavenumbers k_{int} first the wavenumbers k_{1D} have to be calculated from the frequencies f and the true airspeed of the aircraft v_{TAS}:

$$k_{1D} = \frac{f}{v_{TAS}}. \qquad (3)$$

The energy values at k_{1D} are then interpolated on the available absolute values for the wavenumbers k_{int} according to the grid dimensions and the grid spacing.

In case of an energy spectrum calculated from measurements, the random fluctuations of that energy spectrum contribute an additional random effect to the synthetic wind field. To prevent aliasing problems the components of the wavenumber vectors $\vec{k}_{n,m,l}$ are chosen to be resolved by the given grid:

$$k_{(n,m,l)_x} = \frac{1}{L}\cdot n, \quad k_{(n,m,l)_y} = \frac{1}{L}\cdot m, \quad k_{(n,m,l)_z} = \frac{1}{L}\cdot l, \qquad (4)$$

with $L = M\cdot\Delta x$ being the size of the model domain, M the number of grid points in one direction ($M = 2\cdot N$, due to Nyquist's theorem) and Δx the grid spacing, which is taken to be constant in every direction.

Then the absolute values of $\vec{k}_{n,m,l}$ and the components of the unit vectors of $\vec{k}_{n,m,l}$ are only dependent on the indices n, m and l in the triple sum in Eq. (1):

$$|\vec{k}_{n,m,l}| = \sqrt{k^2_{(n,m,l)_x} + k^2_{(n,m,l)_y} + k^2_{(n,m,l)_z}}, \qquad (5)$$

$$e_{k_{(n,m,l)_x}} = \frac{k_{(n,m,l)_x}}{|\vec{k}_{n,m,l}|}, \quad e_{k_{(n,m,l)_y}} = \frac{k_{(n,m,l)_y}}{|\vec{k}_{n,m,l}|}, \quad e_{k_{(n,m,l)_z}} = \frac{k_{(n,m,l)_z}}{|\vec{k}_{n,m,l}|}. \qquad (6)$$

Sometimes, turbulent velocity fields are simulated with compressible flow solvers. In these cases the divergence of the velocity field plays an important role. If the divergence of the velocity field is non-zero, density fluctuations appear in the domain which propagate with the speed of sound. Since sound waves can often not be resolved by the model (because the grid spacing or time step is not small enough) this can lead to stability problems in the model. Therefore, it is an important feature for the random flow generator to produce divergence-free velocity fields in order to prevent the development of large density fluctuations in the model. Taking the divergence of the velocity field in Eq. (1) yields:

$$\nabla\cdot\vec{v}(\vec{x}) = \sum_{n=1}^{N}\sum_{m=1}^{N}\sum_{l=1}^{N}\left(2\pi\cdot\vec{k}_{n,m,l}\cdot\vec{C}_{n,m,l}\left(i\cos(2\pi\cdot\vec{k}_{n,m,l}\cdot\vec{x}) - \sin(2\pi\cdot\vec{k}_{n,m,l}\cdot\vec{x})\right)\right). \qquad (7)$$

The divergence of the generated velocity field is zero if the scalar product $\vec{C}_{n,m,l}\cdot\vec{k}_{n,m,l}$ is zero, which is the case if $\vec{C}_{n,m,l}$ and $\vec{k}_{n,m,l}$ are perpendicular. In Kraichnan [15], e.g., this is achieved by calculating random auxiliary vectors $\vec{f}_{n,m,l}$ that are equally distributed on the unit sphere:

$$\vec{f}_{n,m,l} = (\sin\theta_{n,m,l}\cos\phi_{n,m,l}, \sin\theta_{n,m,l}\sin\phi_{n,m,l}, \cos\theta_{n,m,l}), \tag{8}$$

with $\theta_{n,m,l}$ and $\phi_{n,m,l}$ being spherical coordinates for the unit sphere which are chosen randomly. To obtain vectors that are equally distributed on the unit sphere the azimuth angle ϕ is chosen equally distributed between 0 and 2π and the polar angle θ is defined by $\arccos(1-2R)$, where R is a random number equally distributed between 0 and 1.

For each wavenumber the vector product of the random auxiliary vector $\vec{f}_{n,m,l}$ and the unit vector of the wavenumber is calculated. The resulting unit vectors are equally distributed on the unit sphere and are perpendicular to the wavenumber vectors:

$$\vec{e}_{\vec{c}_{n,m,l}} = \frac{1}{|\vec{f}_{n,m,l} \times \vec{e}_{\vec{k}_{n,m,l}}|}\vec{f}_{n,m,l} \times \vec{e}_{\vec{k}_{n,m,l}}. \tag{9}$$

By applying the above equations a synthetic turbulent wind field is generated which contains isotropic turbulence with a prescribed energy spectrum $E(|\vec{k}_{n,m,l}|)$. Prescribed variances can be reproduced by scaling the velocity components:

$$v(\vec{x})_i = v(\vec{x})_i^{\text{gen}} \frac{\sqrt{\sigma_i^{\text{data}}}}{\sqrt{\sigma_i^{\text{gen}}}}, \tag{10}$$

with $i = 1, \ldots, 3$ denoting the three components of the wind vector, $v(\vec{x})_i^{\text{gen}}$ being the ith component of the velocity field generated by the turbulence generator, σ_i^{gen} being the variance of the ith component of the generated velocity field and σ_i^{data} being the variance of the ith component of the measured velocity time series.

2.2. Using input data from measurements

To generate a turbulent wind field with the turbulence generator presented in Section 2.1 an energy spectrum $E(|\vec{k}_{n,m,l}|)$ has to be prescribed. Here the energy spectrum is defined as $K/\Delta k$, where K is the spectral turbulent kinetic energy. That means this energy spectrum is a measure for the turbulent kinetic energy per wavenumber interval (also called spectral energy density [25]. The energy spectra used in this work are calculated from time series of wind velocity measured with the Helipod [2]. The Helipod is an airborne measurement probe which is attached to a helicopter. Several sensors (e.g. wind vector, temperature, humidity) are mounted for high-resolution measurements in the ABL. A large data set of measurements for different meteorological scenarios is available including atmospheric flow in various thermal stratifications (stable, very stable, neutral, convective).

The measurement data from the Helipod were taken during the LITFASS 2003 campaign [3] which was conducted in the north-east of Germany in Lindenberg near Berlin from May, 24th to June, 17th. The aim of this campaign was to measure turbulent fluxes over heterogeneous terrain in a convective boundary layer. For the generation of the synthetic turbulent wind field measurements from June, 2nd were chosen. On that day the weather at the measurement site was influenced by a high pressure system with its center located over the Baltic sea and a low over the eastern Atlantic. The warm front of the low just passed the region 1 day ago so that the measurement site was now located within the warm sector of the low. The profile of potential temperature (see Fig. 1) at 00 UTC shows a shallow nocturnal stable boundary layer and a residual layer resulting from the mixed layer of the previous day. At 6 UTC the surface temperature has decreased and the stable boundary layer has further grown in depth. In the morning hours the stable boundary layer vanished due to strong diabatic heating after sunrise. At 12 UTC a deep mixing layer has developed. At that time the convective boundary layer was already cloud-topped. The cloud amount was 4/8–5/8 Cumulus with 1/8 Altocumulus and 1/8 Cirrus at the measurement site and there was a weak south-easterly wind with wind speeds of approx. 4 m/s. The flight was performed between 10:21 UTC and 11:01 UTC. At that time the boundary layer height was approx. 1700 m. The measurements were taken at an altitude of approx. 100 m above the ground in the mixing layer of the ABL. In this part of the ABL the turbulent flow is homogeneous due to strong horizontal and vertical mixing. Therefore, the use of an homogeneous anisotropic initial wind field in the simulation of this scenario is justified. Furthermore, the synoptic-scale forcing was weak during the measurement flight making these measurements very useful to study the properties of the boundary layer.

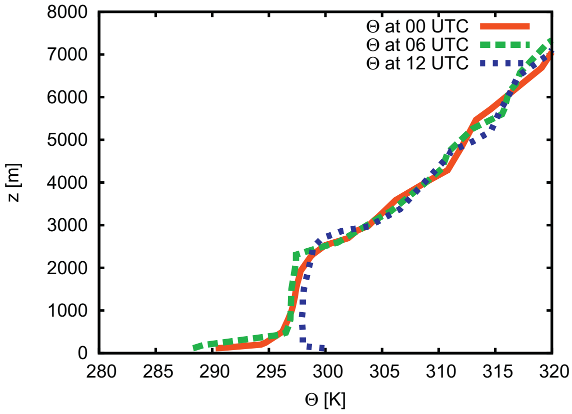

Fig. 1. Vertical profile of potential temperature at the measurement site near Lindenberg at 00 UTC (red, line), 06 UTC (green, dashed) and 12 UTC (blue, points). (For interpretation of the references to color in this figure legend, the reader is referred to the web version of this article.)

The measured data for the three wind components can now be used to calculate an energy spectrum which serves as input for the turbulence generator. For this purpose the measured spectrum is truncated at low frequencies so that only turbulent fluctuations with wavelength of the grid size of the turbulence generator and smaller are taken into account. When choosing the grid spacing for the 3D wind field one has to keep in mind that the Nyquist wavenumber for the 1D measurements is larger than for a 3D field with the same grid spacing. Therefore, if one wishes to use the Nyquist wavenumber of the 1D measurements as maximal resolvable wavenumber of the 3D grid the following has to be considered: Let Δx_m be the grid spacing of the 1D-measurements. Δx is the grid spacing of the 3D grid, with $\Delta x = \Delta y = \Delta z$. The Nyquist wavenumber of the 1D measurements is calculated by:

$$k_{\max} = \frac{1}{2\Delta x_m}. \tag{11}$$

According to the Nyquist theorem the maximal According to the Nyquist theorem the maximal wavenumber that is resolvable with a cubic grid is:

$$k_{\max} = \sqrt{k_{x_{\max}}^2 + k_{y_{max}}^2 + k_{z_{\max}}^2}, \tag{12}$$

$$= \sqrt{\frac{1}{4\Delta x^2} + \frac{1}{4\Delta y^2} + \frac{1}{4\Delta z^2}}, \tag{13}$$

$$= \sqrt{3}\frac{1}{2\Delta x} = \frac{1}{2\Delta x_m}. \tag{14}$$

Therefore, to resolve the Nyquist wavenumber of the 1D measurements the grid spacing of the 3D grid needs to be chosen as:

$$\Delta x = \sqrt{3}\Delta x_m. \tag{15}$$

Since the resolution in wavenumber space is different for the measurements and the 3D grid the energy values at the wavenumbers resolved by the measurements are interpolated to obtain the energy values for the wavenumbers resolved by the model grid.

2.3. Modification for anisotropic turbulence

By using the method of Lund et al. [16] it is possible to produce turbulent wind fields with given anisotropic statistics. The anisotropic wind field is constructed by applying a transformation tensor to the isotropic wind field:

$$v(\vec{x})_i^{\text{aniso}} = a_{ij} \cdot v(\vec{x})_j^{\text{iso}}. \tag{16}$$

The transformation tensor a is defined as:

$$a = \begin{pmatrix} \sqrt{R_{11}} & 0 & 0 \\ R_{21}/a_{11} & \sqrt{R_{22} - a_{21}^2} & 0 \\ R_{31}/a_{11} & (R_{32} - a_{21}a_{31})/a_{22} & \sqrt{R_{33} - a_{31}^2 - a_{32}^2} \end{pmatrix}, \tag{17}$$

where R is the given correlation tensor, e.g. calculated from measurements, that is imposed on the velocity field. The correlations of the resulting velocity field $v_{i_{n,m,l}}^{\text{aniso}}$ are equal to R_{ij}.

2.4. Calculation of the density and pressure field

The turbulence generator only delivers a turbulent wind field, therefore an initial density and pressure field has to be calculated to start a numerical simulation. Since a compressible flow solver is used (see Section 3.1 for details) the simulation is very sensitive to the initial thermodynamic fields. A good guess for the density and pressure field can be made by applying the Bernoulli equation which gives a relation between wind speed and density or pressure, respectively. The equations are:

$$p = p_\infty \left(1 + \frac{\gamma - 1}{2}\text{Ma}^2\right)^{\frac{\gamma}{1-\gamma}}, \tag{18}$$

$$\rho = \rho_\infty \left(1 + \frac{\gamma - 1}{2}\text{Ma}^2\right)^{\frac{1}{1-\gamma}}, \tag{19}$$

with p_∞ and ρ_∞ being the reference values for pressure and density, $\gamma = c_p/c_v$ the adiabatic coefficient and $\text{Ma} = |\vec{v}|/c$ the Mach number (c being the speed of sound).

3. Numerical simulations

3.1. The DLR TAU-Code

The CFD method used is the DLR TAU-Code [9,20]. The TAU code is a three-dimensional finite volume scheme for hybrid grids. The solver uses an edge-based dual-cell approach, i.e. the method is of cell-centered type with respect to the dual-mesh cells. Viscous fluxes are discretized by central differences. Inviscid fluxes are calculated using a central method with artificial dissipation of scalar or matrix type. For time discretization, a second-order backward differencing formula is used together with the dual time stepping approach. Within each time step, the arising nonlinear problems are solved using either a semi-implicit lower–upper symmetric Gauss–Seidel (LU-SGS) method or a low-storage explicit Runge–Kutta scheme. A multigrid scheme of full approximation scheme type and residual smoothing are used for convergence acceleration.

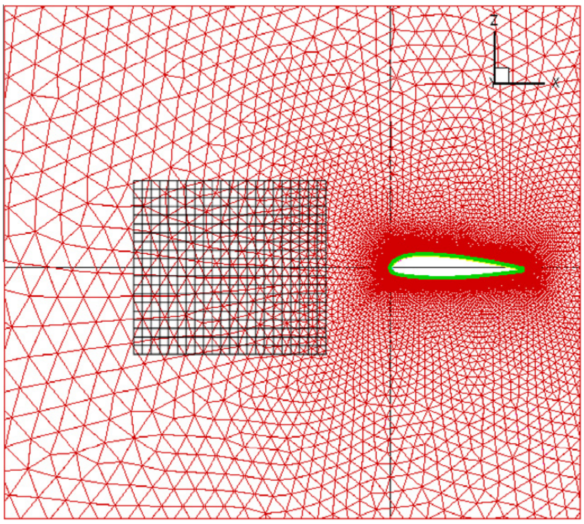

Fig. 2. Sketch of the 3D model domain for the simulations of the interaction of the turbulent flow with the airfoil. The primary grid (red) is an unstructured grid that is fitted around the airfoil while the secondary grid (black) is a cartesian grid in front of the airfoil.

For turbulence modeling, the SAO-DES model is used (see [22] or [11]). In the present test case of decaying turbulence, due to the absence of walls, the RANS switch of the DES is deactivated and the SAO-DES behaves as a sub-grid scale model in LES. Numerical schemes used for LES of compressible flow need to be both low-dissipative and stable. In order to avoid excessive dissipation at the large wave number range of the spectrum, we use matrix dissipation [26] and dissipation scaling according to [7]. The inviscid fluxes are discretized using the skew symmetric form.

3.2. Numerical settings and strategy

The simulation strategy for the turbulent flow around the airfoil is sketched in Fig. 2. The model domain comprises two grids, an unstructured grid (red) that is fitted to the airfoil (green) and a cartesian grid (black) for the simulation of the turbulent flow upstream of the airfoil. The cartesian grid is moved towards the airfoil. In a short distance to the airfoil the turbulent flow is passed to the unstructured grid where the flow can interact with the airfoil. The interaction between the grids is realized by using the Chimera-technique [20,27]. For the simulations described in this paper only the cartesian grid is used to make sure that the prescribed statistics of the turbulent flow are preserved well and the numerical scheme is stable. The cartesian domain is approximately of size $350^3\,\text{m}^3$ using a cartesian equidistant mesh with $500 \times 500 \times 500$ nodes. The boundary conditions used for the simulations are periodic boundaries in x-direction and symmetric boundaries in y- and z-direction. These boundary conditions were chosen according to experience made in the EU-Project “Detached Eddy Simulation for Industrial Aerodynamics” (DESider). Within this project it was found that these boundary conditions have the least influence on the flow in the model domain. The model is run with a physical time step of 0.001 s and the total simulation time is 3 s. Within each time step, 40 inner iterations are performed using the Backward-Euler scheme. To accelerate the convergence to a steady state the multigrid method using a 4th level W-cycle is used.

4. Results

4.1. The synthetic wind field

A turbulent wind field was generated using the turbulence generator presented in Section 2.1. The input statistics for the turbulence generator were calculated from measurements from the LITFASS 2003 campaign [3] which was conducted in the north-east of Germany in Lindenberg near Berlin from May, 24th, to June, 17th. The energy spectrum calculated from the measurements on June, 2nd is shown in Fig. 3 (green, dashed). It shows the $k^{-5/3}$ slope of the inertial subrange of locally isotropic turbulence [14] over the whole wavenumber range. The spectrum from the synthetic wind field (red line in Fig. 3) matches the input spectrum from the Helipod measurements very well (in Fig. 3 the spectrum from the synthetic field was multiplied by a factor of 50 for better visibility). Even the sharp peaks at high wavenumbers (between $k = 0.3$ m^{-1} and $k = 1$ m^{-1}), caused by sound waves generated by the helicopter blades [1] during the Helipod measurement, were reproduced. It is obvious that it cannot cover the large scales from the measurements since the model domain has a size of only 350 m (500 points in each direction, grid spacing of 0.7 m) while the Helipod flight leg had a length of about 4600 m.

The synthetic wind field was modified to obtain the anisotropic wind correlations from the measurement data using Eq. (17). The correlation matrices from the measurement data and from the synthetic wind field as shown in Table 1 are in good agreement as well as the variances which, due to the scaling of the wind field (Eq. (10)), match the given variances perfectly.

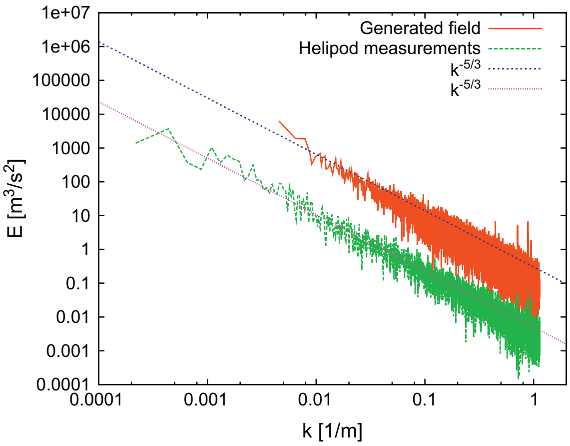

Fig. 3. Energy spectrum of the generated synthetic wind field (red line) and the spectrum of the Helipod measurements (green, dashed) that was used as input for the turbulence generator. The spectrum of the synthetic wind field is multiplied by factor 50 for better visibility of the two spectra. For comparison the $k^{-5/3}$ slope is plotted (blue, pink, dotted).

Table 1
Correlation matrices calculated from the Helipod measurements (left) and the synthetic wind field (right).

	u	v	w
Helipod measurements			
u	1	0.087	0.119
v	0.087	1	−0.004
w	0.119	−0.004	1
Generated field			
u	1	0.079	0.097
v	0.079	1	−0.005
w	0.097	−0.005	1

4.2. TAU simulations

Using the results presented in Section 4.1 it is now possible to initialize the TAU model with a three-dimensional turbulent wind field that possesses important statistical properties of a real ABL flow. In order to make sure TAU gives good results for the simulation of the turbulent wind field the model is run in LES mode first. In these simulations only the secondary grid (cp. Fig. 2) is considered. To show the dependency of the results on the grid spacing an additional run with twice the grid spacing was performed. These results can be found in Appendix A.

Fig. 4 compares the energy spectrum of the initial wind field with the spectrum after 3 s of simulation time. There is a massive loss of energy in the small scales between about 0.3 m^{-1} and 1.2 m^{-1} due to numerical dissipation. This affects eddies of the size of $1 \cdot \Delta x$ to about $4 \cdot \Delta x$ (Δx being the grid spacing). The loss of these turbulent scales is the common behavior of LES-models and was expected. Scales larger than $4 \cdot \Delta x$ are preserved very well. The energy spectrum after 3 s is shifted to lower energy and follows in average the $k^{-5/3}$ slope nearly over the entire wavenumber range. The significant troughs in the spectrum after 3 s occur because the indices in Eq. (1) begin with 1. Therefore, components of the wavenumber vector with index 0 (representing the average value in the respective direction) are not present in the velocity field. During the simulation energy is transferred to these wavenumbers resulting in the troughs visible in Fig. 4.

Fig. 5 shows the simulation results for the variances and correlations of the velocity components. Due to the large size of the dataset, time steps were written only every 0.5 s. From Fig. 5 (right) it can be seen that the correlations of the velocity components change significantly. Previous experiments have shown that the flow in anisotropic decaying turbulence tends towards the isotropic state [4]. For R_{uv} and R_{uw} the absolute value of correlation increases significantly at the beginning. Towards the end of the simulation the absolute value decreases to very small correlations. For R_{vw} this is not the case. The absolute value of the correlation of v and w increases for nearly every time step. The reason for this behavior could be inconsistencies between the flow field and the pressure and density field, respectively, which are guessed from the flow field by applying the Bernoulli equation (see Section 2.4) and and are not guaranteed to match the flow field exactly in the sense of the Navier–Stokes equations. Furthermore, the simulated time period is very short. In Chung and Kim [5] a time scale is given that estimates the time it takes for an anisotropic decaying turbulent flow field to return to the isotropic state. The time scale is

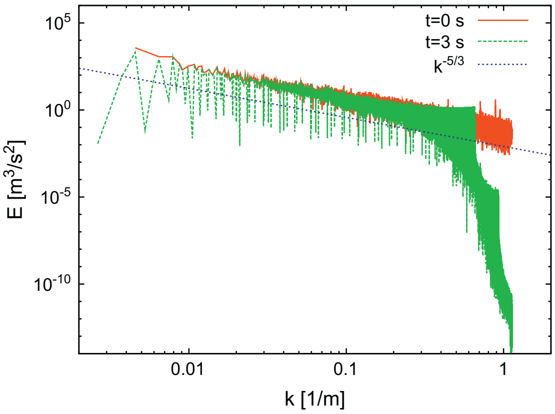

Fig. 4. Energy spectra of the simulations with TAU. Depicted is the spectrum of the initial wind field (red line) and after 3 s simulation time (green, dashed). For comparison the $k^{-5/3}$ slope is plotted (blue, dotted).

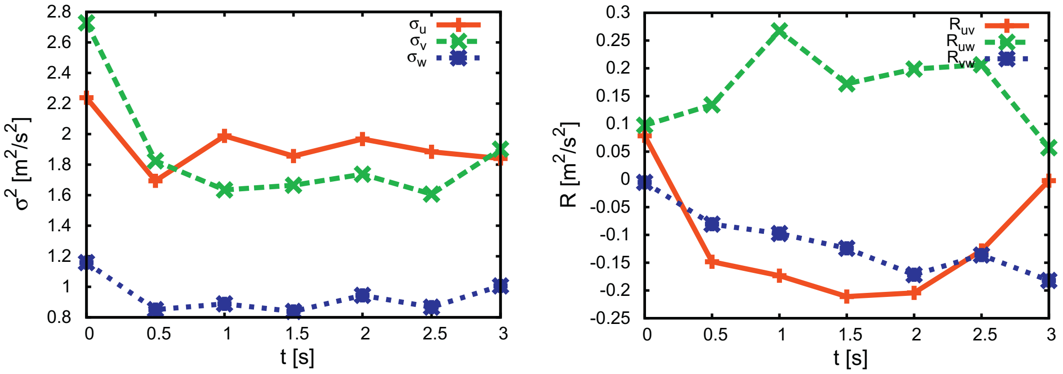

Fig. 5. Timely development of variances (left) and cross-correlations (right) during the TAU-simulation. In the left plot the variances of *u* (plus, red), *v* (cross, green) and *w* (asterisks, blue) are plotted. The left plot shows the cross-correlations of *u* and *v* (plus, red), *u* and *w* (cross, green) and *v* and *w* (asterisks, blue). (For interpretation of the references to color in this figure legend, the reader is referred to the web version of this article.)

calculated by considering the spectral energy and the spectral rate of strain. According to this time scale it would take about 99 s for the initial turbulent flow field in this simulation to return to the isotropic state. Since the fluctuation of the cross-correlations are very strong within this short 3 s period of simulated time it is not possible to make a statement about whether the flow tends towards isotropy or not.

The variances of the velocity components (Fig. 5, left) show a strong decrease in the first 0.5 s reflecting the loss of turbulent kinetic energy. Afterwards the variances alternate around a constant level, although due to the few time steps plotted, it is not possible to make a precise statement about the trend of the curve. The overall decrease of variances with time is also noticeable in the plots of the probability density functions (PDFs) of the velocity components (Fig. 6) where the PDFs become narrower with time since the large velocity values occur less often.

An important feature of the ABL is the intermittency of the turbulent flow. This effect can be seen in the PDF of the difference of

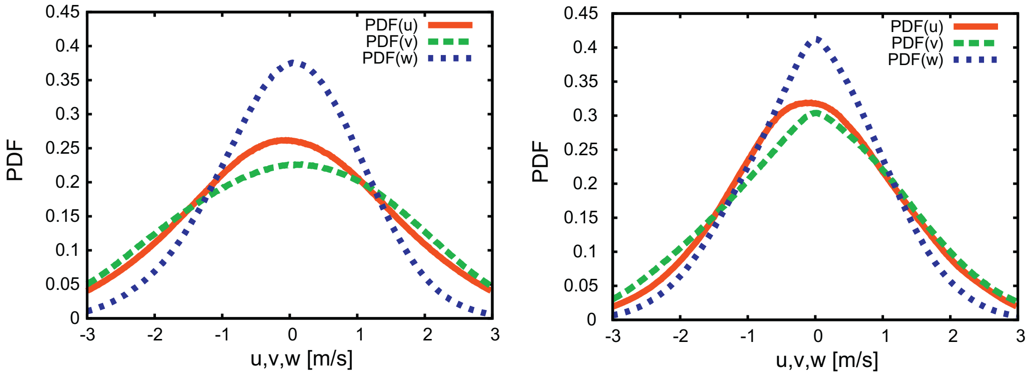

Fig. 6. Probability density function calculated from the three components of the velocity in the initial wind field (left) and the TAU result after 3 s of simulation (right). (For interpretation of the references to color in this figure legend, the reader is referred to the web version of this article.)

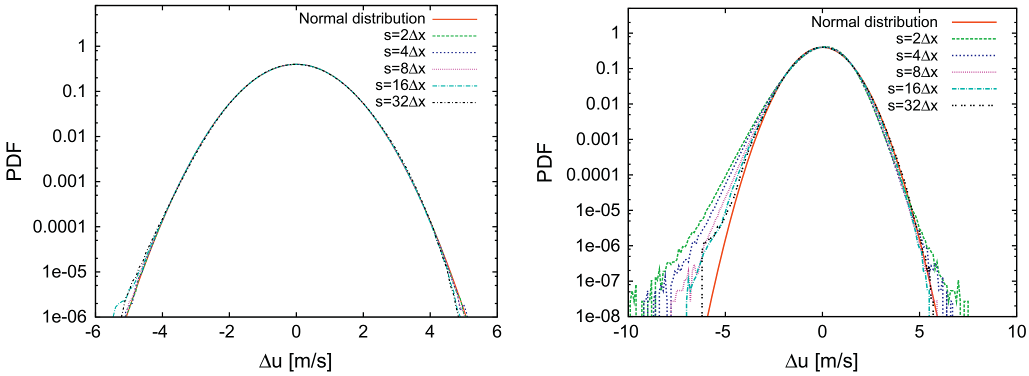

Fig. 7. Normalized longitudinal PDF of the increments of the *x*-component of the velocity calculated from the initial wind field (left) and the TAU result after 3 s (right) for separation distances $s = 1.4$ m (green), $s = 2.8$ m (blue), $s = 5.6$ m (purple), $s = 11.2$ m (light blue) and $s = 22.4$ m (black). For comparison the PDF of the normal distribution is plotted in red.

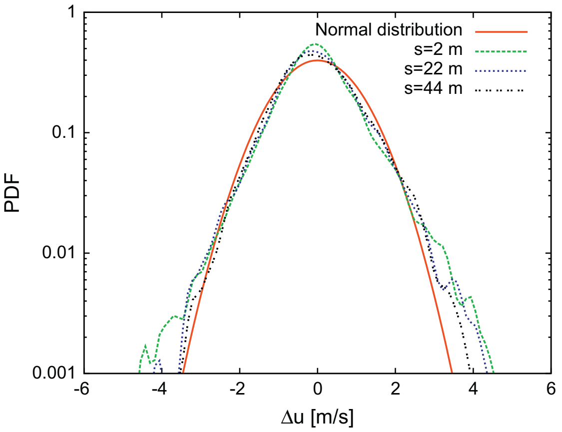

Fig. 8. Normalized longitudinal PDF of the increments of the *x*-component of the velocity calculated from the Helipod measurements for separation distances $s = 2$ m (green), $s = 22$ m (blue) and $s = 44$ m (black). For comparison the PDF of the normal distribution is plotted in red.

the velocity over a certain separation distance. Due to intermittent fluctuations the PDF of velocity increments deviates from the PDF of the normal distribution by having tails on the left and right end of the function (see e.g. [23], for a short summary on intermittency). Fig. 7 (left) shows the longitudinal PDF of the velocity increments of the initial wind field. For all separation distances the PDFs are Gaussian. After 3 s however, the PDF of the velocity increments has adapted to a more realistic state (see Fig. 7, right). As supported by previous publications using experimental data (see [24], for a summary of some experimental results) the longitudinal PDFs of the velocity increment show negative skewness and significant tails for separation distances smaller than the integral length scale. Due to sudden bursts occurring in intermittent flows strong events are much more likely than in a Gaussian distribution which is represented by an increase of the PDF at the left and right end of the distribution. Also visible is that, like in real flows, the PDF of the increments of the velocity becomes more Gaussian with larger separation distances. For a separation distance of 32 times the grid spacing the PDF is nearly Gaussian.

For completeness the longitudinal PDFs of the velocity increments calculated from the Helipod measurements are plotted in Fig. 8. Even though the initial field for the TAU simulation was derived from the Helipod measurements the PDFs of the measurements and the simulation after 3 s are different. The deviation from the normal distribution is much weaker in the PDFs of the measurements. Also the skewness is very small and seems to be positive which would be contrary to the theory (e.g. in [14]) and results from previous measurements. The reason for these differences is not clear. Like in the PDFs of the simulation the PDFs of the measurements become more Gaussian with larger separation distances. It has to be mentioned though that in the simulation the PDF for a separation distance of 22.5 m is nearly perfectly Gaussian while in the PDF of the measurements Gaussianity is reached at much larger separation distances. This effect could be due to a larger integral scale in the measurements. Since the model domain comprises only 350 m^3 the integral scale is smaller in the simulation than in the measurements.

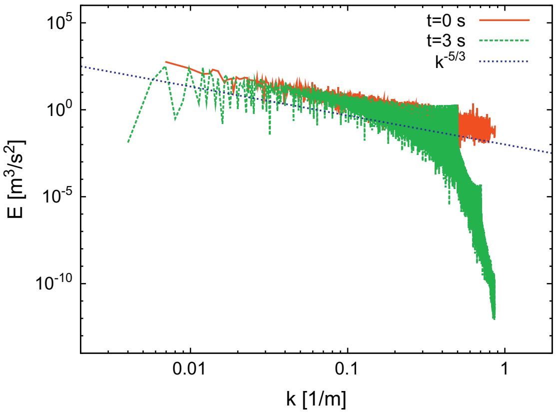

Fig. A.9. Energy spectra of the simulations with TAU on the coarse grid. Depicted is the spectrum of the initial wind field (red line) and after 3 s simulation time (green, dashed). For comparison the $k^{-5/3}$ slope is plotted (blue, dotted).

5. Conclusion

This project aims at simulating a part of the ABL with the compressible flow solver TAU on an unstructured grid. The motivation for these simulations is to be able to model the interaction of a atmospheric turbulent flow with an airfoil in future simulations. For this purpose a realistic atmospheric flow has to be established in the model domain. Since 3D measurements of the ABL do not exist for the range of scales needed for the simulations in this project an algorithm was used to generate synthetic initial wind fields. For the generation of these wind fields statistics of 1D measurement data were calculated and used as input for the turbulence generator presented in Section 2.1. It was shown in Section 4.1 that with this method it is possible to generate synthetic turbulent wind fields possessing some important features of realistic atmospheric turbulence like energy spectrum, variances and correlations. The statistics of these wind fields are anisotropic. In Section 4.2 first results from simulations with the CFD solver TAU were presented showing the general ability to initialize TAU with the generated wind fields. The results show that the key features of the flow are well preserved within a 3 s-simulation and in addition develops realistic PDFs of the velocity increments during the simulation. The results of the flow simulation show statistics of intermittent flows. Only the timely development of the correlation of the velocity components showed large fluctuations and seemed to be not in line with the theory of the return-to-isotropy of an anisotropic flow. This is could be due to an initial mismatch of the density field and pressure field with the velocity field. Since the density and pressure field were guessed by applying bernoulli's equation (Section 2.4 they cannot fully match the velocity field in the sense of the Navier–Stokes-Equations. Furthermore, it is hard to make any statement regarding the timely development of the correlations, since the approximated return-to-isotropy time is much larger than the simulated time (99 s vs. 3 s) and therefore the fluctuations observed may not represent the long-term trend in a longer simulation. This question could only be adressed in a much longer simulation which cannot be afforded considering the large model domain and the fine grid. Nevertheless, we believe that this method of simulating turbulent flows is well suited for further simulations on a Chimera grid (described in Section 3.2) where the generated turbulent flow can actually interact with an airfoil and the influence of a realistic boundary layer flow on the airfoil can be studied for different weather situations.

Acknowledgments

The authors of this paper gratefully acknowledge the support by the 'Deutsche Forschungsgemeinschaft DFG' (German Research Foundation) that funded this research within the DFG FOR 1066. We also thank the "North-German Supercomputing Alliance"

(HLRN) for providing the resources to perform the simulations presented in this paper.

Appendix A. Results of the TAU simulation on the coarse grid

To estimate the influence of the grid spacing on the results of the simulation an additional run with doubled grid spacing ($\Delta x = 1.4$ m) and 250 grid points in each direction was performed. The model setup and domain size of this run is identical to the run with $\Delta x = 0.7$ m. In Fig. A.9 the energy spectrum of the initial wind field and the wind field after 3 s simulation time on the coarse grid is plotted. Like on the finer grid there is a massive loss of energy in the smallest scales. On the coarse grid the energy drop starts at ca. 0.15 m^{-1} which corresponds to a wavelength of approx. four times the grid spacing. The scales larger than that are preserved very well and follow the $k^{-5/3}$-slope of the inertial subrange.

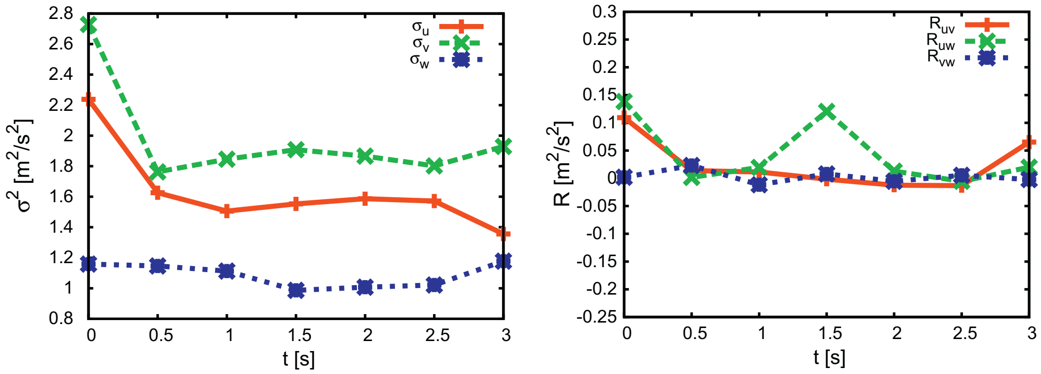

Fig. A.10. Timely development of variances (left) and cross-correlations (right) during the TAU-simulation on the coarse grid. In the left plot the variances of u (plus, red), v (cross, green) and w (asterisks, blue) are plotted. The left plot shows the cross-correlations of u and v (plus, red), u and w (cross, green) and v and w (asterisks, blue). (For interpretation of the references to color in this figure legend, the reader is referred to the web version of this article.)

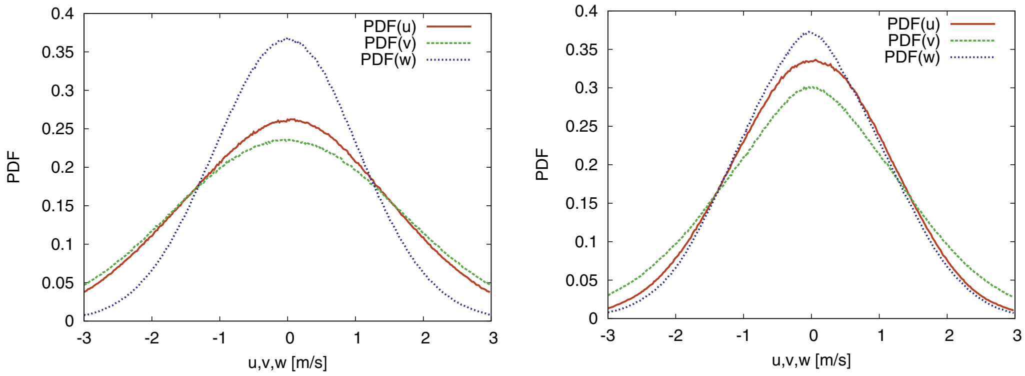

Fig. A.11. Probability density function calculated from the components of the velocity in the initial wind field (left) and the TAU result after 3 s of simulation (right) on the coarse grid. (For interpretation of the references to color in this figure legend, the reader is referred to the web version of this article.)

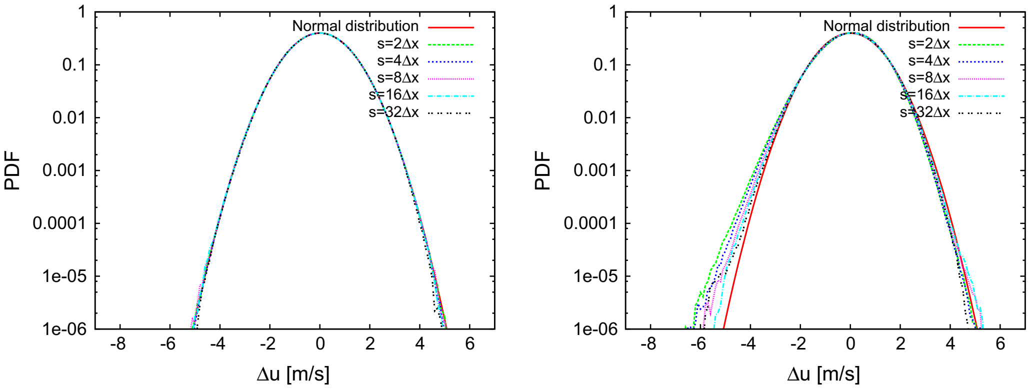

Fig. A.12. Normalized longitudinal PDF of the increments of the x-component of the velocity calculated from the initial wind field (left) and the TAU result after 3 s (right) on the coarse grid. Depicted are separation distances s = 1.4 m (green), s = 2.8 m (blue), s = 5.6 m (purple),s = 11.2 m (light blue) and s = 22.4 m (black). For comparison the PDF of the normal distribution is plotted in red.

Fig. A.10 shows the timely development of the correlations and variances of the velocity components in the simulation on the coarse grid. Like in the run on the fine grid there is no clear trend visible in the correlations of the velocity. The time scale for the return to isotropy is 43 s in this simulation. That means that, like on the fine grid, for this short period of simulation time it is not possible to make a statement whether the turbulent flow returns to isotropy or not. The behavior of the variances looks quite similar to the run on the fine grid with a significant decrease in the first 0.5 s and a more or less constant behavior after that.

The decrease of energy is also visible in the PDFs of the velocity components (s. Fig. A.11). The PDFs are normally distributed. After 3 s simulation time the distribution becomes narrower and the maximum value is higher. The same behavior could be seen in the simulation on the fine grid and reflects the fact that, due to the decrease of kinetic energy, there are less large values and more small values of wind velocity.

The PDFs of the increments of the velocity components show a similar behavior in the run on the coarse grid and the fine grid. As supported by previously published papers (e.g. in [23]) there are tails at both ends of the distributions. The distributions are skewed with a wider tail at negative velocity increments. For small separation distances the skewness is large and becomes smaller for larger separation distances. For the separation distance $s = 32\Delta x$ the distribution is nearly Gaussian (see Fig. A.12).

The simulation on the coarser grid shows results that are comparable to the simulation on the fine grid. In both cases a strong decrease of energy in the smallest scales could be seen in the energy spectra. The decrease starts at a wavelength of around $4\Delta x$. Narrower PDFs of the velocity components reflect the decrease in variance which is caused by the decaying turbulent kinetic energy. In both simulations the skewed PDFs of the velocity increments develop with larger skewness for smaller separation distances and smaller skewness for larger separation distances. The comparison of the runs on the fine and coarse grid clearly show that there are no qualitative differences in the results. Therefore, the results on the fine grid are not influenced by the grid size.

References

[1] Bange J, Roth R. Helicopter-borne flux measurements in the nocturnal boundary layer over land – a case study. Boundary-Layer Meteorol 1999;92:295–325.
[2] Bange J, Spieß T, van den Kroonenberg A. Characteristics of the early-morning shallow convective boundary layer from Helipod flights during stinho-2. Theor Appl Climatol 2007;90:113–26.
[3] Bange J, Spieß T, Herold M, Beyrich F, Hennemuth B. Turbulent fluxes from Helipod flights above quasi-homogeneous patches within the LITFASS area. Boundary-Layer Meteorol 2006;121:127–51.
[4] Choi K-S, Lumley JL. The return to isotropy of homogeneous turbulence. J Fluid Mech 2001;436:59–84.
[5] Chung MK, Kim SK. A nonlinear return-to-isotropy model with reynolds number and anisotropy dependency. Phys Fluids 1995;7(6):1425–37.
[6] Druault P, Lardeau S, Bonnet J-P, Coiffet F, Delville J, Lamballais E, et al. AIAA J 2004;42:447–56.
[7] Ducros F, Ferrand V, Nicoud F, Weber C, Darracq D, Gacherieu C, et al. Large-Eddy simulation of the shock/turbulence interaction. J Comput Phys 1999;152:517–49.
[8] Fung JCH, Vassilicos JC. Two-particle dispersion in turbulent like flows. Phys Rev E 1998;57:1677–90.
[9] Gerhold T, Friedrich O, Galle M. Calculation of complex three-dimensional configurations employing the DLR-tau-code. AIAA-97-0167; 1997.
[10] Gryschka M, Drüe C, Etling D, Raasch S. On the influence of sea-ice inhomogeneities onto roll convection in cold-air outbreaks. Geophys Res Lett 2008;35.
[11] Haase W, Braza M, Revell A. DESider a european effort on hybrid RANS-LES modelling: results of the European-Union Funded Project, 2004–2007. Springer Publishing Company, Incorporated; 2009.
[12] Kempf A, Klein L, Janicka J. Efficient generation of initial- and inflow-conditions for transient turbulent flows in arbitrary geometries. Flow Turb Combust 2005;74:67–84.
[13] Klein M, Sadiki A, Janicka J. A digital filter based generation of inflow data for spatially developing direct numerical or large Eddy simulations. J Comput Phys 2003;186:652–65.
[14] Kolmogorov AN. Energy dissipation in locally isotropic turbulence. Dokl AN SSSR 1941;32:19–21.
[15] Kraichnan RH. Diffusion by a random velocity field. Phys Fluids 1970;13:22–31.
[16] Lund TS, Wu X, Squires KD. Generation of turbulent inflow data for spatially-developing boundary layer simulations. J Comput Phys 1998;140:233–58.
[17] Mavriplis DJ. Unstructured grid techniques. Ann Rev Fluid Mech 1997;29:473–514.
[18] Rakowitz M, Eisfeld B, Schwamborn D, Sutcliffe M. Structured and unstructured computations on the DLR-F4 wing-body configuration. J Aircraft 2003;40:256–64.
[19] Rosales C, Meneveau C. A minimal multiscale lagrangian map approach to synthesize non-gaussian turbulent vector fields. Phys Fluids 2006:18.
[20] Schwamborn D, Gerhold T, Heinrich R. The DLR TAU-Code: recent applications in research and industry. ECCOMAS CFD; 2006.
[21] Smirnov A, Shi S, Celik I. Random flow generation technique for large Eddy simulations and particle-dynamics modeling. J Fluids Eng 2001;123:359–71.
[22] Spalart PR, Jou W-H, Strelets M, Allmaras SR. Comments on the feasibility of LES for wings, and on a hybrid RANS/LES approach. In: Proceedings of first AFOSR international conference on DNS/LES; 1997.
[23] Sreenivasan KR. Fluid turbulence. Rev Modern Phys 1999;71:383–95.
[24] Sreenivasan KR, Antonia RA. The phenomenology of small-scale turbulence. Annu Rev Fluid Mech 1997;29:435–72.
[25] Stull RB. An introduction to boundary layer meteorology. Kluwer Academic Publishers; 1989. 670p, ISBN: 90-227-2969-4.
[26] Swanson RC, Turkel E. On central-difference and upwind schemes. J Comput Phys 1992;101:292–306.
[27] Wolf C, Raichle A, Knopp T, Schwamborn D. Chimera simulations of transported large-scale vortices and their interaction with airfoils. In: New results in numerical and experimental fluid mechanics VII. Notes on numerical fluid mechanics and multidisciplinary design, vol. 112. Berlin/Heidelberg: Springer; 2010. p. 117–24.

A.2 Comparison of two methods simulating highly resolved atmospheric turbulence data for study of stall effects

Computers & Fluids 108 (2015) 57–66

Contents lists available at ScienceDirect

Computers & Fluids

journal homepage: www.elsevier.com/locate/compfluid

Comparison of two methods simulating highly resolved atmospheric turbulence data for study of stall effects

Christoph Knigge [a,*], Torsten Auerswald [b], Siegfried Raasch [a], Jens Bange [b]

[a] Institute of Meteorology and Climatology, Leibniz Universität Hannover, Germany
[b] Center for Applied Geoscience, Universität Tübingen, Germany

ARTICLE INFO

Article history:
Received 20 September 2013
Received in revised form 30 October 2014
Accepted 4 November 2014
Available online 20 November 2014

Keywords:
LES
PALM
Atmospheric boundary layer
Aircraft
Synthetic turbulence

ABSTRACT

We compare two different methods that provide highly resolved three-dimensional turbulent wind fields for numerical investigations of stall effects. The first is computationally very expensive and explicitly simulates the turbulent wind fields using large-eddy simulation (LES). The second method generates synthetic three-dimensional turbulent wind fields from one-dimensional time series data from flights in the atmosphere. The synthetic method is comparatively fast and cheap but reproduces only statistical features of the turbulent flow.

Since the focus in this study lies on the two methods by themselves, data generation is based on the same numerical simulation. The synthetic fields were generated from time series data obtained from virtual flight measurements within the LES. Different meteorological scenarios were analyzed in order to examine the influence of the different driving forces on the results.

Horizontally averaged turbulence parameters of the compared fields are in good agreement. Parameters are independent of height in the synthetic flow fields since the time series used for the generation do not contain height information. In the case of a stably stratified boundary layer, the velocity fluctuations have a near-Gaussian distribution and are therefore well-reproduced by the synthetic method. Although provided with the time series, the synthetic flow fields cannot generate the non-Gaussian distribution of the vertical velocity in case of the analyzed convective boundary layers. Angles of attack of a virtual airplane calculated with the vertical velocity of wind fields generated with the two different methods show large differences. The consequences of these findings for applications will be investigated in a future study by numerical simulation of the flow around wings initialized with the different velocity fields.

1. Introduction

In aviation, a stall describes a flow condition where a certain critical angle of attack (stall angle of attack) leads to a separation of the flow from an airfoil and thus to a decrease in lift. Especially during landing, the risk of stall limits the range of safe aircraft flights. Thus, the value of the angle of attack along the flight path of an aircraft is important for the investigations of stall effects (see e.g. [1,2] for a detailed description of the physics of stall).

A better knowledge of the angle of attack and stall limits is an important task to optimize air traffic. For example, it may allow for lower aircraft speed, which reduces noise and may allow for more flights. Moreover, the investigations on stall effects require numerical simulations of the flow around wings and nacelles, due to the high risk and cost of real flight experiments. For these investigations, it is essential to initialize computational fluid dynamics (CFD) models with atmospheric turbulence data. The rapidly changing turbulent flow in the atmospheric boundary layer (ABL) may strongly affect the stall of aircraft. Turbulence is highly influenced by the surface heterogeneity and radiation which is in turn controlled by clouds and the diurnal cycle. The ABL ranges in height from some hundred meters to 2–3 km. The turbulence is usually non-Gaussian distributed, and coherent structures develop which strongly depend on height (e.g. [3]).

Usually, the numerical models used for the simulation of flows around wings and nacelles provide atmospheric data only with the help of statistical models (e.g. [4–6]). These statistical models mostly use a Dryden or von Kàrmàn velocity spectrum where only two parameters control the generated turbulent flow. Therefore, they cannot account for the complexity of real atmospheric turbulence within the ABL.

---

[*] Corresponding author at: Institute of Meteorology and Climatology, Leibniz Universität Hannover, Herrenhäuser Straße, 30419 Hannover, Germany.

E-mail address: knigge@muk.uni-hannover.de (C. Knigge).

http://dx.doi.org/10.1016/j.compfluid.2014.11.005
0045-7930/

The purpose of this study is to compare two different methods that produce highly resolved three-dimensional atmospheric turbulent wind fields. The first method uses large-eddy simulation (LES) and explicitly simulates three-dimensional turbulent wind fields of a realistic ABL; hereafter named the LES method. The second method generates synthetic three-dimensional fields using statistical quantities. These quantities can e.g. be derived from one-dimensional horizontal flight measurements (time series data) in the atmosphere. Hereafter, this procedure is named the synthetic method. It was discussed in detail by Auerswald et al. [7], who used the synthetically generated flow field to initialize an LES model capable for the simulation of the turbulent flow around a wing.

With the LES method presented here it is possible to simulate turbulent flows that typically occur in the lower atmosphere. High-resolution simulations with the LES model which contain turbulent structures affecting wings are computationally very expensive. In contrast, the synthetic method is comparatively fast. It uses a huge database of different meteorological scenarios collected during various flight experiments all over the world, but it reproduces only statistical features of the atmospheric turbulent flow. Hence, the main objective is to determine the differences in wind fields generated by these two methods. Ideally, the synthetic method as well as the LES method should produce wind fields that show the same features of the ABL, in case the same meteorological conditions are considered.

Since we want to investigate the methods by themselves we replaced the real flight measurements used for the synthetic method by virtual flight measurements that were carried out within the simulated wind fields of the LES (see also [20]). This allows us a more precise comparison of the LES and the synthetically generated wind fields because all results are based on the same data set. Hence it is possible to verify the synthetic method as well as to point out differences between both methods. Three different meteorological scenarios (free-convective, convection- and shear-driven, stably stratified) were simulated to cover different kinds of atmospheric flow conditions within the ABL and to analyze how they affect the results. Although the turbulence which can be expected in case of a stable stratified boundary layer may only play a minor role for stall of aircraft, this meteorological scenario was also investigated to cover the full range of typical meteorological boundary layer conditions and their reproducibility with the synthetic method.

This paper is composed as follows: the next section introduces the LES method. The applied LES model and the setup of the selected meteorological scenarios are described. Section 3 specifies the generation technique of the synthetic method. Furthermore, the approach of the virtual flight measurements is explained and the statistics of the virtual time series data required for the generation of the synthetic fields are analyzed. Section 4 presents and discusses the results of the comparison for each meteorological scenario. In Section 5 the results are summarized.

2. LES method

The LES method explicitly simulates highly resolved three-dimensional realistic wind fields of the ABL. The resulting wind fields have to fulfill two conditions in order to be used as initial state for a CFD-model for investigations of stall effects. First, the LES fields require a resolution which is fine enough to resolve turbulent elements which have an influence on aircraft flight characteristics. That means, that the resolved turbulence elements must be at least one order of magnitude smaller than the typical wing span of commercial aircraft (30–80 m, resulting grid spacing $\leqslant$2 m). Second, the model domain has to be large enough to allow the development of the most important range of turbulence scales which usually occur in a realistic ABL (domain size of about 2 km^3 or larger). Both requirements result in a extremely large number of gridpoints ($\geqslant 10^9$). After introducing the applied LES model, the three meteorological scenarios, their setups and their boundary conditions are explained in detail. The approach of the virtual flight measurements carried out within the LES is presented in Section 3.

2.1. PALM – a parallelized LES model

The study presented in this paper uses the **pa**rallelized **L**ES **m**odel PALM developed by Raasch and Schröter [8]. It is a model for the atmospheric or oceanic boundary layer and was applied in former studies of e.g.: thermally induced oscillations in the CBL [9]; roll convection during a cold air outbreak [10]; or the urban canopy layer from street canyon to neighborhood scale [11]. PALM is written in Fortran 95 with single processor optimization for different processor architectures and uses MPI and/or OpenMP for parallelization.

It calculates the non-hydrostatic, incompressible Navier–Stokes equations in Boussinesq form, the 1st law of thermodynamics, and equations for subgrid-scale (SGS) turbulent kinetic energy (TKE) and scalar conservation. The equations are discretized using finite differences, and are filtered implicitly following the volume-balance approach [12]. Turbulence closure uses the 1.5th order Deardorff [13] scheme. Variables are staggered according to the marker-and-cell method/Arakawa C grid [14,15]. Advection scheme is the second-order Piacsek-Williams scheme [16] and time integration uses the 3rd-order Runge–Kutta scheme. Incompressibility is ensured by the fractional-step method, and the resulting Poisson equation for the perturbation pressure is solved by using FFT.

The lateral boundary conditions are cyclic. At the lower boundary no-slip conditions are used with the assumption of Monin–Obukhov similarity between the surface and the first computational grid level. A constant roughness length in all simulations is applied ($z_0 = 0.1$ m).

2.2. Setup of the three scenarios

Three meteorological scenarios were selected, which are each driven in three different ways, and have different influences on the stall of the aircraft. The first scenario is a buoyancy-driven convective boundary layer (CBL). The free convection is caused by a homogeneously heated surface. No mean background wind is present. This first scenario represents a typical meteorological condition of a mid-latitude high pressure situation over a homogeneous surface. The strongest turbulent elements in this CBL lead to vertical velocities up to $w = 8$ m s^{-1}. The second scenario is an extension of the first. In addition to buoyancy, it is driven by wind shear caused by a moderate geostrophic wind of $u_g = 5$ m s^{-1} (westerly) at the top of the boundary layer. The third scenario is a shear-driven stably stratified boundary layer (SBL). It is also known as nocturnal boundary layer (NBL). Although only weak turbulence occurs in this scenario due to the damping characteristics of the stable stratification, we chose it for an extensive comparison of the two turbulence generation methods at different meteorological conditions. All three scenarios were simulated over a period of 6 h to determine the statistical properties accurately. After 1 h, each flow reached a quasi-stationary state which meant that averaged turbulent quantities of the flow did not change much in time and the boundary layer growth rates of the CBLs were small. Data extracted during this state, were used for virtual measurements and statistical analysis.

For the first and the second scenarios, model domain sizes of $4 \times 4 \times 1.7$ km^3 and a grid resolution of 2 m were used. The vertical grid was stretched from 800 m up to the top of the domain to save computational time. This resulted in a total number of $2049 \times 2049 \times 450 = 1.89 \times 10^9$ grid points. In the CBL cases a homogeneous heating (kinematic sensible heatflux = 0.24 K m s^{-1} which corresponds to a surface sensible heat flux density of 285 W m^{-2}) was used. An initial temperature profile was defined at the beginning of the simulation with neutral conditions up to a level of 700 m, followed by a stable layer with a constant gradient of 2 K/100 m up to the total model domain height to allow for a rapid development of convection. During the simulation, the boundary layer height z_i increased slowly (around 80 m/h in both CBL cases).

As third scenario, an SBL was simulated using the GABLS3 LES intercomparison setup [17]. The GABLS3 case is based on the moderately stratified, baroclinic, mid-latitude boundary layer that was observed over Cabauw (the Netherlands) on July 1st, 2006. The model domain had a size of $800 \times 800 \times 800$ m^3 and a grid spacing of 1 m, which results in $800^3 = 0.5 \times 10^9$ grid points. The smaller domain and higher resolution is due to the smaller-scaled turbulence compared to the convective cases. Initial profiles of potential temperature, humidity and velocity were given at the beginning. A geostrophic wind ($u_g = -2.0$ m s^{-1}, $v_g = 2.0$ m s^{-1}) and large-scale advection of potential temperature, humidity and velocity drove the flow. After each time step, these driving forces as well as the potential temperature and humidity at the bottom were adjusted.

Table 1 shows the characteristic boundary layer scales u_* (friction velocity), $w_* = [g/\theta(\overline{w'\theta'_0})z_i]^{1/3}$ (convective velocity scale), $\theta_* = -\overline{w'\theta'_0}/u_*$ (temperature scale), and z_i (boundary layer height). The subscript zero indicates the surface layer value of the heat flux, θ is the potential temperature, and g is the acceleration due to gravity. The values listed in Table 1 are averaged both in space (horizontally) and time. They agree well with those of other studies about the CBL (e.g. [24]) and the SBL (e.g. [26]).

3. Synthetic method

The synthetic method uses statistical quantities derived from one-dimensional time series of the wind components to generate synthetic three-dimensional wind fields. Usually, highly resolved ($\Delta \approx 0.4$ m) time series are obtained from real flight measurements which were carried out within the ABL using the airborne measurement system Helipod [7,18,19]. The energy spectrum, the correlation tensor and the variances of the wind components were taken from the measured time series to generate the synthetic fields. A huge database of different meteorological scenarios already exists and the technique of generation is comparatively fast.

As mentioned above, we replaced the real flight measurements by virtual flight measurements. The method was developed and implemented by Schröter et al. [20] and is described more in detail in the next subsection. The virtual flights were performed within the simulated wind fields of the LES that imitated the real measurements. The resulting virtual time series were then used to generate synthetic wind fields. Subsequently, the synthetic wind fields were compared with the directly simulated LES wind fields.

Table 1
Summary of steady-state values of characteristic boundary layer scales. “CBL 1” denotes the CBL case without mean background wind, “CBL 2” the CBL case with a moderate mean background wind, and “SBL” the stably stratified boundary layer.

Case	u_* (m s^{-1})	w_* (m s^{-1})	θ_* (K)	z_i (m)
CBL 1	0.21	2.05	−1.32	980
CBL 2	0.30	1.34	−0.39	960
SBL	0.18	–	0.06	150

Due to the LES grid spacing of 2 m, the virtual time series and the corresponding synthetic wind fields have lower resolution than that of the real flight measurements. The resolution in the virtual flight series is 10 m for the CBL cases and 5 m in the SBL case (see next section for further explanation). When choosing the grid spacing for the three-dimensional synthetic wind field, one has to keep in mind that the Nyquist wavenumber for the one-dimensional flight measurements is larger than for a three-dimensional field with the same grid spacing [7]. Following Auerswald et al. [7] the grid spacing of the three-dimensional grid needed to resolve the Nyquist wavenumber of the one-dimensional flight measurements needs to be chosen as:

$$\Delta x = \sqrt{3}\Delta x_m. \tag{1}$$

Here, Δx is the grid spacing of the three-dimensional grid of the synthetic field and Δx_m represents the grid spacing of the flight measurements. In case of the virtually measured time series of both CBLs, this results in grid spacings of 17.32 m for the three-dimensional synthetic field, since the virtual time series have a resolution of 10 m. The synthetic wind field obtained from the virtual time series of the SBL (resolution of 5 m) has a grid spacing of 8.66 m. For the generation of the synthetic fields 500 grid points along each direction were chosen to get significant statistics. An overview of the model domain characteristics of the two different methods is given in Table 2.

The generation technique is described in detail by Auerswald et al. [7]. The method is based on the Fourier approach which was used in earlier works to generate a synthetic turbulent wind field (e.g. [21,22] or [23]). It combines Fourier modes with different wavenumbers and amplitudes to build a synthetic turbulent field. The energy spectrum is imposed by choosing the amplitudes of the Fourier modes accordingly. Additionally, the direction of the wavenumber vectors are chosen randomly. By forcing the amplitude vectors to be perpendicular to the wavenumber vectors, it is ensured that the resulting field is free of divergence. This is an advantage, especially if the synthetic turbulence is intended to be used in a compressible flow model. The turbulence resulting from the described method is isotropic. By applying the Cholesky method (e.g. in [4]) however, the field can be modified to have predefined one-point correlations which introduces anisotropy to the synthetic turbulence. Furthermore, the turbulence field can be scaled to contain predefined variances.

Since the synthetic wind field uses only measured data from one altitude, it contains no information about the vertical structure of the turbulent field. Therefore, it does not have the typical vertical structure of a boundary layer, for example small-scaled eddies in the lower part and larger eddies in the upper part. In fact, the synthetic wind field represents, over its entire height, that part of the boundary layer where the flight measurements were performed.

3.1. Virtual flight measurements within the LES

The virtual flight measurements were carried out within the LES of each meteorological scenario at ten different height levels simultaneously, following the method of Schröter et al. [20]. After

Table 2
Comparison of the model domain characteristics of the two methods used for this study.

	LES (CBL)	Synthetic method
Domain size	$4000 \times 4000 \times 1700$ m^3	$8660 \times 8660 \times 8660$ m^3
Grid spacing	2 m	17.3 m
Grid points	1.89×10^9	0.125×10^9

each time step, measurement data were taken along a defined horizontal path through the model domain. Due to cyclic boundary conditions, the path was rotated by 30° to the *x*-axis. This avoids passing the same structures after some time when the path 'leaves' the model domain and enters it on the opposite side. Measurements along ten different paths in one horizontal plane were performed to analyze the statistical precision of the virtual time series data. Starting heights for the virtual flights ranged from 50 m to 500 m within both CBLs. The ratio of flight level height to boundary layer height z_i was kept constant throughout the simulations of the CBLs to minimize the effects caused by changes in z_i. Since the height of the SBL is lower than for the two convective cases, starting heights for the virtual flights ranged from just 50 m to 300 m within the SBL. Here, the flight altitudes were kept constant because the boundary layer height growth is much slower than for the CBLs. The virtual flights started after 1 h of simulation time, when the turbulent flow had reached the quasi-stationary state. The three wind components u, v, w and the potential temperature θ were virtually measured after each time step. As mentioned above, the resolution of the virtual measurements or more precisely the flight distance between each time step is 10 m in the CBL cases and 5 m in the SBL. It is defined as the product of the ground speed of the virtual aircraft and the model time step. We chose 62.5 m s^{-1} as the ground speed and 0.16 s (CBL cases) and 0.08 s (SBL case) as the constant model time step. This choice ensures that the ground speed is in the order of measured flight speeds. On the other hand the chosen model time step is still large enough to avoid an increase in the duration (and hence costs) of the simulation, which would be the case for an artificial decrease of the time step. The higher resolution of the virtual flight measurements in the SBL case correlates with the halving of the model grid spacing (1 m instead of 2 m in the CBL cases). As described in the next parts of this section, the resulting resolutions of the virtual flights are sufficient to provide data which represent the turbulence of the simulated boundary layer adequately.

For each scenario, an analysis was carried out to obtain the statistical precision of the virtually measured data at each height level. Besides the energy spectrum, the correlation coefficients and variances of the wind components are used to generate the synthetic wind fields. The correlation coefficients of the virtual time series are defined as the (time-averaged) covariances of two wind components normalized by their standard deviations σ:

$$\mathrm{cor}(u,v)=\frac{\overline{u'\cdot v'}}{\sigma_u\cdot\sigma_v},\ \mathrm{cor}(u,w)=\frac{\overline{u'\cdot w'}}{\sigma_u\cdot\sigma_w},\ \mathrm{cor}(v,w)=\frac{\overline{v'\cdot w'}}{\sigma_v\cdot\sigma_w}, \qquad (2)$$

where u' and v' are deviations of the turbulent velocities from the time averaged mean wind of the corresponding wind component. The standard deviations are the square root of the (time-averaged) variances of the time series:

$$\sigma_u^2=\overline{u'^2},\ \sigma_v^2=\overline{v'^2},\ \sigma_w^2=\overline{w'^2}. \qquad (3)$$

To estimate the duration over which the variable must be measured virtually in order to obtain a sufficient accuracy in the statistics, the

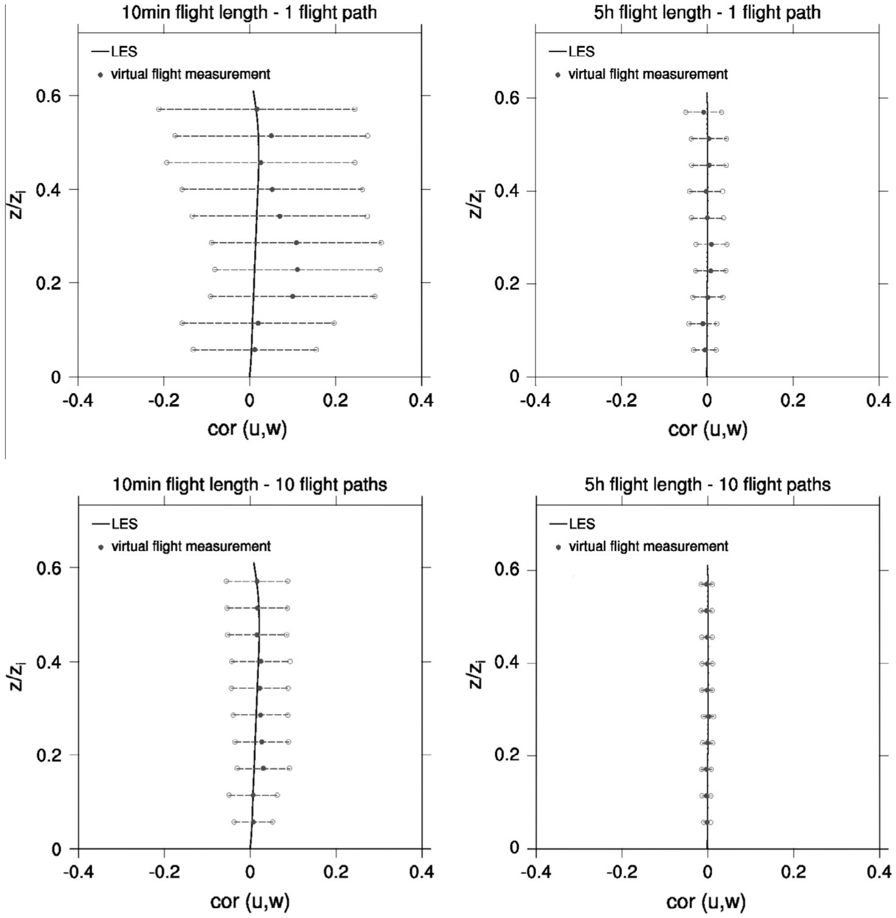

Fig. 1. CBL without mean background wind: correlation coefficients of the velocity components u and w are plotted against the normalized height. Virtual time series coefficients (black dots with error bars) are compared with the horizontally and time averaged coefficients of the LES wind field (continuous line). Different averaging times and numbers of virtual flight paths were used for the calculation of the coefficients.

averaging time was varied between 10 min and 5 h. Additionally, the number of simultaneous flights at each height was varied between one and ten. Fig. 1 shows the correlation coefficients (Eq. (2)) of the CBL in the case without mean background wind. Different combinations of the number of virtual flight paths at each flight level and averaging times are presented in the four graphs. Estimations of errors were determined following the method of Lenschow et al. [24,25]. The results from the virtual flight measurements were compared with the horizontally and time averaged correlation coefficients of the LES wind field for the same time period. Due to the absence of a mean wind, ideally the values should converge to zero at all heights. This is best achieved with 5 h averaging time and ten flight paths for both methods. In case of a reduction of the averaging time and/or the number of flight paths (Fig. 1), the uncertainty in statistical values deteriorates significantly. This means that virtually measured quantities agree less with quantities of the LES wind field, and the systematic and random errors become larger. In principle, Fig. 1 shows that the longer the averaging time and the more flight paths were used, the higher is the statistical significance (in agreement with [24,25]); virtually measured quantities agree better with quantities of the LES wind field and the systematic and random errors become smaller.

Analysis as shown exemplary in Fig. 1 for the CBL without mean background wind were conducted for all three scenarios. Besides the correlation coefficients, covariances and variances of the three wind components and scalars were also calculated. The following conclusions can be drawn from this analysis: For both convective cases, covariances of the wind components require a much longer averaging time (and therefore flight length) than variances or covariances of scalars to achieve a certain accuracy (in agreement with [24]). In contrast to the first scenario, the CBL with mean background wind shows higher correlations between two different wind components. In a CBL, the correlation coefficients depend on the ratio of the Monin–Obukhov length to the height of the ABL [25]. In case of a mean background wind, the Monin–Obukhov length is about one order of magnitude larger than in the CBL without mean background wind. This results in covariances and correlation coefficients that converge slightly faster to the horizontally averaged quantities of the LES wind field. In case of the SBL, correlation coefficients of the wind components are nearly one order of magnitude larger than for the convective cases within the ABL. This results in better statistics for the same flight duration which can be seen in Fig. 2. Differences between the correlation coefficients calculated from the virtual flight measurements and the LES mean value are very low for 10 min averaging time and ten flight paths. The shapes of the profiles of the correlation coefficients with a decrease up to the top of the boundary layer ($z_i \approx 150$ m) are typical for a stably stratified boundary layer and correspond well with those shown in [3].

The LES results show that several long term time series are necessary to obtain sufficiently small errors from flight measurement data. In a real flight experiment, neither the discussed duration due to the instationarity of the real flow conditions nor the number of simultaneous flights, since real flight measurements generally provide data of one single flight leg, are realizable. To be closer to experimental reality, we decided to use one virtually measured time series of 2 h for the generation of the synthetic fields in both CBL cases. Fig. 3 shows the statistics of the correlation coefficients for both CBL cases for the chosen combination of number and duration of flights. In both cases the characteristics of the horizontally averaged quantities of the LES are well reproduced by the virtual flight measurements. The data provided for the synthetic generation of the flow field were taken from the virtual flight with a starting height of 400 m, which is approximately half of the inversion height (0.46 z_i). This height was chosen because it is located in the mixed layer and can therefore be considered as representative for the major part of the boundary layer.

Since the virtual measurements of the SBL converge faster to the LES ensemble mean values, the 1 h duration of the flight was considered as sufficient for the SBL case (see again Fig. 2). The lower inversion height compared to the CBL cases leads to a lower starting height of 125 m.

The energy spectrum, the correlation coefficients and the variances of the wind components were taken from the three virtually measured time series to generate the synthetic fields. These are compared with the directly simulated LES fields in the next section.

4. Comparison of LES and synthetic field

For each of the three meteorological scenarios, instantaneous cross sections of LES and synthetic wind fields were analyzed. Additionally, horizontally averaged turbulence parameters of the LES field as well as their statistical distribution were compared with the same quantities obtained from the synthetic fields. Furthermore, the probability density function of the angles of attack, which would occur if the wind vectors of the LES and the synthetic

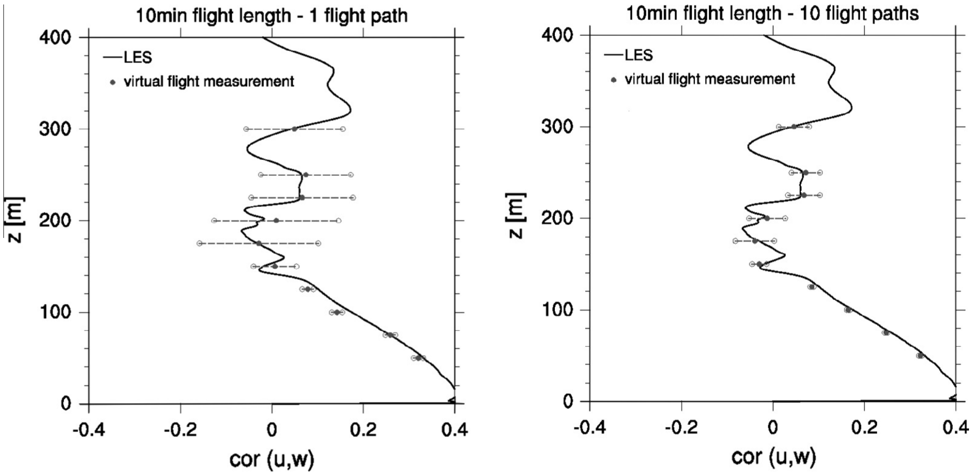

Fig. 2. SBL case: correlation coefficients of the velocity components u and w plotted against height (not normalized due to the low boundary layer growth rate of the SBL). Virtual time series coefficients (black dots with error bars) are compared with the horizontally and time averaged coefficients of the LES wind field (continuous line). Different numbers of virtual flight paths and an averaging time of 10 min were used for the calculation of the coefficients.

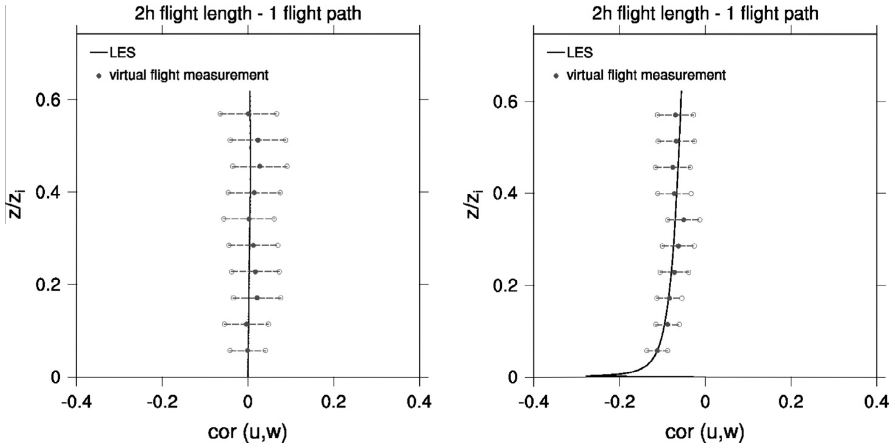

Fig. 3. CBL without mean wind (left) and with a mean background wind of 5 m s^{-1}(right): correlation coefficients of the velocity components u and w are plotted against the normalized height. Virtual time series coefficients (black dots with error bars) are compared with the horizontally and time averaged coefficients of the LES wind field (continuous line). One virtually measured time series of 2 h was used for the calculation of the coefficients.

field interact with a wing, were calculated. The results for each scenario are presented separately.

4.1. Purely buoyancy-driven boundary layer

In the homogeneously heated CBL without mean background wind turbulence is purely generated by buoyancy. Regions with strong updrafts and slightly weaker downdrafts develop (see e.g. [3,27]). Thermals that range from the surface to the top of the boundary layer reach positive vertical velocities up to 8 m s^{-1} whereas corresponding downdrafts have negative velocities of -4 to -5 m s^{-1}. An organized circulation pattern occurs in the lower boundary layer (up to 200 m, not shown here), where up- and downdrafts are arranged in hexagonal cells (a so-called spoke-like pattern [27]). Large regions with negative vertical velocities are surrounded by narrow updrafts. The strongest positive vertical velocities evolve in areas where spokes converge. Above this lower part of the boundary layer, the flow patterns change into larger-scale structures. The distribution of the vertical velocity changes to wider regions of up- and downdrafts, whereas the regions of updrafts still remain slightly smaller with stronger absolute wind velocities compared to the downdrafts. The vertical velocity is non-Gaussian-distributed in the bulk of the mixing layer, which is typical for a CBL (see e.g. [3,28]).

The LES cross section of Fig. 4 (left) shows this non-Gaussian distribution of the vertical velocity w at a height of 0.46 z_i (equal to the height of the virtual flight measurement). The synthetic field did not reproduce these organized (coherent) structures as can be seen in the synthetic cross section of Fig. 4 (right). As mentioned in Section 3, the synthetic method can not reproduce the height dependencies of the atmospheric quantities. Therefore each height level in the synthetic wind field is representative for the flow of the same flight level. As a consequence, the cross section taken arbitrarily from the middle of the model domain (grid point number in the vertical direction $n_k = 250$). Instead of coherent structures, which occur in the LES field, uniformly distributed vertical velocities with up- and downdrafts of the same amplitude are generated.

A comparison of the turbulence parameters obtained from the LES and the synthetic wind fields shows more consistent results of the two methods. The parameters that were used as input parameters for the generation of the synthetic field are analyzed. These are variances and correlation coefficients of all velocity components. Beside the values of the flow fields of the two methods (LES and synthetic generation), the parameter values obtained from the virtual flight measurements are listed. The values were calculated in the horizontal planes shown in Fig. 4. Variances and correlation coefficients agree well, which means that the synthetic

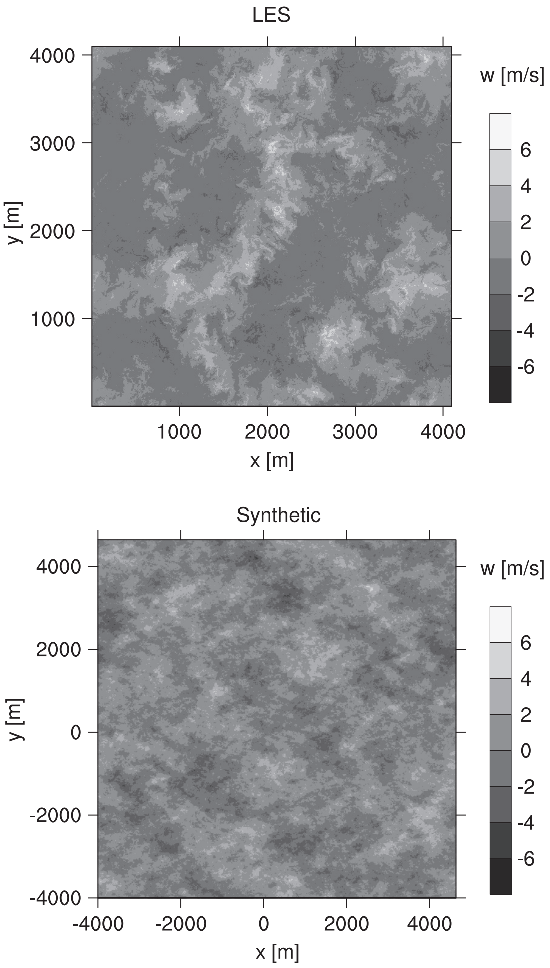

Fig. 4. CBL without mean background wind: horizontal cross sections of the vertical velocity w at height 0.46 z_i of the LES domain and in the middle of the synthetic model domain. The differences in the axis scaling can be explained by the different model domains of the two methods.

method produces three-dimensional turbulent wind fields whose values of the statistical input parameters are in good agreement with the values of the same parameters of the horizontal plane within the LES field.

The good agreement of the statistics listed in Table 3 is in contrast to the differences concerning the distribution of the vertical velocity w in the horizontal cross sections shown in Fig. 4. To quantify the differences between the distributions of the vertical velocity, the probability density function (PDF) of w was calculated. Therefore the data of the horizontal cross section of the LES field according to the virtual flight measurement height were used. A comparison of the PDF from the LES cross section with the corresponding PDF from the virtual time series and the PDF from the synthetic field can be seen in Fig. 5. In the latter, data from the total domain of the synthetic field were used to increase significance. As mentioned above, the LES field reproduces the typical non-Gaussian distributed vertical velocities of a homogeneously heated CBL. This leads to a PDF with a negatively skewed shape. The PDF of the virtually measured time series shows the same feature. Only the peak value is slightly larger compared to the value of the LES horizontal plane, which can be explained by the smaller database of the virtual flight statistics. In contrast, the PDF from the synthetic field does not show this asymmetric course. Instead, it follows a Gaussian distribution. This result confirms the impression from the horizontal cross section of w in Fig. 4, that the synthetic wind field does not contain the typical organized structures of a CBL. Furthermore it shows that although the virtual flight measurements capture the distribution of w, the synthetic field does not reproduce it, even though it is based on the virtual-flight data. The reason for this is that the turbulence generator uses the energy spectrum, variances and covariances of the whole time series [7]. Therefore, no spatial information from the time series is used to generate the synthetic field. Rather the synthetic field is constructed in Fourier space and the direction of the Fourier coefficients is equally distributed over a unit sphere.

Table 3
CBL without mean background wind: variances and correlation coefficients of the velocity components are given for the LES field (spatial average), the virtual time series (time average) and the synthetic field (spatial average).

	LES horizontal plane	LES virtual measurement	Synthetic field
σ_u^2 ($\mathrm{m^2\,s^{-2}}$)	0.72	0.73	0.74
σ_v^2 ($\mathrm{m^2\,s^{-2}}$)	0.70	0.73	0.70
σ_w^2 ($\mathrm{m^2\,s^{-2}}$)	1.61	1.67	1.68
$\mathrm{cor}(u,w)$	0.01	−0.001	0.01
$\mathrm{cor}(v,w)$	0.01	0.03	0.01
$\mathrm{cor}(u,v)$	−0.01	−0.03	−0.002

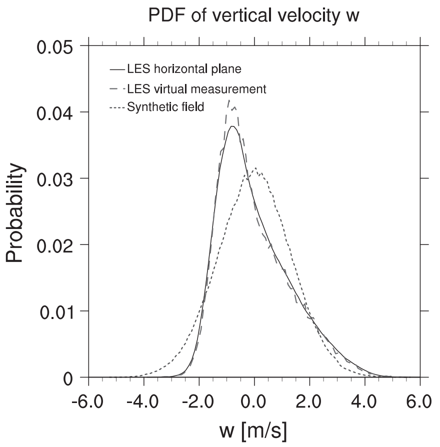

Fig. 5. CBL without mean background wind: probability density function of the vertical velocity w at height 0.46 z_i for the LES field, the virtual measurement and the synthetic field.

Synthetic wind fields with Gaussian distributed vertical velocities that are used to initialize a numerical CFD-model for investigations of stall effects may influence the wing in a different way than non-Gaussian distributed wind field would do. In order to make a first estimation of the influence to an aircraft caused by the differences pointed out above, we determined the angle of attack α of a wing for the two different wind fields (LES and synthetic). It is defined as

$$\alpha = \arctan\left(\frac{w}{v_h}\right), \tag{4}$$

where w is the vertical velocity and v_h the horizontal flow velocity relative to a virtual aircraft flying in the x-direction. The horizontal velocity v_h consists of the flying speed and the wind velocity of the u-component. For the LES field, α was calculated at each gridpoint in the horizontal plane shown in Fig. 4. For the synthetic field, it was calculated at each gridpoint in the model domain. Fig. 6 shows PDFs of the angles that occur in both fields. The differences in the two curves reflect the differences in the PDFs of w (Fig. 5). The values of the angle along the flight path of an aircraft are important for the investigations of stall effects since they are an indicator for flow separation. Especially, in high lift conditions when the angle of attack is already close to the stall angle of attack, the synthetic wind fields may lead to fatally wrong results. Simulations containing a wing would be necessary to investigate the consequences of the differences in the velocity fields in detail.

4.2. Buoyancy-and shear-driven boundary layer

In the homogeneously heated CBL with a moderate mean background wind, turbulence is generated by convection and additionally by vertical shear from the background wind. Coherent structures that occur in the free convective case develop as well but they are modified by the shear (see e.g. [29,30,3]). Since the differences in the flow patterns and statistical turbulence characteristics between this second CBL case and the first CBL case are very small, only a short description and overview of the results of the second case is given.

The modification of the flow structures by the mean wind has the following effects: Compared to the first CBL case, the regions

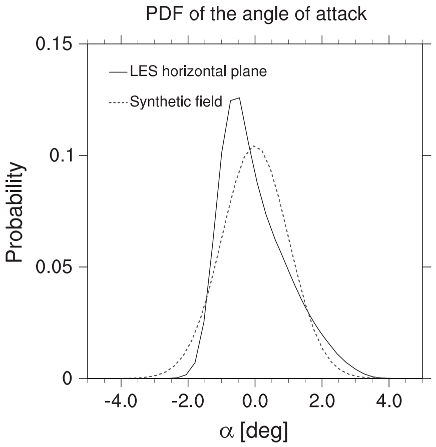

Fig. 6. CBL without mean background wind: probability density function of the angle of attack α at height 0.46 z_i for the LES field and the synthetic field.

of the up- and downdrafts are slightly larger. However, in the LES, the typical distribution of vertical velocities with larger regions of weaker downdrafts and smaller regions of stronger updrafts still appears. The synthetic wind field reproduces the enlargement of the regions of up -and downdrafts compared to the first CBL case, but the distribution of the vertical velocity can not be generated (see again Fig. 5).

The PDFs of the vertical velocity are different between LES field, virtual time series and synthetic field. The non-Gaussian distribution that occurs in the horizontal plane of the LES field can also be found in the virtual time series but is not generated by the synthetic field.

As expected, the PDFs of the angle of attack correlate with this distribution of *w*. A comparison of variances and correlation coefficients of the velocity components, which is comparable to the comparison presented in Table 3, shows qualitatively the same results. Although both variances and correlation coefficients are slightly larger compared to the first free-convection case, the values of the virtual measurements and the LES field are well reproduced by the synthetic fields.

There were two main reasons for the selection of the two CBL cases. First, a high impact on a wing of an aircraft is expected from the strong turbulence in the CBL. Second, they represent typical meteorological scenarios during the day in which flight measurements with the Helipod measurement system are performed (beside the stably stratified boundary layer analyzed below). Thus, Helipod data obtained from comparable atmospheric conditions are used to generate synthetic flow fields and, furthermore, as input flow fields in CFD simulations. The comparisons of both CBLs presented here show qualitatively the same differences between the LES and the synthetic flow fields. The differences are a consequence of the missing coherent structures in the synthetic flow fields. Further investigations on the synthetic generation method seem to be necessary. Beside the quantification of the influence of the differences in the angle of attack compared to the LES method, an improvement of the synthetic method in order to reproduce coherent structures would be useful.

4.3. Stably stratified boundary layer

In the third scenario, turbulence is generated only by vertical shear from the mean background wind. Compared to the two CBL cases the turbulence is considerably weaker because the stability of the boundary layer leads to negative buoyancy of vertically deflected air parcels and hence to smaller eddy motions in the boundary layer. A further characteristic of the SBL caused by the stability and the resulting weaker turbulence is a lower vertical extension of the boundary layer. The upper limit of the SBL presented here is thus lower than in the other scenarios and varies around $z_i \approx 150$ m. Vertical velocities are generally one order of magnitude smaller than in the convective cases. The cross section of the LES field in Fig. 7 shows the vertical velocity *w* at the height of the virtual flight measurements ($z = 125$ m). The distribution of vertical velocities differs significant from the CBL cases, since no coherent structures are visible. Small-scale flow patterns caused by the smaller turbulent eddies have an isotropic distribution in the horizontal cross sections. In contrast to the results of both CBLs, the cross section of the synthetic field (Fig. 7), taken arbitrarily in the middle of the model domain (grid point number in the vertical direction $n_k = 250$), is in much better visual agreement with the LES field. Hence, the synthetic method seems to be able to generate wind fields that are similar to LES fields in case of a stable stratified boundary layer.

The comparison of variances and correlation coefficients of the velocity components is presented in Table 4. As in the other cases, they are in good agreement. The smaller variances (three orders of magnitude compared to the CBL cases) represent the weaker turbulence. In contrast $\mathrm{cor}(v, w)$ and $\mathrm{cor}(u, v)$ have values which are two orders of magnitude larger than those of the CBL cases.

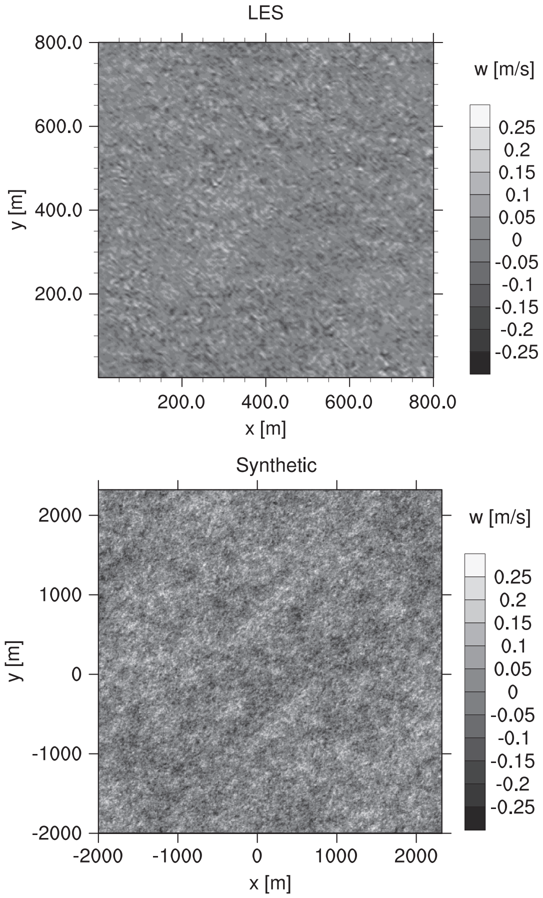

Fig. 7. SBL: horizontal cross sections of the vertical velocity *w* at height 125 m for the LES field and in the middle of the synthetic field.

Table 4
SBL: variances and correlation coefficients of the velocity components are given for the LES field (spatial average), the virtual time series (time average) and the synthetic field (spatial average).

	LES horizontal plane	LES virtual measurement	Synthetic field
σ_u^2 ($\mathrm{m^2\,s^{-2}}$)	0.006	0.006	0.006
σ_v^2 ($\mathrm{m^2\,s^{-2}}$)	0.01	0.01	0.01
σ_w^2 ($\mathrm{m^2\,s^{-2}}$)	0.002	0.002	0.002
$\mathrm{cor}(u, w)$	0.04	0.02	0.04
$\mathrm{cor}(v, w)$	−0.24	−0.24	−0.24
$\mathrm{cor}(u, v)$	−0.14	−0.16	−0.16

The PDFs of the vertical velocity *w* are shown in Fig. 8. The functions of both wind fields and the virtual time series are displayed. All three distributions follow a near-Gaussian distribution. The PDF of the angle of attack is shown in Fig. 9. Both distributions have qualitatively the same shape and reflect the curves of the distribution of the vertical velocity, but for the synthetic wind field the distribution is more narrow and reaches a much higher maximum (25% instead of 15% in the LES).

Considering the relatively small values of the angles of attack and the fact that they would not affect a wing much, the differences may not have a significant influence on an aircraft. However,

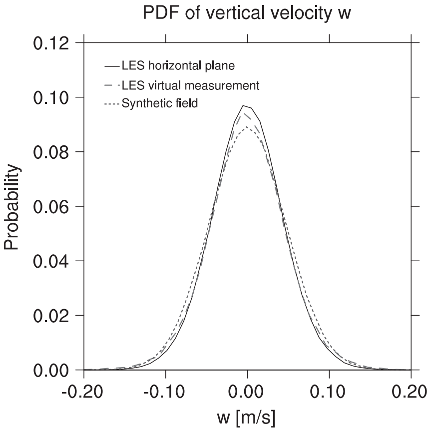

Fig. 8. SBL: probability density function of the vertical velocity *w* at height 125 m for the LES field and of the total domain for the synthetic field.

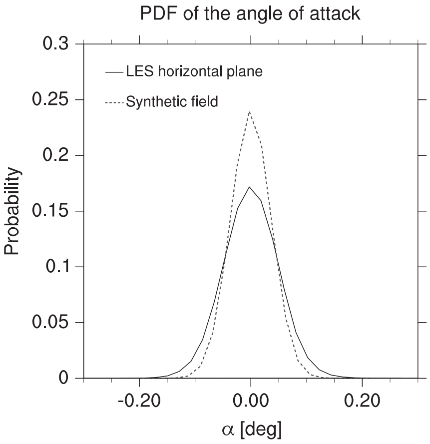

Fig. 9. SBL: probability density function of the angle of attack α at height 125 m for the LES field and of the total domain for the synthetic field.

as already mentioned above for the two CBL cases, further investigations with a CFD model containing a wing initialized with flow fields generated with the two methods described, would be helpful to quantify the differences.

5. Conclusions

Two different methods to provide three-dimensional realistic turbulent wind fields of the ABL and subsequently, to initialize a CFD-model for investigations of stall effects were compared. The first method uses LES and explicitly simulates highly resolved turbulent flows under realistic conditions. The second method generates synthetic fields by means of statistical quantities derived from one-dimensional flight measurements. The main object of this study was to compare the obtained wind fields of both methods and to identify their differences.

For the comparison, one-dimensional virtual flight measurements were performed within the LES of three different meteorological scenarios (two homogeneously heated CBLs with and without mean background wind as well as an SBL). Afterwards, synthetic fields were generated from these virtual time series and compared with the explicitly simulated LES fields. This approach allows for a very precise evaluation of the quality of the synthetic fields, because ideally, the synthetic fields should show the same features as the explicitly simulated LES fields.

The synthetic fields can reproduce the averaged turbulence parameters that were used as input parameters for the generation: variances and correlation coefficients of the velocity components agree well with the parameters of the LES field that were calculated for a horizontal plane at the height level corresponding to the virtual flight measurement height. Since the virtual time series do not provide height information, typical three-dimensional coherent structures as developed in the LES fields of the convective cases cannot be generated. Therefore, the non-Gaussian distribution of the vertical velocity which occurs in the LES fields of the CBLs is missing although this distribution appears in the virtual time series. The comparison of the angles of attack show similar differences between synthetic and LES field. The distributions of the angles are correlated to the distributions of the vertical velocity. It needs to be studied in detail whether future applications of the synthetic method require a better representation of the non-Gaussian turbulence statistics caused by coherent flow structures. In the stably stratified case, in contrast to the results for the CBLs, the synthetic method produces wind fields that are similar to the LES fields. Here, the meteorological conditions lead to Gaussian-distributed small-scale turbulence, which can be well reproduced by the synthetic method.

As mentioned in the introduction, alternative methods to generate synthetic turbulence exists which are often based on the Dryden or von Kàrmàn spectrum. We did not investigate whether these alternative methods perform better than the synthetic method used in this study. Since the turbulence generator we used is initialized with real measurement data, we assume that it provides more accurate results. However, further investigation would be necessary to prove this hypothesis.

The results are highly relevant for future studies employing one of these methods. The actual influence of the differences between the two methods on the stall of aircraft can be investigated by using both wind fields as initialization data of a CFD model. The generation of synthetic fields is faster and cheaper than the LES method, but so far, in a convectively driven atmosphere they do not represent all characteristics of the atmospheric turbulence. The differences in the CBLs concerning the distribution of the vertical velocity and consequently the angle of attack as well as missing coherent structures in one horizontal plane may have a significant effect on the stall of aircraft. Thus it seems to be reasonable to expand the synthetic method with the ability to reproduce coherent structures, for instance. However, the current synthetic method is well qualified to reproduce wind fields with nearly Gaussian-distributed turbulence.

Acknowledgments

This work has been carried out within the research group FOR 1066 (http://www.for1066.tu-bs.de/) and was founded by the German Research Foundation (DFG) Grants BA 1988/8-2 and RA 617/19-2. All numerical simulations have been carried out on the SGI-ICE system of the North-German Supercomputing Alliance (HLRN).

References

[1] Schlichting H, Gersten K. Boundary-layer theory. Springer; 2000. p. 799.
[2] Anderson JD. Fundamentals of aerodynamics. McGraw-Hill; 2010. p. 1152.
[3] Stull RB. An introduction to boundary layer meteorology. Kluver Academic Publishers; 1988. p. 666.
[4] Lund TS, Wu X, Squires KD. Generation of turbulent inflow data for spatially-developing boundary layer simulations. J Comput Phys 1998;140:233–58.
[5] Fidkowski K, Engelsen F, Willcox K, Kroo I. Stochastic gust analysis techniques for aircraft conceptual design. In: AIAA-2008-5848, 12th AIAA/ISSMO

multidisciplinary analysis and optimization conference, Victoria, British Columbia, September 10–12; 2008.
[6] Yang X, Pota H, Garratt M. Design of a gust-attenuation controller for landing operations of unmanned autonomous helicopters. In: Proceedings of the IEEE multi-conference on systems and control, IEEE presented at IEEE multi-conference on systems and control, Yokohama, Japan, Saint Petersburg, Russia, 8–10 July; 2009.
[7] Auerswald T, Bange J, Knopp T, Weinman K, Radespiel R. Large-eddy simulations of realistic atmospheric turbulence with the DLR-TAU-code initialized by in-situ airbone measurements. Comput Fluids 2012;66:121–9.
[8] Raasch S, Schröter M. PALM – a large-eddy simulation model performing on massively parallel computers. Meteorologische Zeitschrift 2001;10(5):363–72.
[9] Letzel MO, Raasch S. Large-eddy simulation of thermally induced oscillations in the convective boundary layer. J Atmos Sci 2003;60:2328–41.
[10] Gryschka M, Raasch S. Roll convection during a cold air outbreak: a large-eddy simulation with stationary model domain. Geophys Res Lett 2005;32:L14805.
[11] Letzel MO, Krane M, Raasch S. High resolution urban large-eddy simulation studies from street canyon to neighbourhood scale. Atmos Environ 2008;42:8770–84.
[12] Schumann U. Subgrid scale model for finite difference simulations of turbulent flows in plane channels and annuli. J Comput Phys 1975;18:376–404.
[13] Deardorff JW. Stratocumulus-capped mixed layers derived from a three-dimensional model. Boundary-Layer Meteorol 1980;18:495–527.
[14] Harlow FH, Welch JE. Numerical calculation of time-dependent viscous incompressible flow with free surface. Phys Fluids 1965;8:2182–9.
[15] Arakawa A, Lamb VR. Computational design of the basic dynamical processes of the UCLA general circulation model. In: Chang J, editor. General circulation models of the atmosphere. Methods in computational physics, vol. 17. Academic Press; 1977. p. 173–265.
[16] Piacsek SA, Williams GP. Conservation properties of convection difference schemes. J Comput Phys 1970;6:392–405.
[17] http://www4.ncsu.edu/~sbasu5/GABLS3.
[18] Bange J, Spieß T, Herold M, Beyrich F, Hennemuth B. Turbulent fluxes from helipod flights above quasi-homogeneous patches within the LITFASS area. Boundary-Layer Meteorol 2006;121:127–51.
[19] Bange J, Spieß T, van den Kroonenberg A. Characteristics of the early-morning shallow convective boundary layer from Helipod flights during STINHO-2. Theor Appl Climatol 2007;90:113–26.
[20] Schröter M, Bange J, Raasch S. Simulated airborne flux measurements in a LES generated convective boundary layer. Boundary-Layer Metrol 2000;95:437–56.
[21] Krainchnan RH. Diffusion by a random velocity field. Phys Fluids 1970;13:22–31.
[22] Fung JCH, Vassilicos JC. Two-particle dispersion in turbulent like flows. Phys Rev E 1998;57:1677–90.
[23] Smirnov A, Shi S, Celik I. Random flow generation technique for large eddy simulations and particle-dynamics modeling. J Fluids Eng 2001;123:359–71.
[24] Lenschow D, Stankov B. Length scales in the convective boundary layer. J Atmos Sci 1986;43:1198–209.
[25] Lenschow D, Mann J, Kristensen L. How long is long enough when measuring fluxes and other turbulent statistics. J Atmos Ocean Technol 1994;11:661–73.
[26] Andren A. The structure of stably stratified atmospheric boundary layers: a large-eddy simulation study. QJR Meteorol Soc 1995;121:961–85.
[27] Schmidt H, Schumann U. Coherent structure of the convective boundary layer derived from large-eddy simulations. J Fluid Mech 1988;200:511–62.
[28] Deardorff JW, Willis GE. Further results from a laboratory model of the convective planetary boundary layer. Boundary-Layer Meteorol 1985;32:205–36.
[29] Kaimal JC, Businger JA. Case studies of a convective plume and a dust devil. J Appl Meteorol 1970;9:612–20.
[30] Wilczak JW, Tillman JE. The three-dimensional structure of convection in the atmospheric surface layer. J Atmos Sci 1980;37:2424–43.

A.3 Evolution of turbulence in a simulation of the atmospheric boundary layer flow around a wing using synthetic turbulence.

Evolution of turbulence in a simulation of the atmospheric boundary layer flow around a wing using synthetic turbulence

Torsten Auerswald and Jens Bange

Center for Applied Geoscience
University Tübingen, Germany

Abstract

A numerical simulation of the flow of atmospheric turbulence around a wing is presented. For representing the atmospheric turbulence in the simulation, synthetic turbulence is used which possesses turbulence statistics measured in the atmospheric boundary layer. The Chimera method is used to interpolate between a Cartesian grid, which contains the turbulent field, and an unstructured grid around the wing. For modeling turbulence Detached Eddy Simulation (DES) is used. Therefore, the turbulence in the simulation is modeled by Large-Eddy Simulation (LES) as well as Reynolds-Averaged Navier Stokes (RANS), depending on the location in the model domain. In the beginning of the simulation the turbulent field undergoes significant changes, especially in the cross-correlations, due to sound waves. In the energy spectrum a loss of energy can be seen in the small scales but for the largest part of the inertial subrange the shape of the spectrum remains constant. At the same time the total turbulent kinetic energy (TKE) decreases by approx. 60 %, since no source for turbulence is included in the model domain. The probability density functions (PDF) are relatively constant but become narrower due to the before mentioned decrease of TKE.

The PDFs of the velocity increments develop intermittency tails. Once the turbulence reaches the unstructured grid, stronger dissipation of small scales is observed while cross-correlations of the turbulent field remain relatively constant. No significant difference between the RANS and LES domain can be seen in the energy spectra. When the turbulence reaches the wing several up- and downdrafts cause increasing and decreasing lift and drag forces. The lift and drag forces are opositionally affected by the turbulence leading to decreasing drag with increasing lift and the other way around.

Keywords: Detached-Eddy Simulation, Atmospheric Boundary Layer, Turbulence-wing interaction, Synthetic Turbulence

Highlights

- A method for simulating turbulent flow around a wing has successfully been tested.
- It uses synthetic turbulence with statistics from the atmospheric boundary layer.
- Different grid types and turbulence model types are used in the simulation.
- Properties of the turbulent flow remain relatively constant after initial phase.

1 Introduction

Two of the most critical maneuvers in air traffic, take-off and landing, take place in the atmospheric boundary layer (ABL). This part of the atmosphere is characterised by the influence of the earth surface on the atmospheric flow which causes turbulence due to surface heating, surface roughness and shear flows. Depending on the weather situation and the surface characteristics the turbulence in the ABL can become very strong. Therefore, it is important for the design and operation of aircrafts to understand the influence of ABL turbulence on aircrafts.

Previous studies have investigated the interaction of a boundary layer with free stream turbulence. E.g. there are experimental studies investigating the interaction of a single vortex with the boundary layers of a wing or a flat plate. They are often focusing on how the vortices influence the transition from a laminar to a turbulent boundary layer. In other cases grid-generated turbulence is used to study the effect of turbulent flows on the boundary layer (see Cassel and Conlisk, 2014 for an overview of such studies). There are also studies in which numerical simulations are used to investigate the interaction between turbulence and boundary layers. In Brandt *et al.* (2004), e.g., Direct Numerical Simulation (DNS) is used to simulate a boundary layer which was triggered by inflowing synthetic turbulence. They carried out several simulations with different energy spectra and Reynolds numbers and studied the transition of the boundary layer for these cases. The study in Ghasemi *et al.* (2013) investigates the generation of entropy in the boundary layer of a flat plate in a turbulent flow using different kinds of Reynolds Averaged Navier Stokes (RANS) models and DNS. In Langari and Yang

(2013) the separated boundary layer transition on a flat plate in flows with different turbulence intensity using Large-Eddy Simulation (LES) is studied.

To the knowledge of the authors the only study which addresses the interaction of ABL turbulence with a wing in numerical simulations is Kelleners and Heinrich (2015). In this work two methods are presented to simulate the turbulent flow around a wing. The first method uses the disturbed velocity approach (Heinrich, 2014), which introduces the turbulence by an additional forcing term in the model equations. That way the effect of the turbulence on the wing can be simulated without resolving the turbulence on the grid. However, in this approach the development of the turbulent field in time is not calculated and no feedback from the wing on the turbulence is possible. In the second method LES data from a simulation of the complete ABL is used. A part of the domain from the LES of the ABL is cut out and fed into the flow model to simulate the flow of the ABL turbulence around the wing. This is a very precise method since high resolution LES data from a simulation of the complete ABL is used. However, computationally it is very expensive to run a simulation which develops a realistic ABL before feeding the turbulence into the flow solver.

In this paper we present an alternative way of simulating the flow around a wing. Instead of using LES data from a simulation of the complete ABL we use measurement data from flight measurements and feed them into a synthetic turbulence generator. This turbulence generator creates the initial 3D turbulent flow field for the simulation of the flow around the wing. The generated turbulence represents some important statistical properties of the ABL turbulence (Auerswald *et al.*, 2012). That way the turbulent flow can be explicitly resolved in the flow simulation but at the same time there is no need for the expensive simulation of the ABL. Instead the ABL turbulence is represented by the synthetic turbulence which needs much less resources to compute and still represents important features of the ABL. Nevertheless, the synthetic turbulence can, of course, not contain all the properties of a real ABL flow. The differences between the synthetic turbulence and turbulence from an LES are investigated in Knigge *et al.* (2015).

Section 2 presents the setup of the model and gives a short overview over the synthetic turbulence generator. In section 3 the simulation results are shown together with an analysis of the development of the turbulence during the simulation. The focus lies especially on the change of turbulence statistics when the turbulent flow faces changes in grid properties and turbulence models. Section 4 gives a summary of the presented results and an outlook for future work.

2 Method

2.1 Simulation strategy

For the simulation of the turbulent flow around the wing, the flow solver DLR-TAU (Schwamborn *et al.*, 2006) is used. The model domain consists of two grids (see Fig. 1) which are connected using the Chimera method (Schwamborn *et al.*, 2006). The first grid is an unstructured body-fitted grid which allows the simulation of the flow around the wing. A Cartesian grid is used as secondary grid which contains the turbulent flow field and is positioned upstream of the wing. On that grid the turbulent flow is transported towards the wing by moving the Cartesian grid with the mean flow. This allows the synthetic turbulence to adjust to the model physics while it is transported towards the wing. Only when the Cartesian grid is close to the wing the Cartesian grid is stopped and the turbulence leaves the Cartesian grid and enters the first grid on which the turbulence can interact with the wing. That way the turbulence stays on the Cartesian grid as long as possible during the simulation which reduces the numerical dissipation of the small scale turbulence.

The Cartesian grid is a cubic grid which consists of ca. 23 million points. Its normalised grid spacing is $\Delta x/c = 0.23$ (where c is the chord length of the wing) and the normalised length of the cube edges is $L/c = 66.3$. This allows to resolve a reasonable range of turbulent scales from the ABL. The unstructured grid consists of around 10 million points and has a normalised grid spacing ranging from $\Delta x/c = 1.6 \cdot 10^{-6}$ near the wing to up to $\Delta x/c = 13.3$ at the outer boundary. The sector upstream of the wing on the unstructured grid is refined to around $5\Delta x$ of the Cartesian grid. This is necessary to ensure proper interpolation between the two grids further away from the wing. In a radius around the wing of around $4c$ the resolution of the unstructured grid is increased to $\Delta x/c = 0.23$ (the same like on the Cartesian grid). This radius is the distance at which the Cartesian grid is stopped for the turbulent field to flow onto the unstructured grid.

For the design of the wing an ONERA-A airfoil is stretched in spanwise direction.

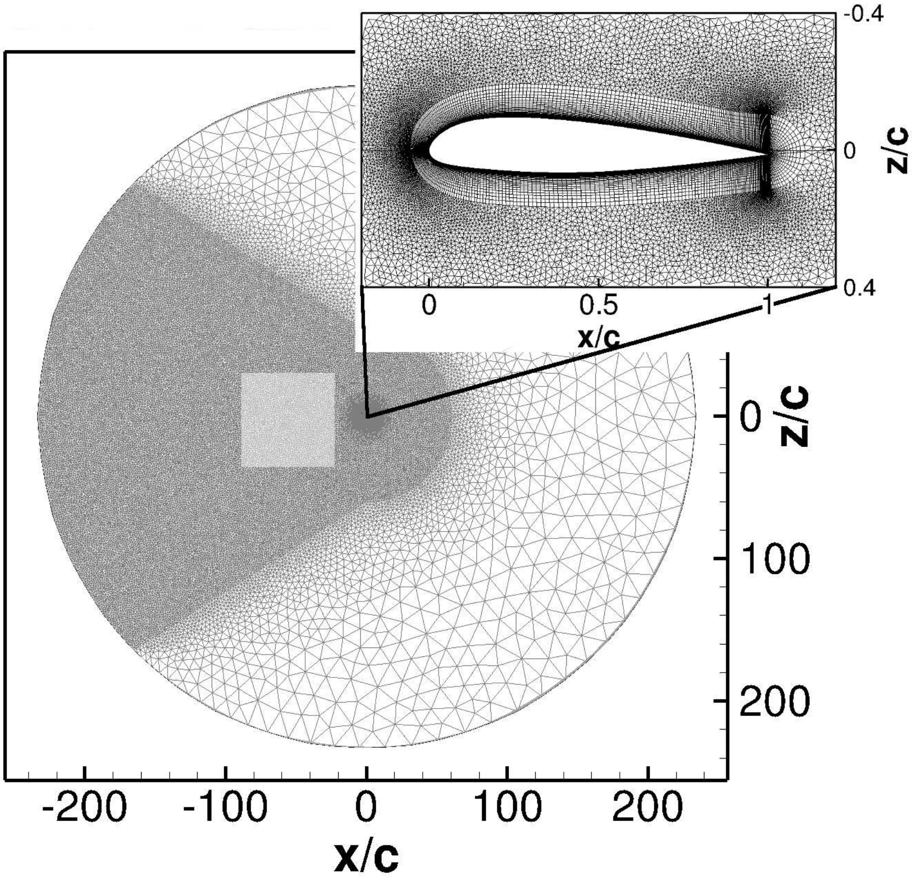

Figure 1: *Model domain for the Chimera simulations with DLR-TAU. The domain consists of two grids. The primary grid is body-fitted around the wing. The secondary Cartesian grid (grey block) is used to simulate the turbulent flow in front of the wing.*

Round wing tips are added to the wing to minimise the disturbance of the flow. The chord length is 3 m and the wing span is 15 m. The distance of the first wall-normal point ranges from $y1^+ = 0.1$ to $y1^+ = 1$. Only for some cells at the wing tips towards the trailing edge, distances of up to $y1^+ = 1.5$ are reached. Around the wing surface 74 wall-normal layers of hexahedral elements are included. The total number of surface points on the wing is about 70000 with 150 cells resolving the spanwise direction.
For the simulation of the flow, an angle of attack of 6 degrees is chosen. The time step size is set to $1.25 \cdot 10^{-4}$ s or $t^* = U/c \cdot t = 2.54 \cdot 10^{-3}$ in dimensionless units (where U is the mean velocity in x-direction and c the chord length). By setting the mean flow speed to 67.7 m/s, it takes the turbulent flow field around 1 s ($t^* = 20.35$) to reach the

wing. This ensures enough time for the initial turbulent flow field to adapt to the model physics. It takes the wing around 3 s ($t^* = 61.05$) to fly through the turbulent flow field which leads to a total simulation time of 4 s ($t^* = 81.40$).

2.2 Model setup

For modeling the unresolved turbulence the Detached-Eddy Simulation (DES) formulation of the Menter SST k-ω model (see Travin *et al.*, 2008) is used. In DES the parts of the turbulent flow which are of particular interest are simulated using LES while those parts which would be very expensive to simulate using LES are simulated using RANS. The model switches between RANS and LES behaviour by switching between different length scales in the model formulation. The DES length scale is defined as:

$$\tilde{l} = \min(l_{k\text{-}\omega}, C_{\mathsf{DES}} \cdot \Delta), \tag{1}$$

where $l_{k\text{-}\omega}$ is the RANS length scale, C_{DES} is a constant and $\Delta = \max(\Delta_x, \Delta_y, \Delta_z)$ is the maximum of the grid spacings in all three dimensions. If $\tilde{l}/l_{k\text{-}\omega} = 1$ the model is in RANS mode, since then the length scale is equal to the RANS length scale. If $\tilde{l}/l_{k\text{-}\omega} < 1$ the model is in LES mode, since the length scale is defined as the minimum of the RANS and the LES length scale. In Fig. 2, $\tilde{l}/l_{k\text{-}\omega}$ is depicted for $t^* = 40.1$ when the Cartesian grid was already stopped and a part of the turbulent field has already left the Cartesian grid. The box in the top left corner of Fig. 2 provides a zoomed in view on the wing. The boundary layer of the wing is simulated using RANS. This is forced in the model by setting a fixed distance around the wing within which RANS is used. The parts on the unstructured grid outside the boundary layer, where the cell size is small enough compared to the turbulent eddies, are modeled using LES. Further away from the wing where the grid resolution gets too coarse to resolve turbulent eddies properly, the model switches to RANS mode. The turbulence on the Cartesian grid is modeled using LES. The left hand side of the Cartesian box is in RANS mode because a part of the turbulence field already left the Cartesian grid through the right boundary plane.

In Fig. 3 a yz-plane of $\tilde{l}/l_{k\text{-}\omega}$ in between the wing and the Cartesian grid is shown. Since in y- and z-direction the grid is becoming coarser further away from the center, those parts are simulated in RANS mode while there is a tube in front of the wing within which the model is in LES mode.

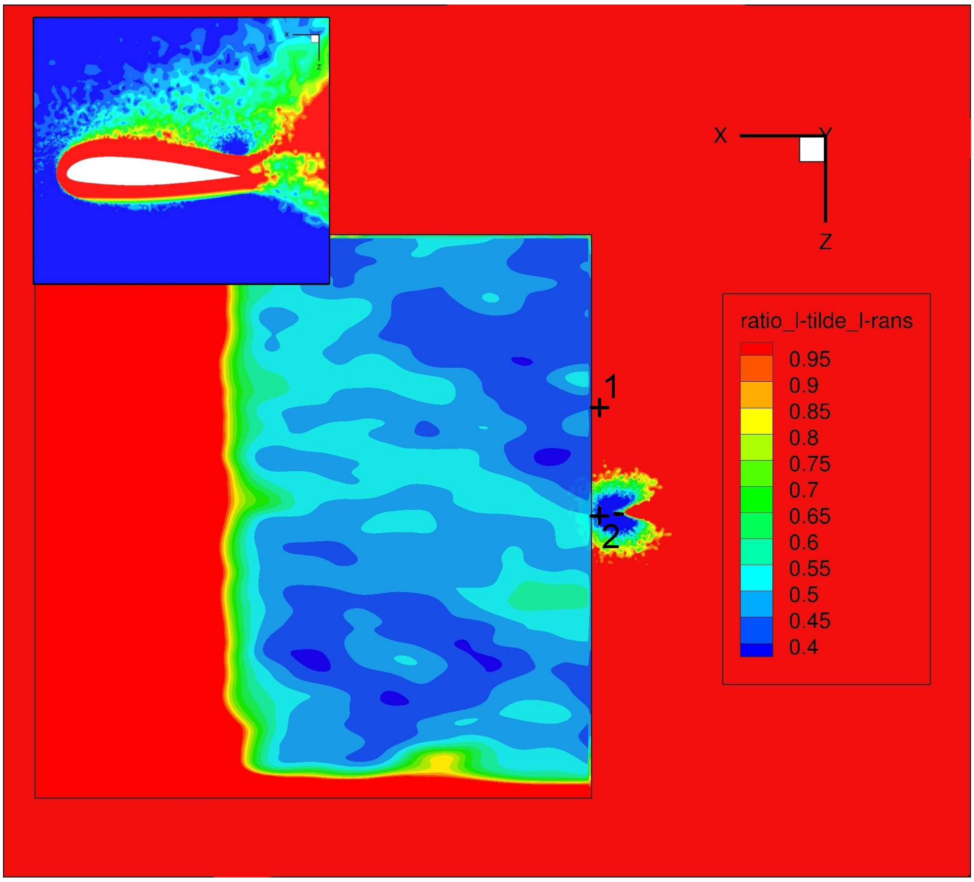

Figure 2: *Ratio of $\tilde{l}$ and $l_{k\text{-}\omega}$ in an xz-plane. The Cartesian grid is depicted by the big box on the left hand side, the wing is in front of the Cartesian grid to the right and the box in the top left corner provides a zoomed in view on the wing. Position 1 and 2 marked by the crosses indicate measurement points explained in sec. 3.*

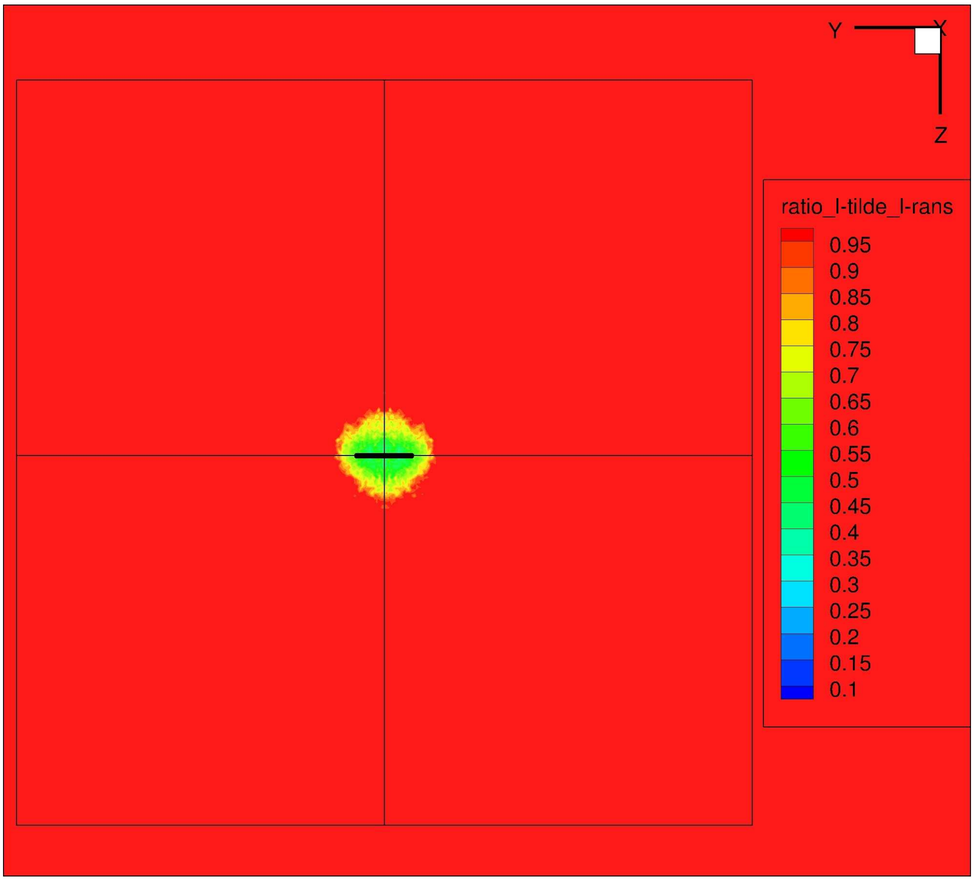

Figure 3: *Ratio of* $\tilde{l}$ *and* $l_{k\text{-}\omega}$ *in a* yz*-plane with the wing in the center. The big box is depicting the Cartesian grid.*

The flow solver applies central differences for discretising the viscous fluxes. The inviscid fluxes are discretised using a skew-symmetric scheme (Kok, 2009) and time discretisation is performed using a second order backward differencing method with dual time stepping (Jameson, 1991).

For the surface of the wing viscous wall boundary conditions are used. The boundary in x- and z-direction is a farfield boundary while the boundaries in y-direction are set to be symmetry planes.

2.3 Initial fields

The simulation needs to be initialised on both the unstructured body-fitted and the Cartesian grid. For the initial solution on the unstructured grid a RANS simulation was performed without the Cartesian grid. In this simulation the steady flow field around the wing was calculated which serves as initial solution for the unstructured body-fitted grid in the simulation of the turbulent flow around the wing.

The flow on the Cartesian grid needs to be initialised with a 3D turbulent wind field. Since there is no earth surface in the model domain there is no mechanism to develop an ABL during the flow simulation. To initialise the simulation with realistic turbulence, measurement data from the ABL are used to generate a 3D synthetic turbulent wind field. The turbulence generator is based on a Fourier approach where the measured energy spectrum determines the Fourier coefficients:

$$\vec{v}(\vec{x}) = \sum_{n=1}^{N}\sum_{m=1}^{N}\sum_{l=1}^{N}\Big(\vec{C}_{n,m,l}\big(\cos(\vec{k}_{n,m,l}\cdot\vec{x}) + i\sin(\vec{k}_{n,m,l}\cdot\vec{x})\big)\Big),$$

where $\vec{C}$ is the amplitude vector, $\vec{k}$ is the wavenumber vector and $\vec{x}$ is the position vector. By calculating the absolute value of the amplitude vector using:

$$|\vec{C}_{n,m,l}| = \sqrt{E(|\vec{k}_{n,m,l}|)\Delta|\vec{k}_{n,m,l}|},$$

the measured energy spectrum $E(k)$ can be reproduced in the synthetic turbulence. The resulting wind field is divergence-free and isotropic. Additionally, a Cholesky decomposition is applied to the synthetic turbulence field to ensure correct correlations.

The measurements for the input statistics of the turbulence generator were taken by the airborne measurement platform Helipod (Bange *et al.*, 2007) which provides high-resolution measurements of the 3D wind vector. Measurements from a sunny summer day near Berlin, Germany in 2003 were chosen to represent a convective ABL. The statistics of these measurements were used to generate the 3D wind field to initialise the turbulence on the Cartesian grid (see Auerswald *et al.*, 2012 for a detailed description of the turbulence generator and the measurement data used).

Fig. 4 shows the initial flow fields for the Cartesian grid (a) and the unstructured body-fitted grid (b) for the x-component of the velocity normalised by the mean velocity in x-direction. Since the Cartesian grid is moving with the mean flow and the wing has an angle of attack of 6 degrees and a true air speed of 68.1 m/s ($|\vec{v}|/U = 1.12$), the mean vertical velocity in the Cartesian grid is 7.1 m/s ($w/U = 0.12$). In Fig. 4 (a) the wing is visible as a small dot on the right hand side of the picture. The initial flow field around the wing is shown in Fig. 4 (b). It was generated running a RANS simulation on the unstructured body-fitted grid only, without the turbulent field and with a constant flight speed.

3 Results

In this section results from the simulation of the turbulent flow around the wing are presented. In Fig. 5 snapshots of the turbulent flow around the wing represented by the normalised vertical velocity are shown for six different points in time: $t^* = 0$ (a), $t^* = 9.4$ (b), $t^* = 18.6$ (c), $t^* = 38.9$ (d), $t^* = 56.7$ (e) and $t^* = 77.1$ (f). The colors depict the normalised vertical velocity. On the right hand side of the pictures the wing is visible by its strong stationary flow field. The Cartesian grid is depicted by two squares marking the inner (small square) and outer (big square) interpolation boundary. The inner interpolation boundary is used to interpolate the data from the Cartesian grid onto the unstructured grid while at the outer interpolation boundary the data from the unstructured grid is interpolated onto the Cartesian grid. For $t^* = 0$ the turbulent field is only present on the Cartesian grid. Until $t^* = 18.1$ the Cartesian grid and the turbulent field move towards the wing. In that phase the turbulent field is restructured significantly. The reason for that are sound waves traveling through the model domain which are triggered by the pressure and density fields, which are not in full agreement with the continuity equation (see Auerswald *et al.*, 2012 for details how the initial density and pressure fields are calculated). It can be seen that in the interval from $t^* = 9.4$ to $t^* = 18.6$ the changes in the velocity field have become much smaller

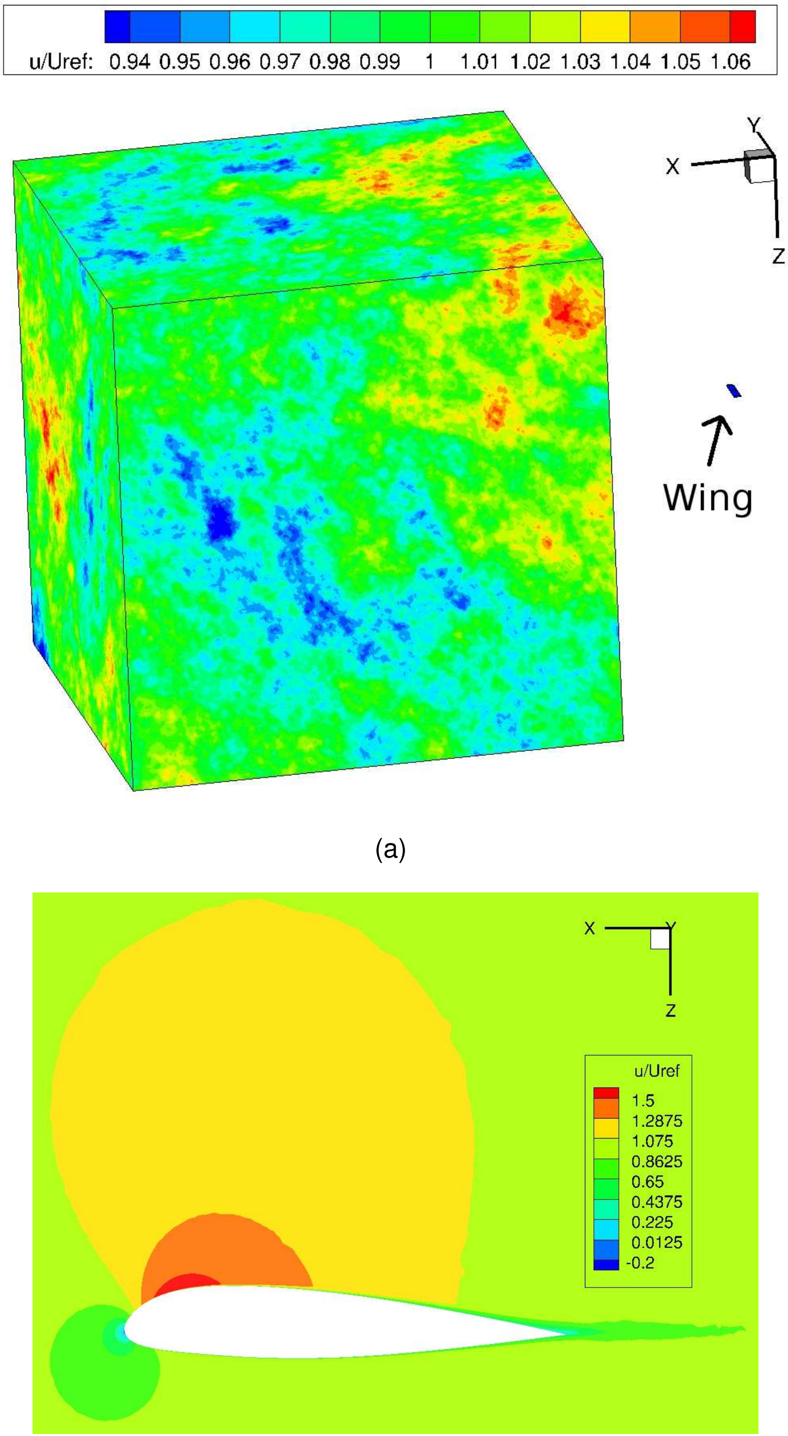

(a)

(b)

Figure 4: *Initial flow field on the Cartesian grid (a) and around the wing (b). In colors the velocity in x-direction normalised by the mean velocity in x-direction is shown.*

than in the first interval from $t^* = 0$ to $t^* = 9.4$. At $t^* = 18.1$ the Cartesian grid is stopped and the turbulent field moves out of the Cartesian grid onto the unstructured grid. At that time the turbulent field has stabilised and remains more or less constant while it is moving towards the wing. It can also be seen that on the unstructured grid some of the small scale structures are lost (visible in the space between the two squares where the field data is already interpolated onto the unstructured grid) which will be discussed later in more detail using energy spectra (see Fig. 7).

The turbulent field in the simulation is facing many different numerical and physical conditions. It is initialised with estimated pressure and density fields which do not match the velocity field with respect to the continuity equation, it is transported from a Cartesian grid to an unstructured grid and from an LES domain to a RANS domain (in parts of the field), and it enters the stationary flow field of the wing. To understand how these factors influence the properties of the turbulence, the statistics of the turbulent field were calculated at different points in the simulation. First, the 3D statistics of the initial turbulent field are compared to the turbulent field on the Cartesian grid at $t^* = 18.1$ (when the Cartesian grid is stopped). Then time series at two different locations on the unstructured grid were recorded. One location is in front of the wing, named position 2, at the same altitude as the wing and the other one is in front of the wing but at a higher altitude outside the stationary flow field of the wing (position 1). The statistics of the time series of these two points are compared to the respective space series from the turbulent field on the unstructured grid at $t^* = 81.1$ which would be convected through those points in front of the wing during the simulation. Fig. 6 shows the setup in the model domain.

3.1 Results from the moving grid ($t^* = 0$ to $t^* = 18.1$)

In Fig. 7 the 3D energy spectrum of the initial turbulent flow field (red, solid) and the turbulent flow field at $t^* = 18.1$ (green, dashed), both calculated on the Cartesian grid, are compared. The dotted blue line shows the $k^{-5/3}$ slope of the inertial subrange. To reduce the noise in the spectra an average over a wavenumber interval of 20 values was applied. The spectrum of the initial field follows the $k^{-5/3}$-slope throughout the whole spectral range. The wiggles which start to occur at around $k \cdot c = 0.3$ are caused by the Fourier transform because the turbulent field is non periodic. They

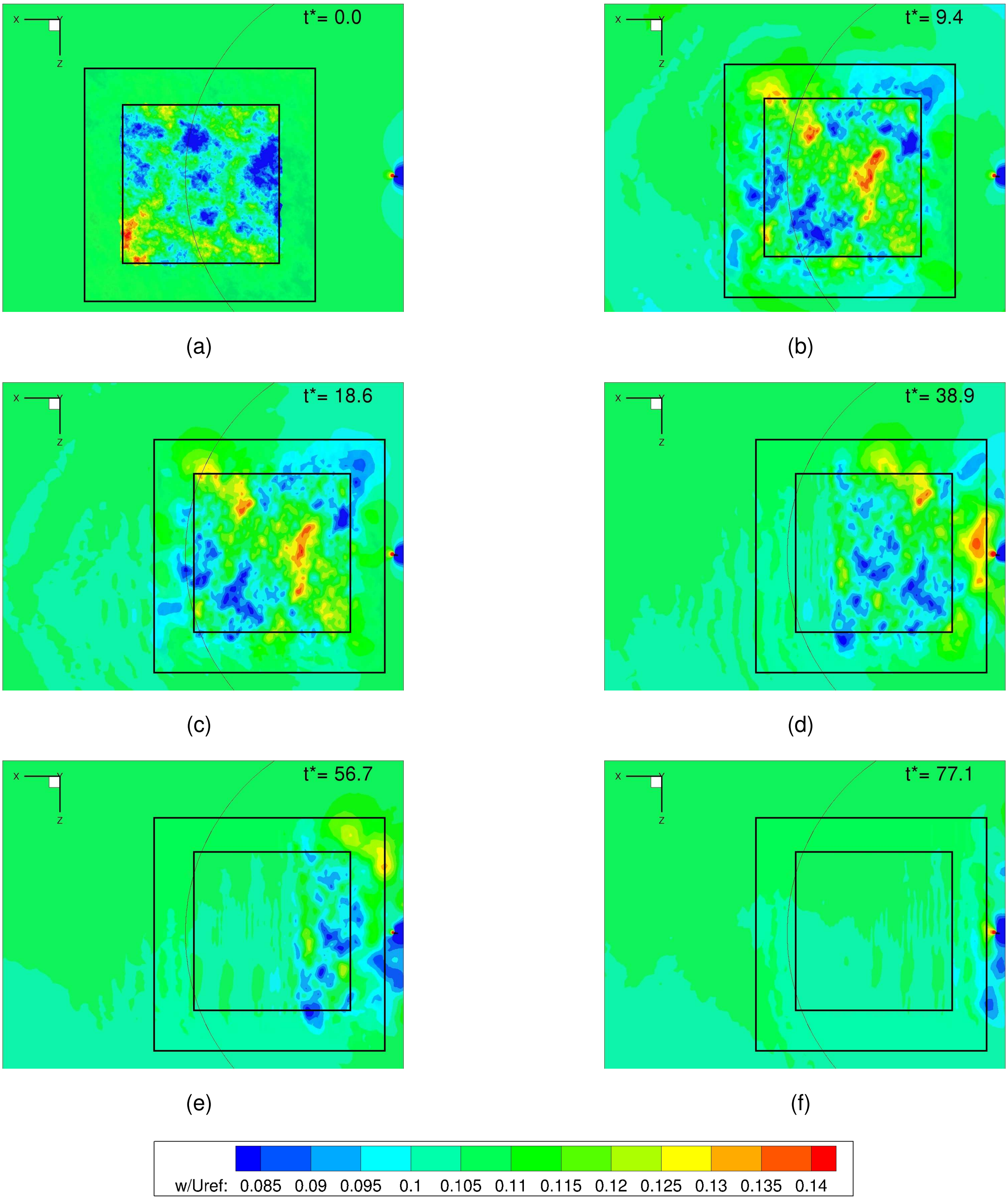

(a) (b) (c) (d) (e) (f)

Figure 5: *Vertical velocity (normalised by the mean velocity in x-direction) at time* $t^* = 0$ *(a),* $t^* = 9.4$ *(b),* $t^* = 18.6$ *(c),* $t^* = 38.9$ *(d),* $t^* = 56.7$ *(e) and* $t^* = 77.1$ *(f). The big square marks the outer interpolation boundary, the small square the inner interpolation boundary.*

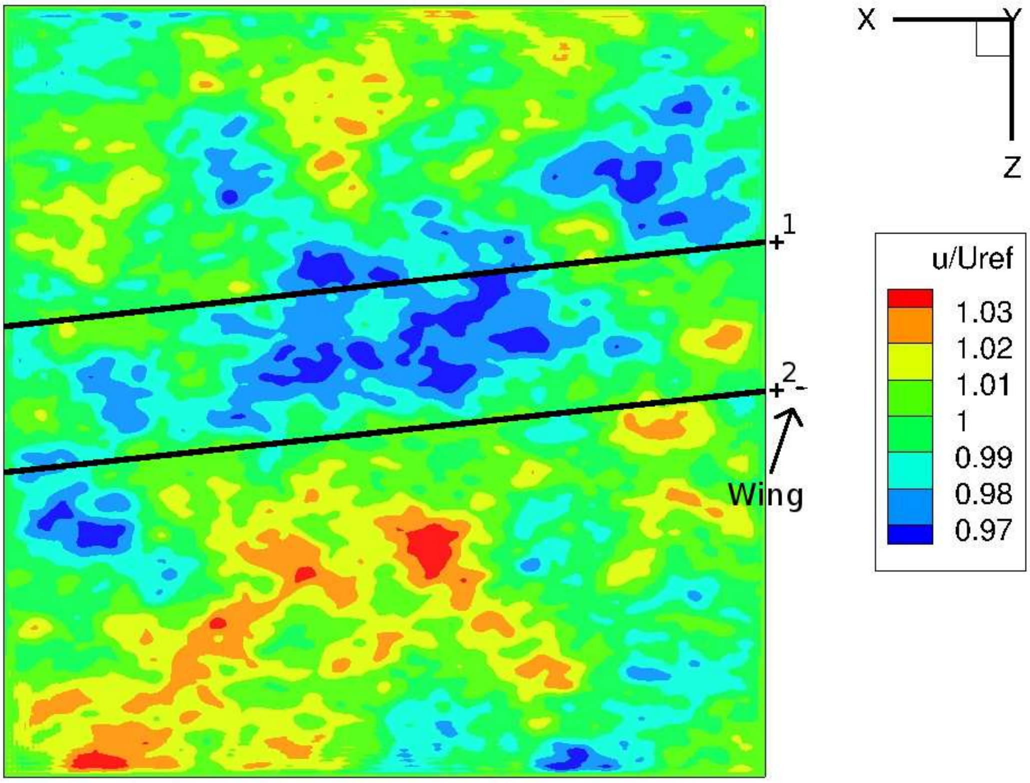

Figure 6: *Paths through the Cartesian grid from which the space series were extracted (black lines). The crosses mark the position on the unstructured grid from which the time series were taken. In front of the turbulence field the wing can be seen as a black dot near position 2. The colors in the turbulence field are representing the normalised velocity in* x*-direction.*

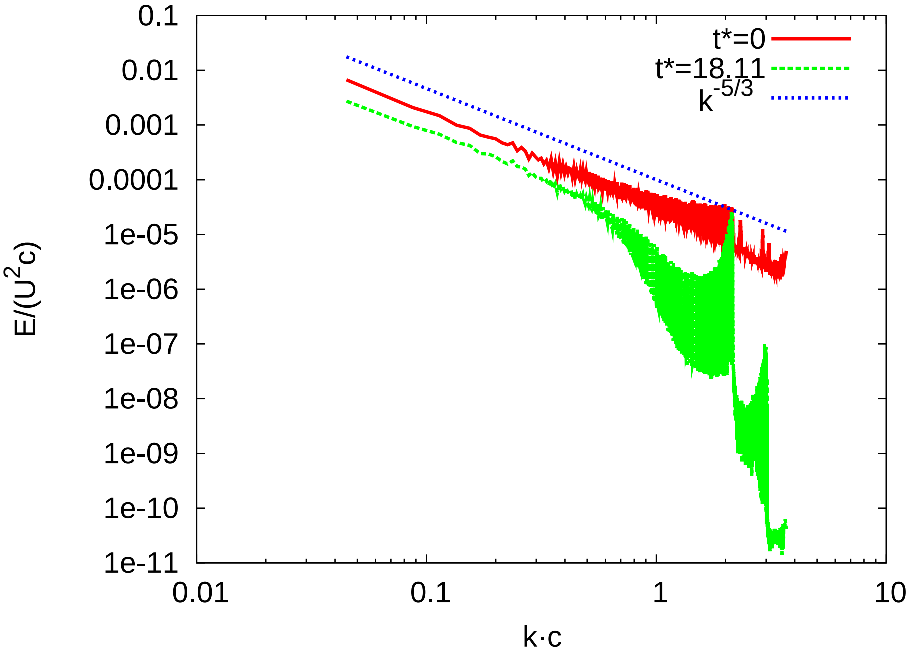

Figure 7: *3D energy spectra of the initial turbulent wind field (red, solid) and the turbulent wind field at* $t^* = 18.1$ *(green, dashed), both calculated on the Cartesian grid, and* $k^{-5/3}$ *slope of the inertial subrange (blue,dotted). The energy spectra were smoothed by averaging over intervals of 20 data points.*

reach a maximum at $k \cdot c = 2.16$ which is equal to the wave length of two times the grid spacing. The spectrum of the turbulent field at $t^* = 18.1$ shows overall lower values of the spectral turbulent kinetic energy (TKE) in the whole wavenumber range. The total TKE (resolved + modeled) drops from $K/U^2 = 1.51 \cdot 10^{-3}$ at $t^* = 0$ to $K/U^2 = 0.63 \cdot 10^{-3}$ at $t^* = 18.1$, due to a combined effect of turbulence decay and numerical dissipation. At low wave numbers the spectrum follows the $k^{-5/3}$-slope but there is a significant deviation from that slope starting at around $k \cdot c = 0.45$. This corresponds to roughly 10 times the grid spacing and is caused by the numerical dissipation of the small scales during the simulation. Also in this spectrum wiggles are visible which reach a maximum at two times the grid spacing and are also caused by the Fourier transform because of the non periodic turbulent field.

In table 1 the cross-correlations γ_{ij} for the turbulent wind field at $t^* = 0$ and $t^* = 18.1$ are compared. It can be seen that the cross-correlations change quite a lot during the simulation without showing a clear trend. γ_{uv} and γ_{uw} decreased and changed sign

	γ_{uv}	γ_{uw}	γ_{vw}
$t^* = 0$	0.005	0.264	0.063
$t^* = 18.1$	-0.143	-0.182	0.310

Table 1: *3D cross-correlations γ_{ij} for the initial turbulent wind field ($t^* = 0$) and the turbulent wind field at $t^* = 18.1$.*

while γ_{vw} did not change sign and increased. This might be due to the initial mismatch of the velocity field with the density and pressure field and the synthetic turbulence adjusting to the model physics during the simulation. According to theory, anisotropic turbulence without external forcing should return to an isotropic state, meaning that the cross-correlations should become zero. However this would happen on a much larger time scale than the $\Delta t^* = 18.1$ simulated here (see Chung and Kim, 1995 for more details on the return to isotropy).

Fig. 8 shows the probability density functions (PDF) for the three normalised velocity components at time $t^* = 0$ (red, solid) and $t^* = 18.1$ (green, dashed). For comparison the normal distributions for the respective variances are plotted for $t^* = 0$ (blue, dot-dashed) and $t^* = 18.1$ (pink, dotted). The PDF of the initial field shows only small deviations from the normal distribution in all three velocity components. At $t^* = 18.1$ the PDFs of the velocity components are narrower than the ones in the initial field which is because of the loss of TKE and therefore lower variances for all three velocity components. But the comparison with the normal distribution for the lower variances at $t^* = 18.1$ shows that the PDFs still follow the normal distribution with only small deviations. In comparison to the normal distribution the PDFs for all three velocity components are generally narrower and reach a larger maximum value.

In Fig. 9 the longitudinal PDFs of the normalised velocity increments for u for 5 different separation distances, $2\Delta x$, $4\Delta x$, $8\Delta x$, $16\Delta x$ and $32\Delta x$, are plotted for the turbulent field on the Cartesian grid at time $t^* = 0$ (a) and $t^* = 18.1$ (b). The shape of the PDF of the velocity increments is influenced by the intermittency of the turbulent flow. Due to intermittent fluctuations the PDFs of the velocity increments show tails at the left and right end of the distribution for small separation distances. The smaller the separation distance the bigger the deviation from the normal distribution is expected (see Sreenivasan, 1999). According to Fig. 9 the PDFs of the velocity increment follow a normal distribution for all separation distances initially since the synthetic turbulence

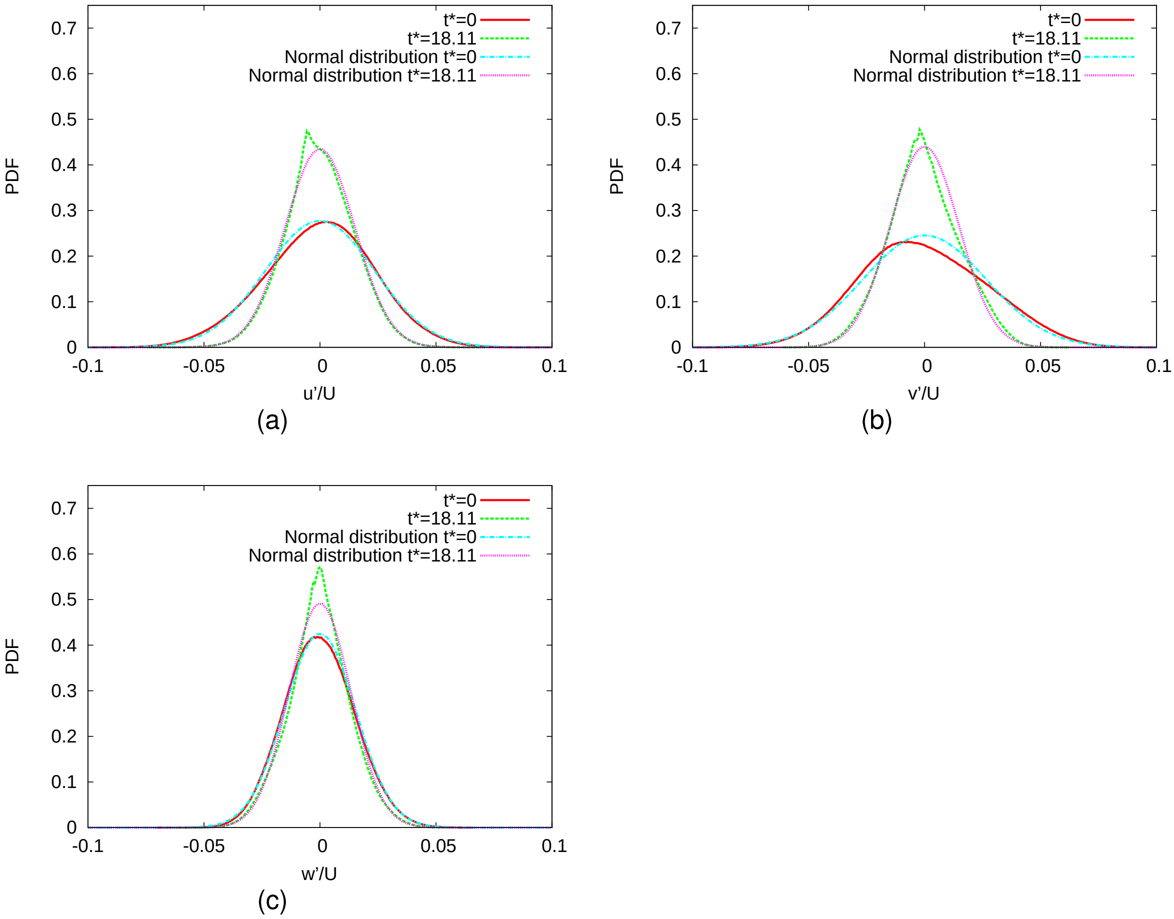

(a)

(b)

(c)

Figure 8: *PDFs of the normalised velocity component in* x*-direction (a),* y*-direction (b) and* z*-direction (c) for* $t^* = 0$ *(red, solid) and* $t^* = 18.1$ *(green, dashed). For comparison the normal distributions for the respective variances are shown for* $t^* = 0$ *(blue,dot-dashed) and* $t^* = 18.1$ *(pink, dotted).*

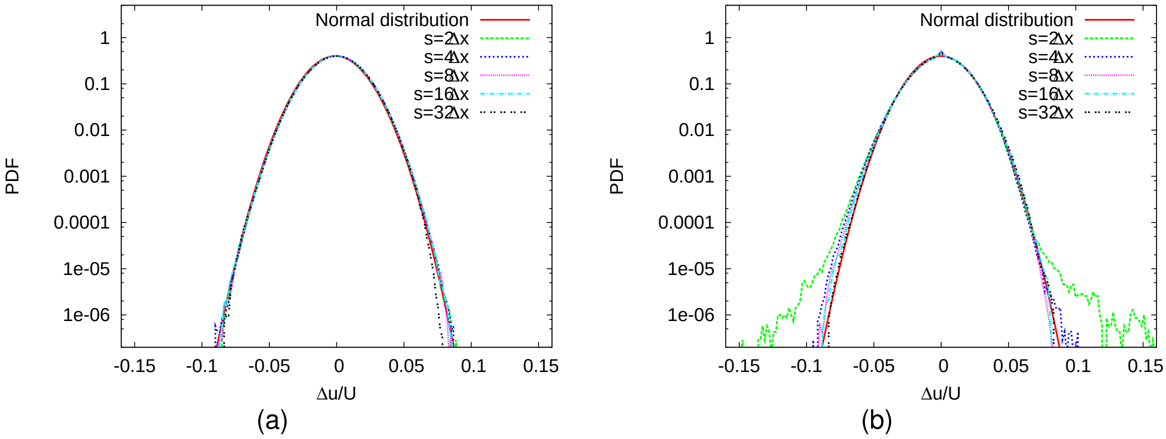

(a) (b)

Figure 9: *Normalized longitudinal PDF of the increments of the* x*-component of the normalised velocity calculated from the initial wind field (a) and the DLR-TAU result at* $t^* = 18.1$ *(b). Depicted are separation distances* $s/c = 0.46$ *(green),* $s/c = 0.93$ *(blue),* $s/c = 1.86$ *(purple),* $s/c = 3.73$ *(light blue) and* $s/c = 7.46$ *(black). For comparison the PDF of the normal distribution is plotted in red.*

does not account for intermittent effects. But after only a time interval of $\Delta t^* = 18.1$ the PDFs already exhibit tails for small separation distances. According to Auerswald *et al.* (2012) the PDFs for bigger separation distances should also develop tails within a time interval of $\Delta t^* = 60$ leading to a more realistic representation of the turbulent field inside the flow simulation. The development of the tails results from the solution of the Navier-Stokes equation directly and has been explained theoretically in Li and Meneveau (2005).

3.2 Evolution of the turbulence on the unstructured grid ($t^* = 18.1$ to $t^* = 81.4$)

After analysing the turbulent field during the interval from $t^* = 0$ to $t^* = 18.1$, now the focus will be on the part of the simulation where the turbulent field leaves the Cartesian grid and flows towards the wing. Until the Cartesian grid was stopped the sound waves which were present in the beginning of the simulation disappeared and the turbulent field became more or less stationary. Fig. 10 shows the normalised 1D energy spectra in x-direction for position 1 and 2 (cf. Fig. 6). In order to get smoother spectra and significant statistics the spectra were averaged over all y locations within the width of the Cartesian grid. To be able to directly compare the spectra from the time series and space series, the latter were converted into time series using the mean flight speed. At position 1 the turbulence model is in RANS mode for all y. For larger absolute values of y/c the size of the grid cells at position 1 is around $\Delta x/c = 1.7$. Closer to $y/c = 0$ the grid cell size is approx $\Delta x/c = 0.87$.

Since position 2 is located at the same height z like the wing, the turbulence model is either in RANS ($\Delta x/c = 1.3$) or LES mode ($\Delta x/c = 0.2$) depending on y (see Fig. 3 and 6). Therefore for position 2 two kinds of energy spectra were calculated representing LES (blue, short dashed) and RANS (pink, dotted) respectively. The spectra of the respective space series along the lines through the Cartesian grid are shown for position 1 and for position 2, and additionally, the $f^{-5/3}$ slope of the inertial subrange is plotted. The energy spectra calculated from the line through the Cartesian grid at $t^* = 18.1$ are almost identical in position 1 and 2 which was expected since the initial turbulent field was generated with the same statistics at each point of the Cartesian grid. For small frequencies the spectra for the time series taken at point 1 and 2 are almost identical to the spectra on the Cartesian grid. In this frequency range there is almost no dissipation of energy visible and all spectra follow the $f^{-5/3}$-slope of the inertial subrange. Also the spectra in the LES and RANS part of the domain are very similar. At high frequencies though, the spectra at point 1 and 2 drop significantly compared to the spectra on the Cartesian grid. The spectra on the Cartesian grid deviate from the $f^{-5/3}$-slope at much higher frequencies than the spectra from the unstructured grid. That means in the small scales there is significantly more dissipation on the unstructured grid compared to the Cartesian grid. Also on the unstructured grid there is almost no difference between the spectrum in the RANS and LES part of the domain. Even though the spatial resolution is coarser in the RANS part the dissipation of the small resolved scales is almost the same like in the LES part of the domain. The time the turbulence spends in the RANS domain in point 1 is probably too short for the turbulent flow to be affected significantly by the RANS model.

The values of the normalised resolved TKE K/U^2 are presented in tab. 2. It shows that in general the variances in the time series of point 1 and 2 are lower than in the space series from the Cartesian grid. The values for the RANS and LES part in position 2 show no significant difference in resolved TKE.

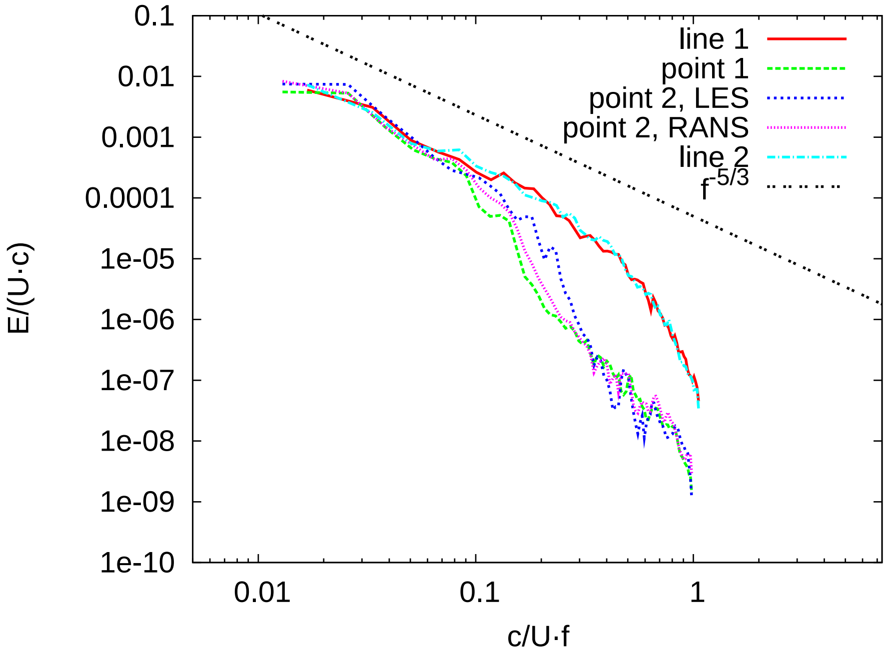

Figure 10: *Normalised 1D energy spectra (summation of the spectra for u, v and w) in x-direction for the space series for position 1 (red, solid line), the time series for position 1 (green, long dashed), the time series for position 2 in the LES part (blue, short dashed), the time series in the RANS part (pink, dotted) and the space series for position 2 (light blue, dash-dotted). For comparison the $f^{-5/3}$-slope of the inertial subrange is plotted in black (double dotted).*

	position 1	position 2
point RANS	$0.35 \cdot 10^{-3}$	$0.48 \cdot 10^{-3}$
point LES	-	$0.46 \cdot 10^{-3}$
line	$0.56 \cdot 10^{-3}$	$0.68 \cdot 10^{-3}$

Table 2: *Normalised TKE K/U^2 for the time and space series in position 1 and 2.*

In Fig. 11 the cross-correlations of the velocity components, which indicate the anisotropy of the velocity field, are shown over y/c (i.e. in span wise direction). The left column shows the correlations calculated from the time series (red, solid line) in point 1 and the correlation from the respective line through the turbulent field (blue, dashed). The right column shows the same for position 2. The shaded areas indicate the random statistical error calculated following Lenschow and Stankov (1986). In all six cross-correlations a strong dependency on y can be observed. Furthermore, it can be seen from the figure that there are only small differences between the correlations calculated from the time series and the space series. That means that while the turbulent field leaves the Cartesian grid and flows towards the wing the cross-correlations of the velocity components are not changing much. The deviations seem to be a bit bigger in position 2 which could be due to the effect of the wing which disturbs the upstream flow field.

After studying the properties and behaviour of the turbulent field the interaction of the turbulence with the wing is analysed. Fig. 12 shows the time series of the lift (a) and drag (b) coefficient. Until around $t* = 20$ the influence of the sound waves from the initial turbulent field can be seen. After $t* = 20$ the turbulent field is reaching the wing. The effect of some up- and downdrafts can be observed with c_L and c_D reacting inversely to the disturbances. That means that whenever the lift is increasing the drag is decreasing and the other way around. This effect is known as Knoller-Betz effect (e.g. Jones *et al.*, 1998).

4 Conclusions

A method to simulate the turbulent flow around a wing was presented. The simulation was initialised with synthetic turbulence which used measurement data as input. The presented method used Chimera interpolation to move a Cartesian grid containing the turbulent field over an unstructured grid towards a wing. In that first phase of the simulation sound waves could be observed which were created by a mismatch of the initial turbulent field with the pressure and density field. This imbalance led to a reorganisation of the turbulent field causing a significant change in the cross-correlations of the velocity components. The shape of the energy spectrum remained constant for the large scales. In the small scales, up to 10 times the grid spacing, the turbulent

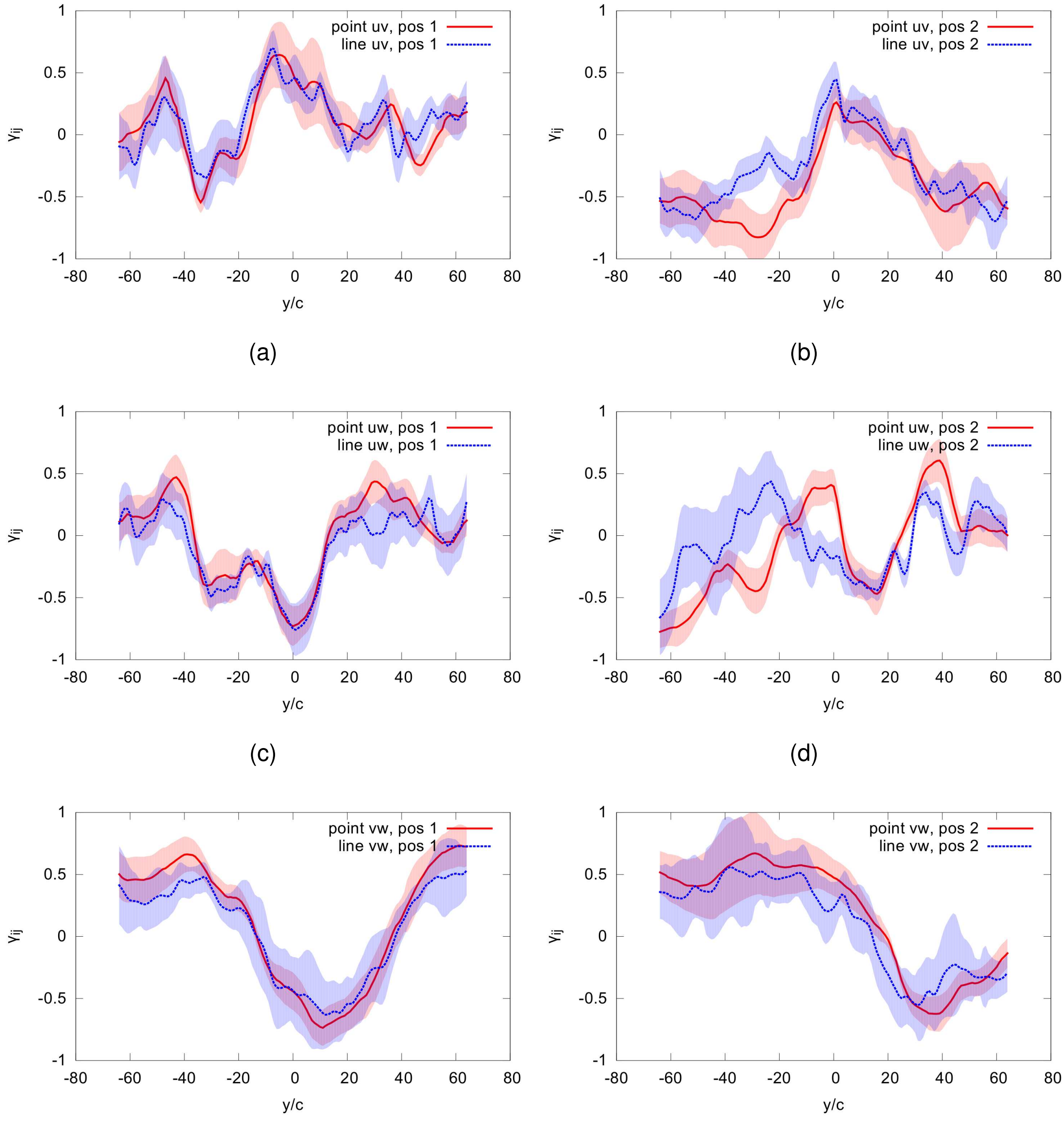

(a) (b)

(c) (d)

(e) (f)

Figure 11: *Cross-correlations* γ_{uv} *at position 1 (a),* γ_{uv} *at position 2 (b),* γ_{uw} *at position 1 (c),* γ_{uw} *at position 2 (d),* γ_{vw} *at position 1 (e) and* γ_{vw} *at position 2 (f) over* y/c *for the time series measured on the unstructured grid (red, solid line) and the space series taken from the Cartesian grid (blue, dashed). The shaded areas represent the random statistical error.*

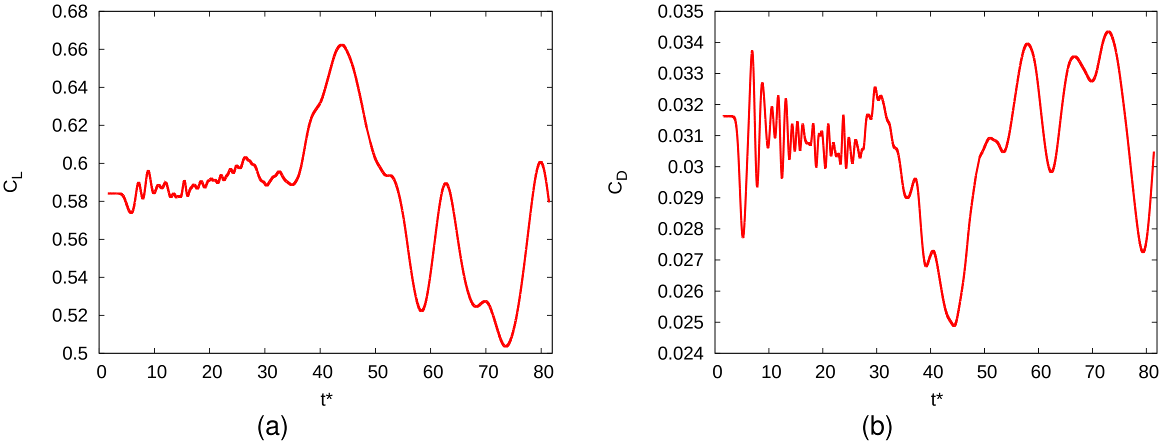

Figure 12: *Time series of the lift coefficient (a) and drag coefficient (b).*

kinetic energy was mostly lost due to numerical dissipation. Since there was no mechanism to produce ABL turbulence inside the model domain an overall decay of TKE was observed in the whole spectral range. At the same time the PDFs of the velocity components became narrower due to the decrease in variance but remained normally distributed. The PDFs of the velocity increments were normally distributed at the beginning of the simulation. However, during the simulation the PDFs developed tails, at least for the smallest separation distances, indicating the development of intermittent turbulence during the simulation. Intermittency is typical for realistic turbulence and intermittency tails were found in many previous experimental studies. The simulated turbulence shows a realistic representation of this phenomenon (Sreenivasan, 1999).
Once the Cartesian grid was stopped the turbulent field had stabilised (to quasi-stationarity) and was not affected by sound waves anymore. The time series at two points on the unstructured grid were analysed and compared to the space series on the Cartesian grid which would be convected through those two points during the simulation. One point was located in front of the wing far above the area influenced by the wing. This location was in the RANS part of the model domain. The other point was located at the same distance in front of the wing as point 1 but at the same altitude as that of the wing. In this part of the domain the grid resolution was much finer than in point 1 which allowed to model the turbulence using LES. Compared to the spectra from the space series on the Cartesian grid, the spectra from the time series on the unstructured grid showed a significant loss of energy in the small scales for both position 1 and 2. In the

large scales the spectra were very similar and also the spectra from the time series in the RANS and LES part were almost identical. At least in this short time of simulation the coarser grid and RANS turbulence model in point 1 did not affect the turbulence in a negative way. In the comparison of the cross-correlations a good match was found between the cross-correlations from the space series on the Cartesian grid and the time series on the unstructured grid. Especially for position 1 the differences were very small. In position 2 bigger differences could be seen between the Cartesian and unstructured grid. It was not clear where those differences came from but it might be due to the influence of the wing on the upstream flow field.

In the time series of the lift and drag coefficient the influence of the turbulence on the wing could be observed. The wing was hit by a few up and down drafts which lead to inversely changing coefficients. With increasing lift the drag was decreased and with decreasing lift the drag was increased due to the Knoller-Betz effect (Jones *et al.*, 1998).

In future studies an improved method for estimating the initial pressure and density fields should be used to make sure that the statistical properties with which the turbulent field is initialised (especially the cross-correlations) will reach the wing later in the simulation. Once the turbulent field was reorganised and the velocity was in match with the pressure and density fields the statistical properties of the turbulent flow were quite constant (apart from the inevitable numerical dissipation of the small scales and the general decay of TKE). Due to the significant loss of small-scale energy on the unstructured grid it is advised to leave the turbulent flow on the Cartesian grid for as long as possible. Since the RANS part of the grid did not show a significantly different energy spectrum than the LES part, it might be possible to simulate the flow upstream of the wing in RANS mode only. But that would, of course depend on the studied case.

The presented method showed the potential for studying the influence of realistic turbulent flows on a wing. In further studies cases with larger angles of attack should be investigated to e.g. simulate the influence of different meteorological scenarios on the stall of the wing.

Acknowledgements

The authors acknowledge the support of the "Deutsche Forschungsgemeinschaft DFG" (German Research Foundation) which funded this research in the framework of FOR1066. We thank the "High Performance Computing Center Stuttgart" (HLRS) for providing the resources to perform the simulations presented in this paper. We also would like to thank Axel Probst and Silvia Reuss from the Institute of Aerodynamics and Flow Technology of the German Aerospace Center for the support in setting up and running the DLR-TAU flow solver. Furthermore, we thank Prof. Rolf Radespiel for the helpful support.

References

Auerswald, T., **Bange, J.**, **Knopp, T.**, **Weinman, K.** and **Radespiel, R.**, **2012**: Large-Eddy Simulations of realistic atmospheric turbulence with the DLR-TAU-code initialized by in situ airborne measurements. *Computers & Fluids*, **66**, 121–129.

Bange, J., **Spieß, T.** and **van den Kroonenberg, A.**, **2007**: Characteristics of the Early-Morning Shallow Convective Boundary Layer from Helipod Flights during STINHO-2. *Theor. Appl. Climatol.*, **90**, 113–126.

Brandt, L., **Schlatter, P.** and **Henningson, D. S.**, **2004**: Transition in boundary layers subject to free-stream turbulence. *J. Fluid Mech.*, **517**, 167–198.

Cassel, K. W. and **Conlisk, A. T.**, **2014**: Unsteady separation in vortex-induced boundary layers. *Philosophical Transactions of the Royal Society of London A: Mathematical, Physical and Engineering Sciences*, **372**(2020).

Chung, M. K. and **Kim, S. K.**, **1995**: A nonlinear return-to-isotropy model with Reynolds number and anisotropy dependency. *Physics of Fluids*, **7**(6), 1425–1437.

Ghasemi, E., **McEligot, D. M.**, **Nolan, K. P.**, **Crepeau, J.**, **Tokuhiro, A.** and **Budwig, R. S.**, **2013**: Entropy generation in a transitional boundary layer region under the influence of freestream turbulence using transitional RANS models and DNS. *International Communications in Heat and Mass Transfer*, **41**, 10–16.

Heinrich, R., **2014**: Simulation of Interaction of Aircraft and Gust Using the TAU-Code. *New Results in Numerical and Experimental Fluid Mechanics IX, Notes on Numerical Fluid Mechanics and Multidisciplinary Design.*, **124**, 503–511.

Jameson, A., **1991**: Time Dependent Calculations Using Multigrid, with Applications to Unsteady Flows Past Airfoils and Wings. In: *AIAA 91-1596*.

Jones, K. D., **Dohring, C. M.**, and **Platzer, M. F.**, **1998**: Experimental and Computational Investigation of the Knoller-Betz Effect. *AIAA Journal*, **36**(7), 1240–1246.

Kelleners, P. and **Heinrich, R.**, **2015**: Simulation of Interaction of Aircraft with Gust and Resolved LES-Simulated Atmospheric Turbulence. In: R. Radespiel, R. Niehuis, N. Kroll and K. Behrends (editors), *Advances in Simulation of Wing and Nacelle Stall*, Springer, vol. 131.

Knigge, C., **Auerswald, T.**, **Raasch, S.** and **Bange, J.**, **2015**: Comparison of two methods simulating highly resolved atmospheric turbulence data for study of stall effects. *Computers & Fluids.*, **108**, 57–66.

Kok, J., **2009**: A High-Order Low-Dispersion Symmetry-Preserving Finite-Volume Method for Compressible Flow on Curvilinear Grids. *J. Comp. Phys.*, **228**(18), 6811–6832.

Langari, M. and **Yang, Z.**, **2013**: Numerical study of the primary instability in a separated boundary layer transition under elevated free-stream turbulence. *Physics of Fluids*, **25**(7), 074,106.

Lenschow, D. and **Stankov, B.**, **1986**: Length scales in the convective boundary layer. *J. Atmos. Sci.*, **43**, 1198–1209.

Li, Y. and **Meneveau, C.**, **2005**: Origin of Non-Gaussian Statistics in Hydrodynamic Turbulence. *Physical Review Letters*, **95**(16), 164,502–1–164,502–4.

Schwamborn, D., **Gerhold, T.** and **Heinrich, R.**, **2006**: The DLR TAU-Code: Recent Applications in Research and Industry. *ECCOMAS CFD 2006*.

Sreenivasan, K. R., **1999**: Fluid turbulence. *Rev. Modern Phys.*, **71**, 383–395.

Travin, A., **Shur, M.**, **Strelets, M.** and **Spalart, P. R.**, **2008**: Physical and numerical upgrades in the detached-eddy simulations of complex turbulent flows. *Advances in LES of Complex Flows*, 239–254.

A.4 An anisotropic synthetic turbulence method for Large-Eddy Simulation.

International Journal of Heat and Fluid Flow 62 (2016) 407–422

Contents lists available at ScienceDirect

International Journal of Heat and Fluid Flow

journal homepage: www.elsevier.com/locate/ijhff

An anisotropic synthetic turbulence method for Large-Eddy Simulation

Torsten Auerswald[a,b,*], Axel Probst[b], Jens Bange[a]

[a] Center for Applied Geoscience, University Tübingen, Germany
[b] Institute of Aerodynamics and Flow Technology, German Aerospace Center, Germany

ARTICLE INFO

Article history:
Received 4 November 2015
Revised 19 August 2016
Accepted 9 September 2016
Available online 28 September 2016

Keywords:
Synthetic turbulence
Large-Eddy Simulation
Channel flow

ABSTRACT

The method for generating anisotropic synthetic turbulence by Auerswald and Bange (2015) is extended to account for the integral length scales in *y*- and *z*-direction. This extension leads to more realistic turbulent structures. The method reproduces the given turbulence statistics very well and allows to set a number of turbulence parameters independently. In four Large-Eddy Simulations of a channel flow the synthetic turbulence is used as inflow boundary condition. The performance of the synthetic turbulence is tested and compared to the Direct Numerical Simulation (DNS) results by Moser et al. (1999). In these simulations the synthetic turbulence shows good performance in recovering realistic turbulence downstream in the channel. The skin-friction coefficient converges to the level of the DNS. The profiles of the Reynolds stresses are very similar in the LES and the DNS except for the profiles of R^+_{ww} where large deviations occur.

1. Introduction

Despite the progress in computer performance Large-Eddy Simulation (LES, e.g. Deardorff, 1970) is still very demanding for many applications. Since it resolves the large scales of the turbulence, LES needs finer grids than the Reynolds-Averaged Navier Stokes (RANS, e.g. Spalart and Allmaras, 1992) approach which models the whole turbulent spectrum in a statistical sense. In many applications only specific regions are of interest in terms of the unsteady turbulent characteristics. In these cases those parts are simulated using LES and the other parts using RANS. For example in simulations of the flow over a wing at high Reynolds numbers and high angles of attack, detaching eddies will be observed in the rear part of the wing. In Detached Eddy Simulations (DES, Spalart et al., 1997) only these detached flow parts with relevant eddies are simulated using LES, whereas the flow upstream and the boundary layer on the wing is simulated using RANS. In the interface region between the RANS and LES domains turbulence information is missing in the resolved flow coming from the RANS part. Therefore the flow entering the LES part contains no resolved turbulence which often leads to a delayed turbulence development in the LES part. To achieve a realistic turbulent flow in the LES domain as quickly as possible, synthetic turbulence which contains statistics from the RANS model can be injected into the LES part (e.g. Jarrin et al., 2006). However, the statistical information provided by RANS turbulence models is not complete. E.g. they lack information about higher order moments, the intermittency of the turbulent flow or exact spectral information. Though energy spectra can be derived from Reynolds stresses, information about the phase of the Fourier modes and the sign of the Fourier coefficient is not known. Furthermore, the turbulent pressure and density field is not known as well. As a consequence synthetic turbulence methods can only provide an estimate of the correct turbulent flow derived from the RANS statistics.

In previous studies different methods were proposed to generate synthetic turbulence. They are often tested in a simple channel flow simulation. To evaluate the performance of the synthetic turbulence methods, usually the turbulence statistics from a periodic LES are compared to the developed turbulence in the channel downstream of the synthetic turbulent inlet. One class of methods are the Fourier approaches. They are based on the work by Kraichnan (1970) in which the superposition of Fourier modes with Fourier coefficients chosen to meet a given energy spectrum result in a synthetic turbulent field. Recent examples for this approach are the work by Batten et al. (2004), Batten et al. (2012), Adamian and Travin (2011) and Shur et al. (2014) (which contains an aeroacoustic extension of Adamian and Travin, 2011). In these studies the Cholesky decomposition is used to meet the given shear stresses by applying a transformation matrix to the velocity field. During this process the 1D statistics (e.g. length scales and energy spectra) in lateral and especially vertical direction are changed, and therefore control over the statistics in each direction is limited. Nevertheless, results in the simulation of a channel flow,

---

[*] Corresponding author.
E-mail address: torsten.auerswald@uni-tuebingen.de (T. Auerswald).

http://dx.doi.org/10.1016/j.ijheatfluidflow.2016.09.002

especially for the latter method, are very close to the periodic LES. A different approach is the synthetic eddy method (SEM) by Jarrin et al. (2006). This method is based on the superposition of eddies which are defined by geometrical shape functions for the velocity field. Appropriate length scales can be achieved by choosing the size of the individual eddies. This method is very efficient and allows for control over the coherent structures of the turbulent field. However, since it realises the correct shear stresses by applying the Cholesky decomposition, the same disadvantages as in the previously mentioned methods are present. Additionally, it does not allow to prescribe an energy spectrum. Based on the SEM Poletto et al. (2011) developed the divergence-free synthetic eddy method (DF-SEM). Like the SEM it uses shape functions to represent single eddies geometrically. But where the SEM applied the shape function to the velocity field Poletto et al. (2011) apply it to the vorticity field. When transforming the vorticity field to the velocity field, the divergence term is neglected resulting in a divergence-free velocity field. Correct Reynolds stresses are achieved by a proper scaling of the intensities of the eddies. This avoids the disadvantages that come with the Cholesky decomposition. However this method also does not provide control over the energy spectra. As a consequence in both the turbulent fields from the SEM and DF-SEM, the spectra close to the wall are deviating from the spectra observed in a periodic LES. Nevertheless, these two methods also achieve good results in the simulation of a channel flow compared to the periodic LES.

The motivation for this work was to improve the method presented in Auerswald and Bange (2015) and to develop an alternative to the above mentioned methods, which allows for more flexibility when prescribing inflow conditions while at the same time being cost efficient. Another alternative would be Fourier methods based on the work of Smirnov et al. (2001). They require the calculation of the Eigenvectors of the Reynolds stress tensor and orthogonal transformations of the velocity vectors in order to reproduce the correct Reynolds stresses, which can cause higher computational costs.

In case of a Reynolds stress model (RSM, Launder et al., 1975) the turbulence statistics provided by RANS are the components of the Reynolds stress tensor and the dissipation rate. In this work the turbulence generator from Auerswald and Bange (2015) is used to generate a time series of 2D-planes with synthetic turbulence using the statistics an RSM would provide. In order to avoid the disadvantages of the Cholesky decomposition and gain more control over the statistics, the method by Auerswald and Bange (2015) uses an alternative approach to provide correct shear stresses without changing the other turbulence statistics. To be able to evaluate the quality of the generated turbulence the input statistics are taken from a DNS of a channel flow (Moser et al., 1999) instead of a RANS simulation. The advantage of the DNS data is that it provides high quality statistics for the given case. From the DNS statistics, synthetic turbulence is generated which is then used as inflow boundary condition for different LES of a channel flow. The resulting turbulent flow fields in the channel are compared to the DNS results and the results of a periodic LES. For the simulations of the channel flow the numerical solver DLR-TAU (Schwamborn et al., 2006), developed at the German Aerospace Center, is used. In Section 2.1 an overview over the turbulence-generating method from Auerswald and Bange (2015) is given. Section 2.2 explains the extension to the turbulence generator which allows to generate synthetic turbulence with more realistic lengths scales in y- and z-direction. With this new method it is therefore possible to prescribe the 1D energy spectrum in x-direction, the length scales in x, y and z direction for u,v and w and the profiles of the normal stresses and shear stresses. The numerical method and simulation scenario are described in Section 2.3. In Sections 3.2 and 3.3 results from the turbulence generator without and with extension are shown, and Section 3.4 presents first results from an LES of a channel flow using the synthetic turbulence generator with extension and compares it to the data from the DNS and periodic LES. To evaluate the performance of the new method the results are also compared to the SEM and DF-SEM.

2. Method

2.1. The original synthetic turbulence generator

To generate synthetic turbulence the method from Auerswald and Bange (2015) is applied. In this method the Reynolds stress tensor and the dissipation rate (which can be provided by a RANS simulation or a DNS) serve as input parameters. First, 1D power spectra $S_i(k_x(y), y, z)$ $(i = 1, 2, 3)$ are calculated for all three velocity components on a $y - z$-plane by applying the model spectrum formulation from Kamruzzaman et al. (2012) for the wavenumbers:

$$k_x(y) = \frac{2\pi i}{N_t \Delta t U(y)}, \tag{1}$$

where i is an integer in the interval $[-N_t/2, N_t/2]$, N_t is the number of timesteps, Δt the timestep size and $U(y)$ the mean velocity in x-direction. In the following $k_x(y)$ will be abbreviated by k_x.

The model spectrum takes the normal stresses and the dissipation rate as input variables. It is designed in such a way that the integral over the spectrum is equal to the normal stress for the respective component of the velocity. The shape of the spectrum takes into account the integral length scale, estimated from the normal stress and the dissipation rate (the exact equation is provided in Eq. (22)), by adjusting the wavenumber at which the transition zone between the production range and the inertial subrange is located.

From the 1D power spectra $S_i(k_x, y, z)$, the spectral velocities can be calculated:

$$\tilde{u}_i(k_x, y, z) = a_i(k_x, y, z) \cdot \frac{1}{2}\sqrt{(S_i(k_x, y, z)) \cdot \Delta k_x}, \tag{2}$$

where Δk_x is the wave number interval in x-direction and $a_i(k_x, y, z)$ are the signs of the spectral velocities for each wave number k_x and position y and z. They can take the values -1 or 1. Applying an inverse Fourier Transform (FT) to Eq. (2) results in a time series (because of Eq. (1)) of 2D-flow fields which contains the prescribed 1D-spectra. It also meets the normal stresses used to calculate the spectra and different integral length scales for the three velocity components calculated from the normal stresses and the dissipation rate (see Kamruzzaman et al., 2012 for details). By properly choosing the signs $a_i(k_x, y, z)$ of the spectral velocities before applying the inverse FT also the shear stresses can be prescribed without changing the other statistics.

The Reynolds stress tensor is defined as:

$$\tau_{ij} = \rho R_{ij}(0), \tag{3}$$

where $R_{ij}(0)$ is the one-point covariance in x-direction of the velocity components and ρ the density of the fluid. Since the inverse FT of the cospectrum is equal to the covariance function the one-point covariance can be written as:

$$R_{ij}(0) = \sum_{n=0}^{N} \tilde{u}_{ni}^{*}\tilde{u}_{nj}, \tag{4}$$

where n is the index for the wave numbers and N the total number of wave numbers that can be resolved with the given grid. That means that the signs $a_i(k_x, y, z)$ control the contribution of the spectral velocities to the total covariance at each wavenumber. If $a_i = a_j$ at all points (k_x, y, z) the covariance will be at a maximum and if $a_i = -a_j$ at all points (k_x, y, z) the covariance will be at a minimum. If a_i and a_j are chosen randomly by independent random numbers at all points, the covariance will be zero. That means if a_i is chosen properly all covariances between the maximum and the minimum can be met.

The probability $P(A_{ij})$ that the signs of two spectral velocities are equal $(a_i = a_j)$ at a certain wave number in the $y-z$-plane is:

$$P(A_{ij}) = \frac{\tau_{ij}(y,z) - \hat{\tau}_{ij}(k_x,y,z)}{\tau_{ij,\max}(y,z) - \hat{\tau}_{ij,\max}(k_x,y,z)}, \tag{5}$$

where A_{ij} represents the event that $a_i = a_j$, $\hat{\tau}_{ij}(k_x,y,z)$ is the Reynolds stress after summation over the cospectrum from $k_{x,\min}$ to k_x. $\tau_{ij,\max}(y,z)$ is the maximum Reynolds stress that can be constructed with the given spectral velocities and $\hat{\tau}_{ij,\max}(k_x,y,z)$ is the maximum Reynolds stress that can be constructed in the interval $(k_{x,\min}, k_x)$. $k_{x,\min}$ is the minimum wave number that can be resolved by the given grid.

The following combinations of events are possible:

$$A_{12} \cap A_{23} \cap A_{13} \tag{6}$$

$$A_{12} \cap A_{23}^r \cap A_{13}^r \tag{7}$$

$$A_{12}^r \cap A_{23} \cap A_{13}^r \tag{8}$$

$$A_{12}^r \cap A_{23}^r \cap A_{13} \tag{9}$$

$$A_{12}^r \cap A_{23}^r \cap A_{13}^r, \tag{10}$$

For the event A_{ij} the sign a_j will be chosen to be equal to a_i. In the case of A_{ij}^r, a_j will be chosen randomly in order for it to not contribute to the covariance statistically.

The following Eqs. (11)–(13) represent these five combinations. Independent random numbers are used to determine the signs of the spectral velocities. The random numbers to determine if the spectral velocity component is going to contribute to the covariance are called r_{12}, r_{13} and r_{23} for the covariances R_{12}, R_{13} and R_{23}, respectively. If the spectral velocity component is not going to contribute to the covariance, the random numbers r_1, r_2 and r_3 are used to determine the sign for u, v and w, respectively. First the sign of $u(k_x, y, z)$ is chosen randomly:

$$a_1(k_x,y,z) = \begin{cases} 1 & \text{, if } r_1 < 0.5, \\ -1 & \text{, if } r_1 \geq 0.5. \end{cases} \tag{11}$$

Then the sign for $v(k_x, y, z)$ is chosen by:

$$a_2(k_x,y,z) = \begin{cases} a_1(k_x,y,z) & \text{, if } r_{12} < P(A_{12}) \text{ and } R_{12} > 0, \\ -a_1(k_x,y,z) & \text{, if } r_{12} < P(A_{12}) \text{ and } R_{12} \leq 0. \\ 1 & \text{, if } r_{12} > P(A_{12}) \text{ and } r_2 < 0.5, \\ -1 & \text{, if } r_{12} > P(A_{12}) \text{ and } r_2 \geq 0.5. \end{cases} \tag{12}$$

And finally the sign for $w(k_x, y, z)$ is chosen by:

$$a_3(k_x,y,z) = \begin{cases} a_2(k_x,y,z) & , r_{12} < P(A_{12}) \text{ and } (r_{23} < P(A_{23}) \text{ or } r_{13} < P(A_{13})) \text{ and } R_{23} > 0, \\ -a_2(k_x,y,z) & , r_{12} < P(A_{12}) \text{ and } (r_{23} < P(A_{23}) \text{ or } r_{13} < P(A_{13})) \text{ and } R_{23} \leq 0, \\ 1 & , r_{12} < P(A_{12}) \text{ and } (r_{23} > P(A_{23}) \text{ and } r_{13} > P(A_{13})) \text{ and } r_3 < 0.5, \\ -1 & , r_{12} < P(A_{12}) \text{ and } (r_{23} > P(A_{23}) \text{ and } r_{13} > P(A_{13})) \text{ and } r_3 \geq 0.5, \\ a_2(k_x,y,z) & , r_{12} > P(A_{12}) \text{ and } r_{23} < P(A_{23}) \text{ and } R_{23} > 0, \\ -a_2(k_x,y,z) & , r_{12} > P(A_{12}) \text{ and } r_{23} < P(A_{23}) \text{ and } R_{23} \leq 0, \\ a_1(k_x,y,z) & , r_{12} > P(A_{12}) \text{ and } r_{23} > P(A_{23}) \text{ and } r_{13} < P(A_{13}) \text{ and } R_{23} > 0, \\ -a_1(k_x,y,z) & , r_{12} > P(A_{12}) \text{ and } r_{23} > P(A_{23}) \text{ and } r_{13} < P(A_{13}) \text{ and } R_{23} \leq 0, \\ 1 & , r_{12} > P(A_{12}) \text{ and } r_{23} > P(A_{23}) \text{ and } r_{13} > P(A_{13}) \text{ and } r_3 < 0.5, \\ -1 & , r_{12} > P(A_{12}) \text{ and } r_{23} > P(A_{23}) \text{ and } r_{13} > P(A_{13}) \text{ and } r_3 \geq 0.5, \end{cases} \tag{13}$$

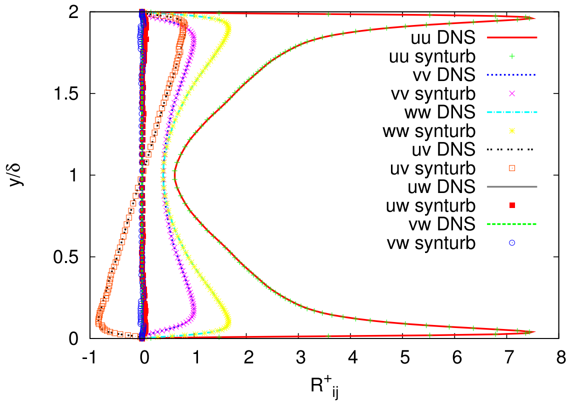

Fig. 1. Vertical profiles of the normalised covariances R_{ij} in x-direction averaged over z from the DNS data (lines) and from the synthetic turbulence (symbols) (For interpretation of the references to colour in this figure legend, the reader is referred to the web version of this article.).

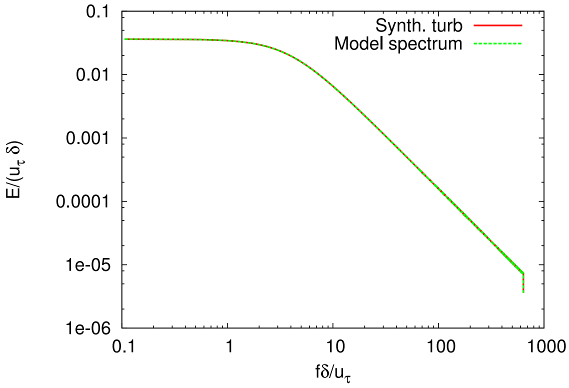

Fig. 2. Normalised 1D-spectrum of u from synthetic turbulence (red, line) and from the model spectrum (green, dashed) at a height of $y/\delta = 0.47$, averaged over z. (For interpretation of the references to colour in this figure legend, the reader is referred to the web version of this article.)

To generate a turbulent velocity field the signs from Eqs. (11) to (13) have to be assigned to the spectral velocities and an inverse FT has to be performed. The resulting turbulence exhibits the given normal stresses, shear stresses and 1D-spectra for each velocity component in x-direction. It also matches the estimated integral length scales in x-direction, since the model spectrum from Kamruzzaman et al. (2012), used to generate the turbulent field, considers the integral length scales by adjusting the wavenumber at which the transition between the energy producing range and the inertial subrange is located. Results from this method are shown in Section 3.2.

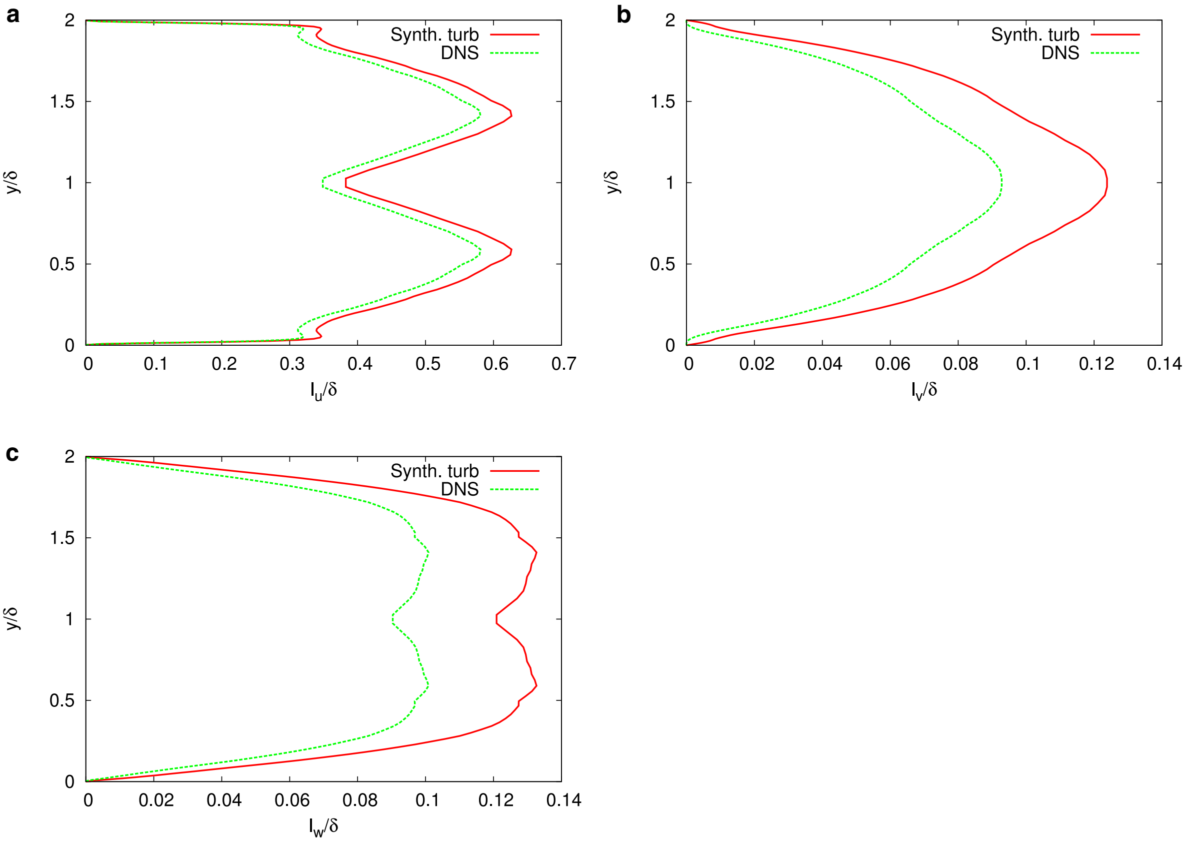

Fig. 3. Vertical profiles of the normalised integral length scales of (a) u, (b) v and (c) w in x-direction calculated from the synthetic turbulence (red, line) and estimated from the DNS data (green, dashed). (For interpretation of the references to colour in this figure legend, the reader is referred to the web version of this article.)

2.2. Modifications to the turbulence generator

Even though the turbulence generator presented in the previous section represents the input statistics very well (see Section 3.2), modifications for the application in the LES of the channel flow are necessary. So far only the statistics in x-direction are considered. At each point in the y-z-plane synthetic turbulence is generated independently. That leads to very small-scale turbulence in y- and z-direction which basically has a length scale of the size of the grid spacing in y- and z-direction. Such a turbulent field would dissipate very quickly in a numerical simulation. Therefore, in this section, an extension to the turbulence generator is presented which gives some control over the size of the eddies in y- and z-direction. The idea is to force larger length scales in y- and z-direction by not generating synthetic turbulence at each point of the y-z-plane but skipping points until the grid spacing is about the same size like the length scale in that direction. On the points where no synthetic turbulence is generated the values for the velocity components are calculated by interpolation. To distinguish the points on which turbulence is generated from the points which contain the complete turbulent field, the first ones will be called to be on the 'coarse grid' and the latter ones to be on the 'fine grid' (even though there is no need to generate a coarse grid, since points on the grid in use are simply skipped).

The simplest way to interpolate is a linear interpolation:

$$u_{i,j,k_1} = \tilde{u}_{i,j,k_2} + (z_{k_1} - z_{k_2}) \frac{\tilde{u}_{i,j,k_2+1} - \tilde{u}_{i,j,k_2}}{z_{k_2+1} - z_{k_2}}, \tag{14}$$

where u is the interpolated value on the fine grid, $\tilde{u}$ is the value on the coarse grid, z_{k_1} is the z-coordinate on the fine grid and z_{k_2} is the z-coordinate on the coarse grid. This equation interpolates $\tilde{u}$ linearly in z-direction. By inserting this equation into the equation for the variance:

$$R_{11_{i,j,k_1}} = \frac{1}{N} \sum_{n=0}^{N} \left(\tilde{u}_{i,j,k_2} + (z_{k_1} - z_{k_2}) \frac{\tilde{u}_{i,j,k_2+1} - \tilde{u}_{i,j,k_2}}{z_{k_2+1} - z_{k_2}} \right)^2, \tag{15}$$

one can see that the Reynolds stresses will not be linear in the interpolation intervals. This causes deviations from the prescribed Reynolds stresses which also affect the 1D-spectra and length scales (see Section 3.3). The normal stresses will be interpolated linearly if the squares of the velocities are interpolated linearly instead of the velocities themselves:

$$u_{i,j,k_1} = \sqrt{\tilde{u}^2_{i,j,k_2} + (z_{k_1} - z_{k_2}) \frac{\tilde{u}^2_{i,j,k_2+1} - \tilde{u}^2_{i,j,k_2}}{z_{k_2+1} - z_{k_2}}}. \tag{16}$$

The variance then takes the form:

$$R_{11_{i,j,k_1}} = \frac{1}{N} \sum_{n=0}^{N} \sqrt{\tilde{u}^2_{i,j,k_2} + (z_{k_1} - z_{k_2}) \frac{\tilde{u}^2_{i,j,k_2+1} - \tilde{u}^2_{i,j,k_2}}{z_{k_2+1} - z_{k_2}}}^{\,2}, \tag{17}$$

which results in the linear interpolation equation for the variance:

$$R_{11_{i,j,k_1}} = \tilde{R}_{11_{i,j,k_2}} + (z_{k_1} - z_{k_2}) \frac{\tilde{R}_{11_{i,j,k_2+1}} - \tilde{R}_{11_{i,j,k_2}}}{z_{k_2+1} - z_{k_2}}. \tag{18}$$

In order to not only get positive interpolated values, signs have to be assigned to the interpolated velocity. A simple way is to just assign the sign of the next velocity value from the coarse grid to the interpolated velocity. In any case, by interpolating the squares of the velocity in this way, there will be discontinuities in the

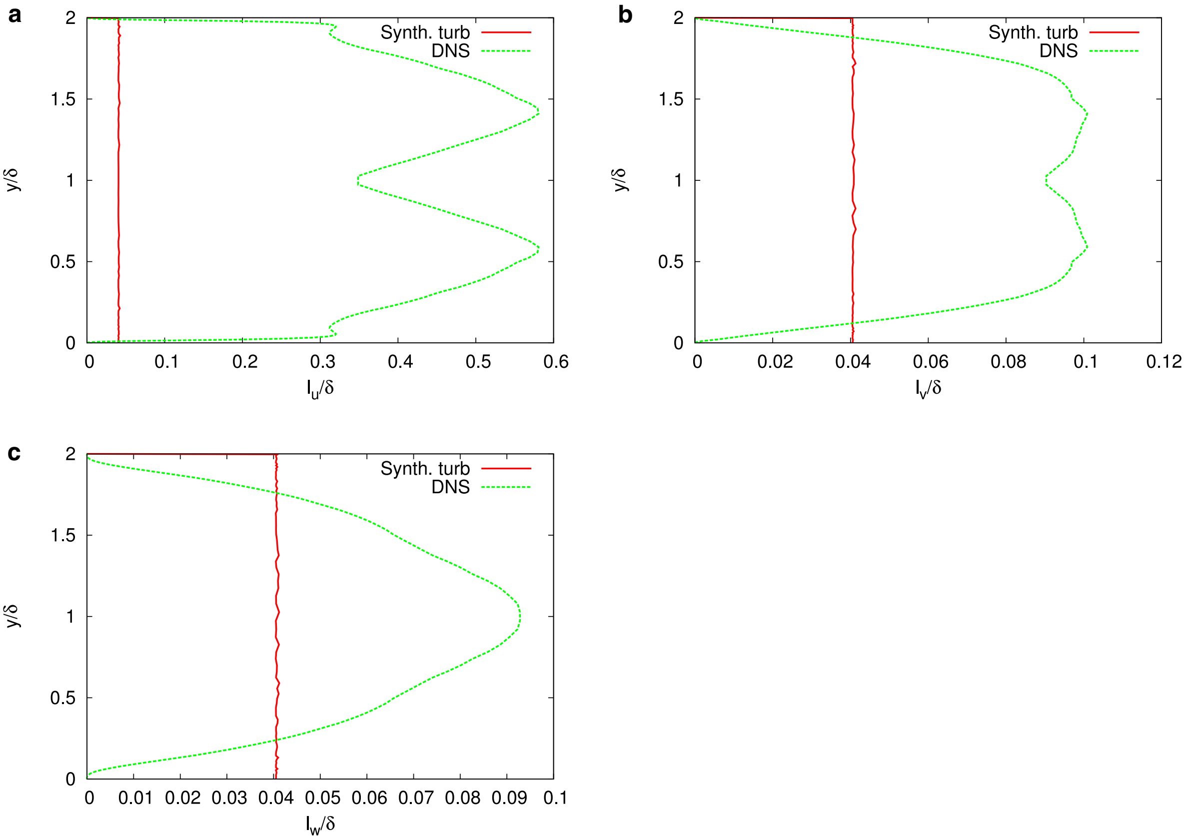

Fig. 4. Vertical profiles of the normalised integral length scales of (a) u, (b) v and (c) w in *z*-direction calculated from the synthetic turbulence (red, line) and estimated from the DNS data (green, dashed). (For interpretation of the references to colour in this figure legend, the reader is referred to the web version of this article.)

interpolated field when the velocities are changing sign. To avoid these discontinuities and to get a smoother interpolation the signs of the velocities on the coarse grid can already be assigned to the squares of the velocities on the coarse grid:

$$u_{i,j,k_1} = s \cdot \sqrt{\left| \underbrace{\frac{\tilde{u}_{i,j,k_2}}{\left|\tilde{u}_{i,j,k_2}\right|}\tilde{u}^2_{i,j,k_2} + (z_{k_1} - z_{k_2})\frac{\frac{\tilde{u}_{i,j,k_2+1}}{\left|\tilde{u}_{i,j,k_2+1}\right|}\tilde{u}^2_{i,j,k_2+1} - \frac{\tilde{u}_{i,j,k_2}}{\left|\tilde{u}_{i,j,k_2}\right|}\tilde{u}^2_{i,j,k_2}}{z_{k_2+1} - z_{k_2}}}_{T} \right|}, \tag{19}$$

where s is the sign of the term *T*. Now when the velocities are changing signs the interpolation will be smoother but in those cases there will be deviations from the linear interpolation of the Reynolds stresses. The more of these cases occur the larger the deviation will be.

Results for all three interpolation types (Eqs. (14), (16) and (19)) are shown in Section 3.3. The interpolation is applied first in the spanwise *z*-direction. Then the interpolated field is interpolated once more in the wall normal *y*-direction. To prescribe different length scales for *u*, *v* and *w* in *y*- and *z*-direction, the number of grid points to skip and interpolate, can be determined independently for each velocity component. For simplicity, in this study, the length scales of the velocity components were set to be equal for all velocity components in *y*- and *z*-direction. The smaller the prescribed length scales are, the more similar the turbulent field becomes to the field generated by the method presented in Section 2.1

The numerical costs for this method are very small compared to the costs for the LES of the channel flow. Per timestep generated with this method about 0.025 s is needed on one core of a regular Intel core i3-530 CPU with 2.93 GHz. This is orders of magnitude less than the computation of one physical timestep in the LES of the channel flow. On 12 Intel Haswell CPU's (144 cores in total, 2.5 GHz), computing a single timestep takes 25 s. That results in roughly 3600 s per timestep on a single core. Ignoring the differences between the different CPUs used and the fact that the solver performance scales only approximately linearly on multiple cores, the computational costs of generating the synthetic turbulence for each timestep is roughly 0.001 % of a timestep. For the test case considered in this work, the present SEM implementation in TAU requires about 1–2% of a timestep. In both cases these computational costs are very small compared to the overall costs for a timestep. However, in more complex simulations with multiple synthetic-turbulence planes or when using less sub-iterations per timestep due to a finer temporal resolution, the difference in the costs for generating the synthetic turbulence could lead to a more significant advantage of the present method over the SEM.

2.3. Numerical method

To analyse the performance of the synthetic-turbulence approach in the framework of LES, the method has been implemented in the unstructured flow solver DLR-TAU (Schwamborn et al., 2006). This section briefly outlines the applied numerical algorithms and the sub-grid model of turbulence.

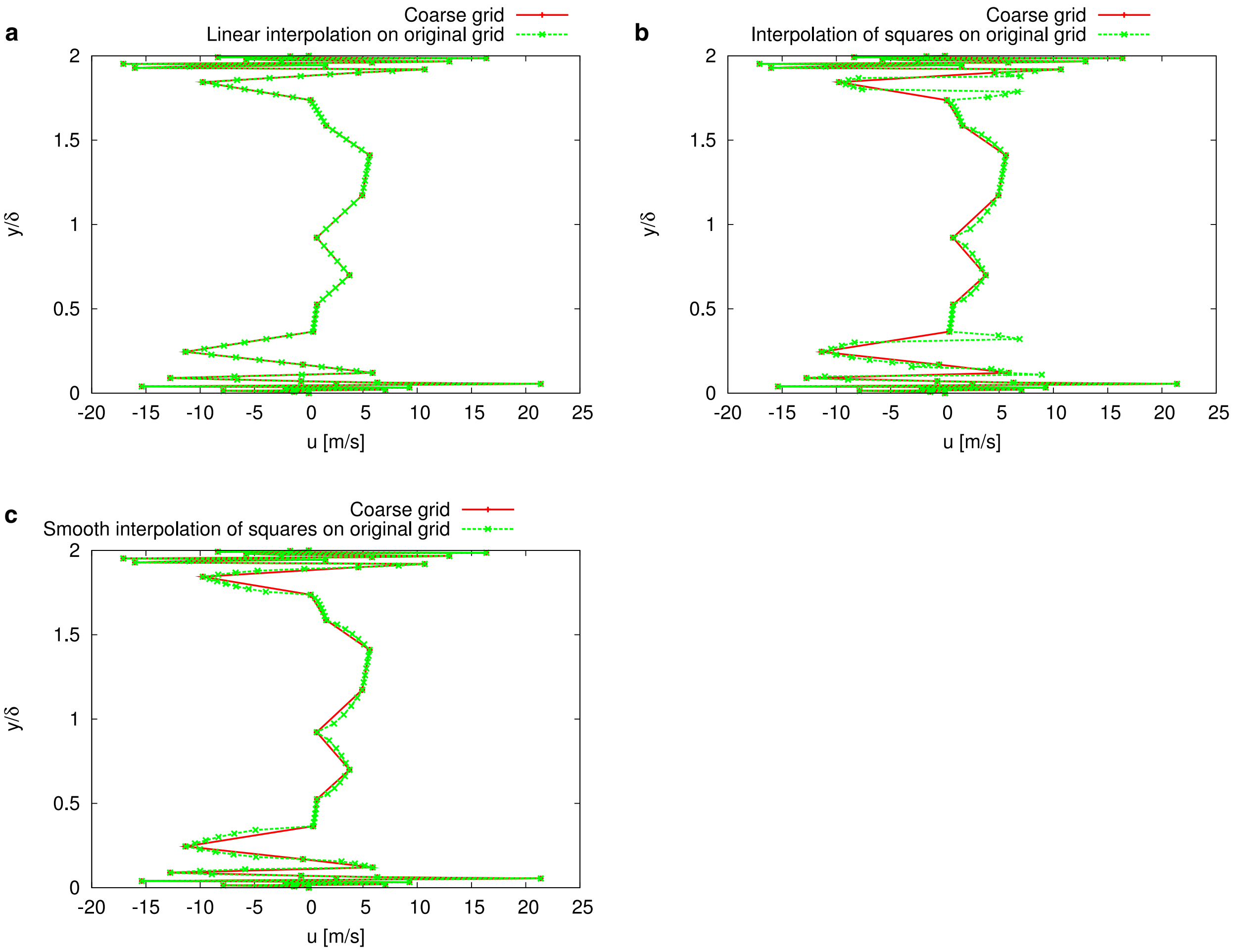

Fig. 5. Interpolation in y-direction from the coarse grid (red line) onto the fine grid (green, dashed) for u: (a) linear, (b) squares, (c) smooth squares. (For interpretation of the references to colour in this figure legend, the reader is referred to the web version of this article.)

2.3.1. *The DLR-TAU flow solver*

The DLR-TAU code applies the finite-volume approach to numerically solve the compressible (Reynolds-averaged or LES-filtered) Navier–Stokes equations on an unstructured grid metric.

For scale-resolving simulations of subsonic flows a 2nd-order central discretization of the skew-symmetric convection form by Kok (2009) is used which preserves kinetic energy locally and globally on curvilinear grids. The viscous fluxes are discretised using central differences.

While the skew-symmetric discretization is designed to be non-dissipative, a small amount of artificial dissipation is usually required to ensure stability on highly-stretched or irregularly-shaped grid cells. In this work, a 4th-order matrix-valued dissipation flux is added to the five mean-flow equations which is computed at each face ij between two control volumes i and j:

$$\mathbf{d}_{ij}^{(4)} = \kappa^{(4)} \cdot |\mathbf{PA}|_{ij} \cdot \phi_{ij} \cdot \left\{ \nabla^2 \mathbf{w}_i - \nabla^2 \mathbf{w}_j \right\} \quad . \tag{20}$$

The term $|\mathbf{PA}|_{ij}$ is the matrix-dissipation operator (Swanson and Turkel, 1992) which includes the low Mach-number preconditioning (LMP) matrix $\mathbf{P}$, while $\mathbf{w}_i$, $\mathbf{w}_j$ are the vectors of conservative main-flow variables. The term $\kappa^{(4)}$ is a global scaling factor. The LMP matrix is introduced to reduce the disparity of eigenvalues of the compressible equations at low Mach numbers, thus providing almost Ma-independent accuracy. To avoid singularities of $\mathbf{P}$ in stagnation regions, a lower bound for the so-called 'artificial speed of sound' is included, which is weighted by a global cut-off parameter K_{LMP} (cf. Radespiel et al., 1995 for details). The cell-stretching coefficient ϕ_{ij} is used to increase dissipation in the direction of local cell stretching in order to stabilise computations on grid cells with a very high aspect ratio (Blazek, 2005).

In this work, the parameters in Eq. (20) are chosen according to Probst and Reuß (2015) who determined suitable settings for wall-resolved large-eddy simulations of the plane channel flow: $\kappa^{(4)} = 1/1024$, $K_{\text{LMP}} = 0.3$, and $\phi_{ij} = 1$.

The time discretization in the DLR-TAU code uses a 2nd-order backward differencing formula, BDF(2), together with dual-time stepping (Jameson, 1991). Within each time step, the nonlinear problems are solved using a semi-implicit lower-upper symmetric Gauss-Seidel (LU-SGS) method which is optionally combined with a multigrid scheme of full approximation type and residual smoothing for convergence acceleration.

2.3.2. *The WALE model for large-eddy simulation*

In LES only the large scales of the turbulent energy spectrum are resolved, whereas the smaller dissipative eddies below the local grid spacing Δ require appropriate modelling. In the present work this is accomplished by the Wall-Adapting Local Eddy-viscosity model (WALE, Ducros et al., 1998) which employs the Boussinesq approach to compute the modelled sub-grid stresses

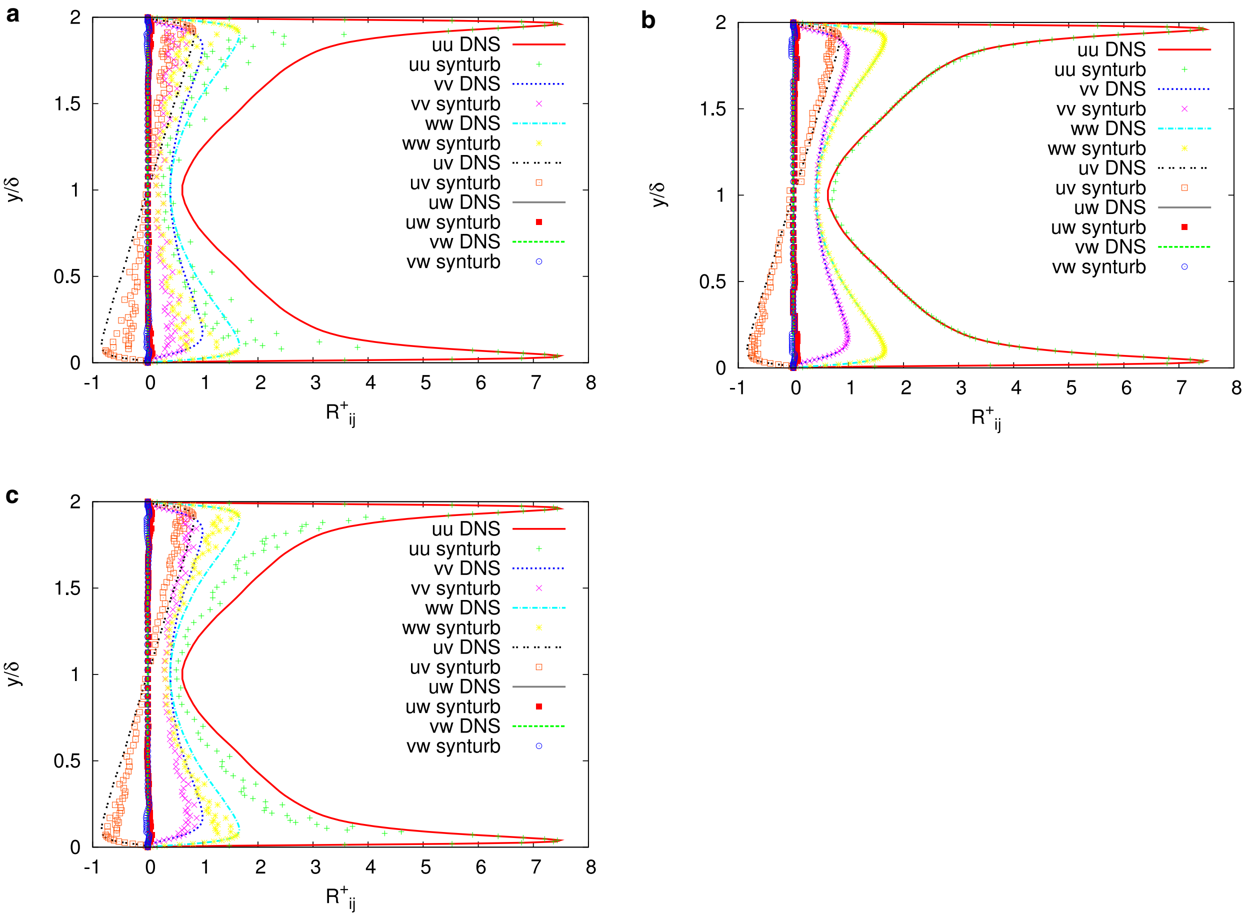

Fig. 6. Vertical profiles of the normalised covariances R_{ij} in x-direction averaged over z from the DNS data (lines) and from the synthetic turbulence (symbols). Results for the different interpolations: (a) linear, (b) square and (c) smooth square. (For interpretation of the references to colour in this figure legend, the reader is referred to the web version of this article.)

from a scalar eddy viscosity μ_t:

$$\mu_t = \rho \cdot (C_{\mathrm{WALE}} \cdot \Delta)^2 \cdot S^*, \quad \text{with:} \quad \Delta_{vol} = (\Delta x \cdot \Delta y \cdot \Delta z)^{1/3}. \qquad (21)$$

A rather complex form of the velocity-gradient operator S^* ensures realistic asymptotic behaviour of the sub-grid viscosity at solid walls (see Ducros et al., 1998 for details). For the model constant C_{WALE} the commonly accepted calibration value for wall-bounded turbulence is used: $C_{\mathrm{WALE}} = 0.325$.

3. Channel flow simulations at $\mathrm{Re}_\tau \approx 395$

3.1. Numerical setup

To assess the original and the extended synthetic-turbulence generators we consider the plane channel flow at $\mathrm{Re}_\tau = u_\tau \cdot \delta/\nu \approx 395$, where u_τ is the friction velocity, δ the channel half-height and ν the kinematic viscosity. While in Sections 3.2 and 3.3 the properties of the synthetic turbulence in the inflow plane are analyzed a priori, Section 3.4 provides results from LES simulations of the whole channel with the DLR-TAU code.

In these simulations the synthetic velocity fluctuations are prescribed via a time-dependent Dirichlet inflow boundary condition. The required input statistics for the synthetic turbulence are derived from the corresponding DNS results of this flow by Moser et al. (1999). The computational domain comprises a rectangular box of height 2δ, a length of 32δ and a width of $\pi \cdot \delta$. At the outflow a characteristic constant-pressure condition is applied, while in spanwise direction periodic boundary conditions are used. A sufficiently low bulk Mach number of $\mathrm{Ma} = 0.15$ is chosen to avoid any compressibility effects.

The spatial and temporal resolution follows common practice for wall-resolved LES, i.e. using a hexahedral grid with normalised spacings of $\Delta x^+ = x \cdot u_\tau/\nu \approx 32$, $\Delta y(1)^+ \approx 1$, $\Delta z^+ \approx 15$ and a normalised time step of $\Delta t^+ = \Delta t \cdot u_\tau^2/\nu \approx 0.4$. The overall simulation times for the LES comprise around 5.6 convective time units (1 CTU $= 32\delta/U_{\mathrm{bulk}}$ is the characteristic time it takes the flow to travel through the channel at bulk velocity U_{bulk}), which are divided into an initial transient phase of 3 CTU and another 2.6 CTU for obtaining temporal statistics.

The channel flow at this Reynolds number is often used for testing synthetic turbulence (e.g. Jarrin et al., 2009; Keating and Piomelli, 2004). Since the flow has a low Reynolds number, it can be simulated using wall-resolved LES. Therefore the influence of turbulence modelling on the results is rather small and it is easier to isolate the effects of the synthetic turbulence. Furthermore, for this Reynolds number DNS results are available for comparison.

3.2. Results from the original turbulence generator

In this section results for the synthetic turbulence at the inlet plane of the channel generated by the turbulence generator as described in Section 2.1 and by Auerswald and Bange (2015) are

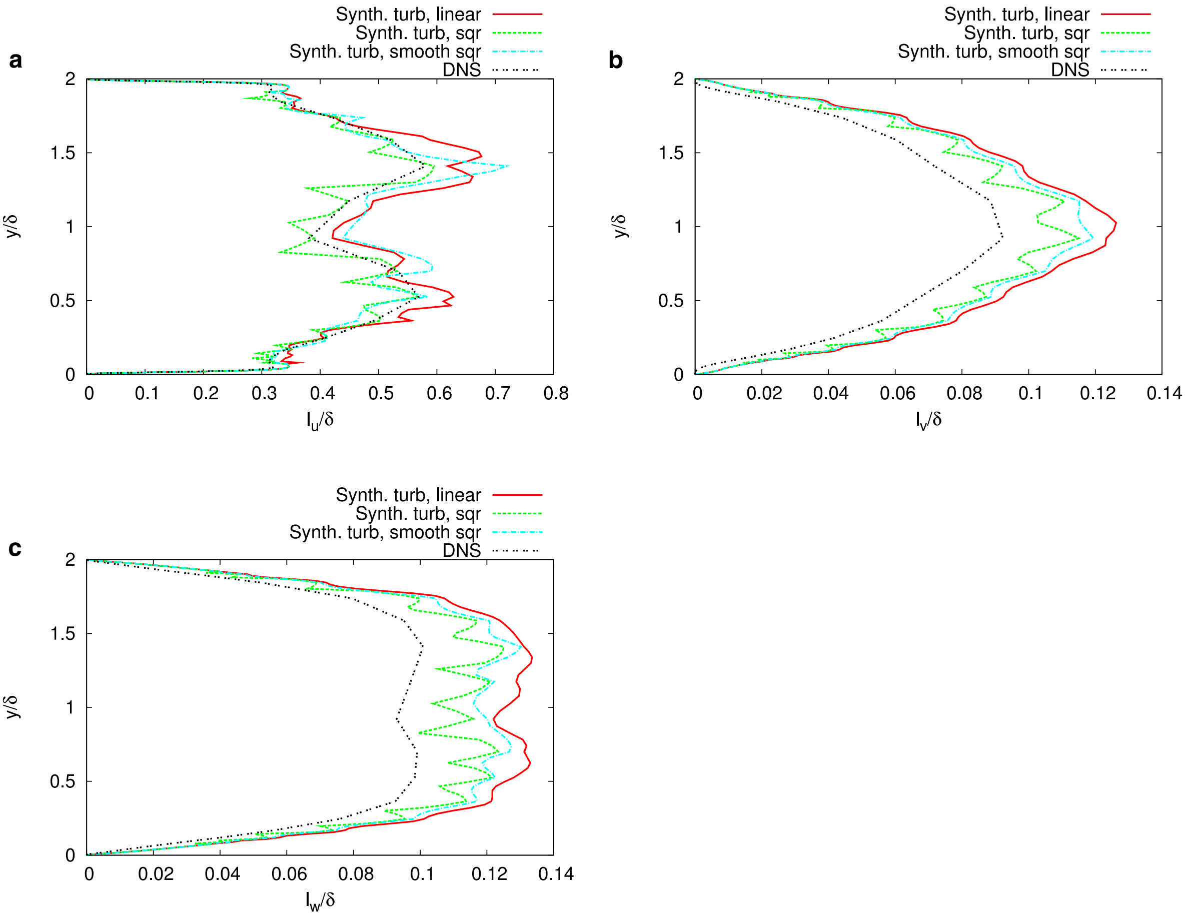

Fig. 7. Vertical profiles of the normalised integral length scales of (a) u, (b) v and (c) w in x-direction estimated from the DNS data (black, double dotted) and calculated from the synthetic turbulence with linear interpolation (red, line), square (green, dashed) and smooth square (blue, dot-dashed). (For interpretation of the references to colour in this figure legend, the reader is referred to the web version of this article.)

presented. The input data is taken from the DNS of a channel flow from Moser et al. (1999) at $\mathrm{Re}_\tau = 395$. In order to produce correct shear stresses, the turbulence generator needs to produce a minimum number of timesteps which results in enough wavenumbers at which the signs of the spectral velocities can be determined. In the case presented in this paper it was found that already with 500 timesteps satisfying results were achieved. However since the LES of the channel flow, presented later, comprises 12,000 timesteps, all results presented here are based on 12,000 timesteps of synthetic turbulence. That number corresponds to 6000 Fourier modes for the model spectrum.

Fig. 1 shows the covariances (which are proportional to the Reynolds stresses, see Eq. (3)) in x-direction averaged over z and normalised by u_τ^2. The lines depict the covariances from the DNS data. The covariances calculated from the synthetic turbulence are depicted by symbols. Some of the lines can not be seen because of the very good match with the symbols. In all components the prescribed covariances and the covariances from the synthetic turbulence are in almost perfect agreement.

In Fig. 2 the model spectrum S_i of u at a height of y/δ=0.47 calculated from the Reynolds stresses from the DNS data (green, dashed) is shown exemplarily. Like all other spectra for the three velocity components at all heights, it is in perfect match with the 1D-spectrum in x-direction calculated from the generated synthetic turbulence. Figs. 3 and 4 show the vertical profiles of the integral length scales of the velocity components calculated in x- and z-direction, respectively. The red line shows the integral length scale estimated from the DNS data. For the estimation the variances and the dissipation rate are used as suggested in e.g. Kamruzzaman et al. (2012):

$$l_u = \pi C_1 \frac{R_{11}^{3/2}}{\epsilon}, l_v = \pi C_1 \frac{R_{22}^{3/2}}{\epsilon}, l_w = \pi C_1 \frac{R_{33}^{3/2}}{\epsilon}, \tag{22}$$

where C_1 is a Reynolds number dependent factor. Following Kamruzzaman et al. (2012) it is set to 0.23. R_{ii} are the variances and ϵ is the dissipation rate both taken from the DNS data set. The integral length scale from the synthetic turbulence is calculated by integrating the autocorrelation function from lag zero to the first zero crossing of the autocorrelation function. The autocorrelation function is averaged over z. Since the integral length scales are derived from two different methods a perfect match is not expected. Nevertheless Fig. 3 shows a good agreement between the integral length scales from the DNS data and the synthetic turbulence. For all three velocity components the integral length scales from the synthetic turbulence are only slightly larger than the estimated integral length scales from the DNS. Also the shape of the vertical profiles is very similar.

However, the integral length scales in z-direction show a very different picture (see Fig. 4). Because of a lack of control over the statistics in z-direction the integral length scales in that direction are equal to the grid spacing in z-direction of 0.04δ (red line).

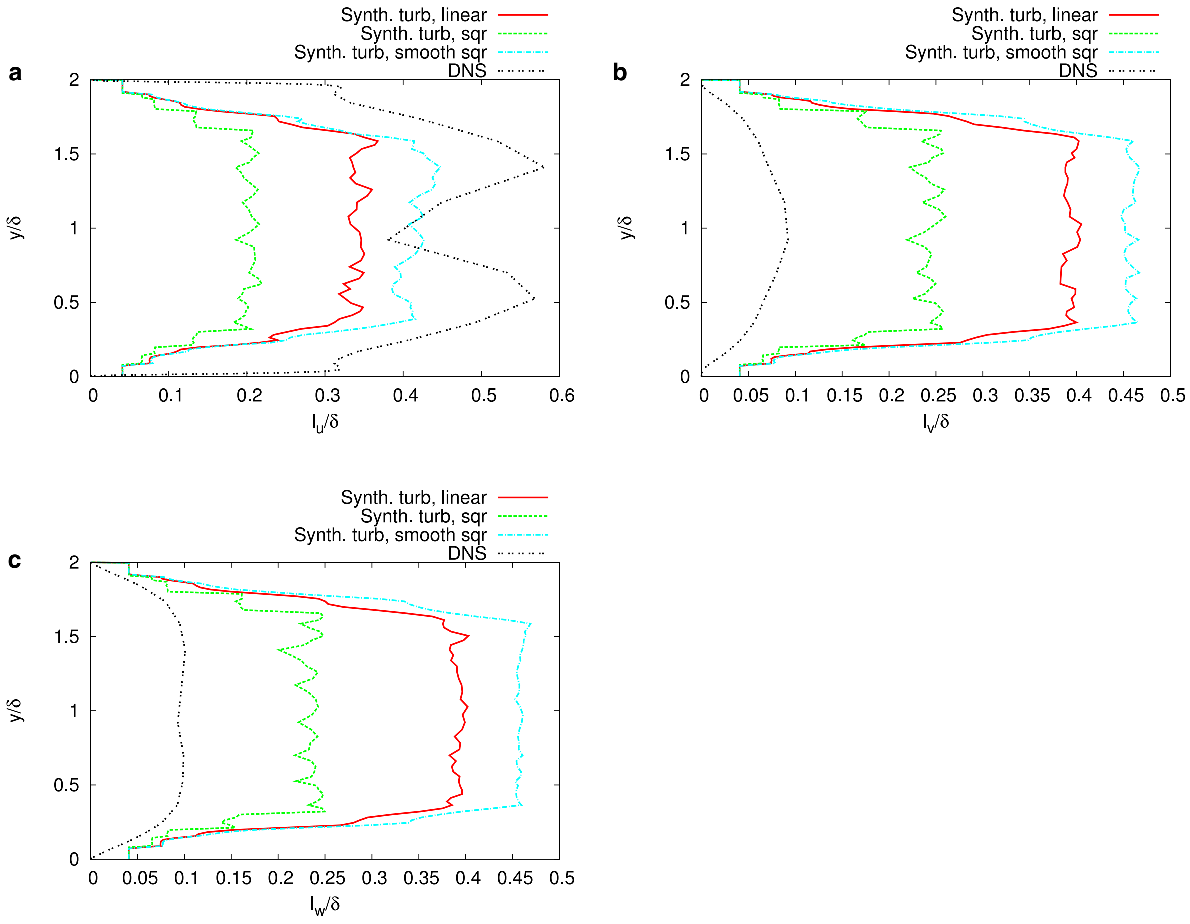

Fig. 8. Vertical profiles of the normalised integral length scales of (a) *u*, (b) *v* and (c) *w* in *z*-direction estimated from the DNS data (black, double dotted) and calculated from the synthetic turbulence with linear interpolation (red, line), square (green, dashed) and smooth square (blue, dot-dashed). (For interpretation of the references to colour in this figure legend, the reader is referred to the web version of this article.)

For comparison the integral length scales from the DNS data are plotted in green, dashed. The reason is that for each point in the $y - z$-plane synthetic turbulence in *x*-direction is generated independently from the synthetic turbulence at other points in the $y - z$-plane. Therefore the size of the turbulent eddies is very small in *y*- and *z*-direction.

3.3. Results from the extended turbulence generator

In this section results for the synthetic turbulence at the inlet plane of the channel generated by the synthetic turbulence generator are presented where the generator was extended to provide larger length scales in *y*- and *z*-direction. This was achieved by skipping a certain number of grid points in *y*- and *z*-direction on which the synthetic turbulence was not generated, depending on the integral length scales estimated from the DNS data. The turbulent signal from the grid points on which the synthetic turbulence was generated was interpolated to create a turbulent signal for the grid points which were skipped, originally. In the following the data set in which grid points were skipped will be addressed as being on the ‘coarse grid’ and the field containing all the turbulence data, including the interpolated one, as being on the ‘fine grid’. However it is not necessary to literally use different grids, since grid points on the grid in use are simply skipped for the generation of the turbulence. Like in the previous section synthetic turbulence fields for 12,000 timesteps were calculated.

Results from the three different interpolation methods from Eqs. (14), (16) and (19) are compared. Below the three cases will be called ‘linear’, ‘squares’ and ‘smooth squares’, respectively. First, an example for the interpolation of *u* in *y*-direction is shown in Fig. 5 to give an impression of how the different interpolation methods work. For this example a vertical profile for the *x*-component of the velocity was chosen at a random position in *z*-direction. The red line shows the values on the coarse grid while the interpolated values on the fine grid are depicted in green, dashed. In Fig. 5(a) the linear interpolation is shown where the values between two points of the coarse grid are assumed to follow a linear trend. Fig. 5(b) shows the interpolation of the squares of the velocities, where the interpolated velocity value is assigned the sign of the next velocity value on the coarse grid. It can be seen that when the velocity on the coarse grid changes its sign there are discontinuities occurring in the interpolated velocity values. In Fig. 5(c) the interpolated curve is much smoother. Here the squared velocities are assigned the sign of the velocities before the interpolation is performed. This way discontinuities are avoided when the velocities change sign on the coarse grid.

As discussed in Section (2.2), the interpolation of the velocity field, applied in the extension of the turbulence generator, causes deviations in the statistics of the synthetic turbulence from the

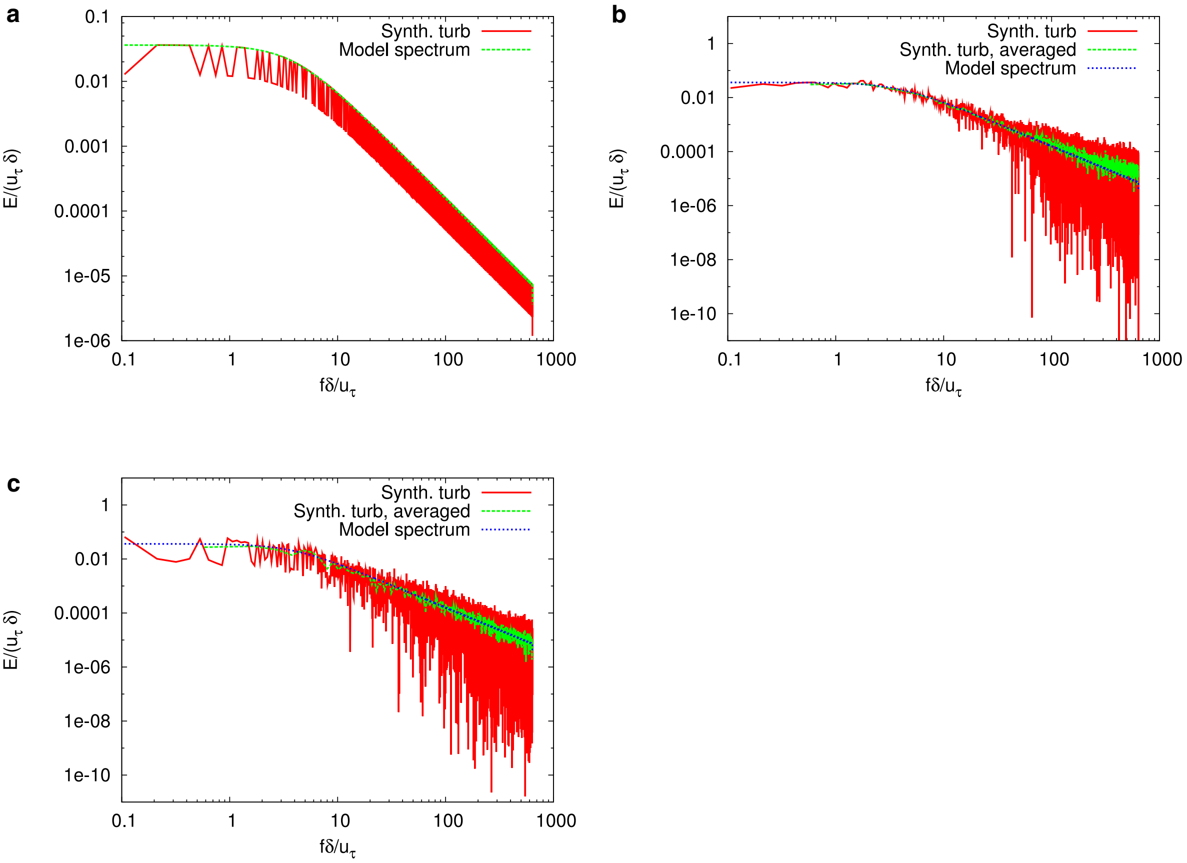

Fig. 9. Normalised 1D-spectra for u from synthetic turbulence (red, line) and from the model spectrum (green,dashed) for (a) linear, (b) square and (c) smooth square interpolation at $y/\delta = 0.47$ averaged over z. (For interpretation of the references to colour in this figure legend, the reader is referred to the web version of this article.)

input statistics. Fig. 6 shows how the different interpolation types affect the vertical profiles of the covariances. The prescribed covariances are shown in lines and the covariances from the synthetic turbulence are shown using symbols. In Fig. 6(a) strong deviations from the prescribed covariances can be seen for the linear interpolation method. The values near the wall fit very well, since no interpolation is performed there. Due to the small integral length scales prescribed near the wall no grid points on the fine grid are skipped. But in the region between 0.07 δ and 1.9 δ, where the integral length scales become larger and grid points are skipped to account for those length scales, the values for all covariances from the synthetic turbulence are much smaller than the prescribed ones.

For the square interpolation, shown in Fig. 6(b), the variances are matched very well for all three velocity components. Also the covariance of u and v is matched well even though there are some larger deviations. Fig. 6(c) shows the covariances for the smooth square interpolation. Here larger deviations from the input profiles for the variances as well as for the covariance of u and v are observed than in the profiles of the square interpolation method. The larger deviations in the variances are caused by the modification in the interpolation. In this case it was not a linear interpolation of the squares of the velocity but of the squares with the respective signs of the velocity values. Therefore, in those parts where the sign of the velocity values change, the interpolated value is not equal to the value of the linear interpolation of the squares without the signs of the velocities. Since only the latter guarantees a linear interpolation of the variances, deviations occur in the smooth square method. However, the deviations in the smooth square method are significantly smaller than in the linear method. The deviation in the covariance of u and w is a larger in the smooth square method than in the square method. Table 1 summarises the deviations of the absolute values of the covariance from the synthetic turbulence from the absolute values of the DNS data in percent. The deviations were only calculated in the interval in y-direction where interpolation was performed and then averaged over y. The perfect match in all components of the covariance which is obtained with the synthetic turbulence without extension (Fig. 1) is not achieved by any of the interpolation methods.

Table 1
Mean deviation of the absolute values of the covariances from the synthetic turbulence from the DNS data in percent.

	Δ_{uu}	Δ_{vv}	Δ_{ww}	Δ_{uv}
lin	51.0%	51.9%	51.3%	55.7%
sqr	5.9%	3.5%	3.9%	24.3%
sqr smooth	21.4%	22.7%	21.8%	34.9

The integral length scales in x-direction for all three velocity components, shown in Fig. 7, are similar for all three methods. They all fit the estimated integral length scales from the DNS quite well. The integral length scales from the square interpolation are a bit smaller than for the linear and the smooth square interpolation methods and also show more wiggles then the other methods. In general the integral length scales in x-direction from the synthetic

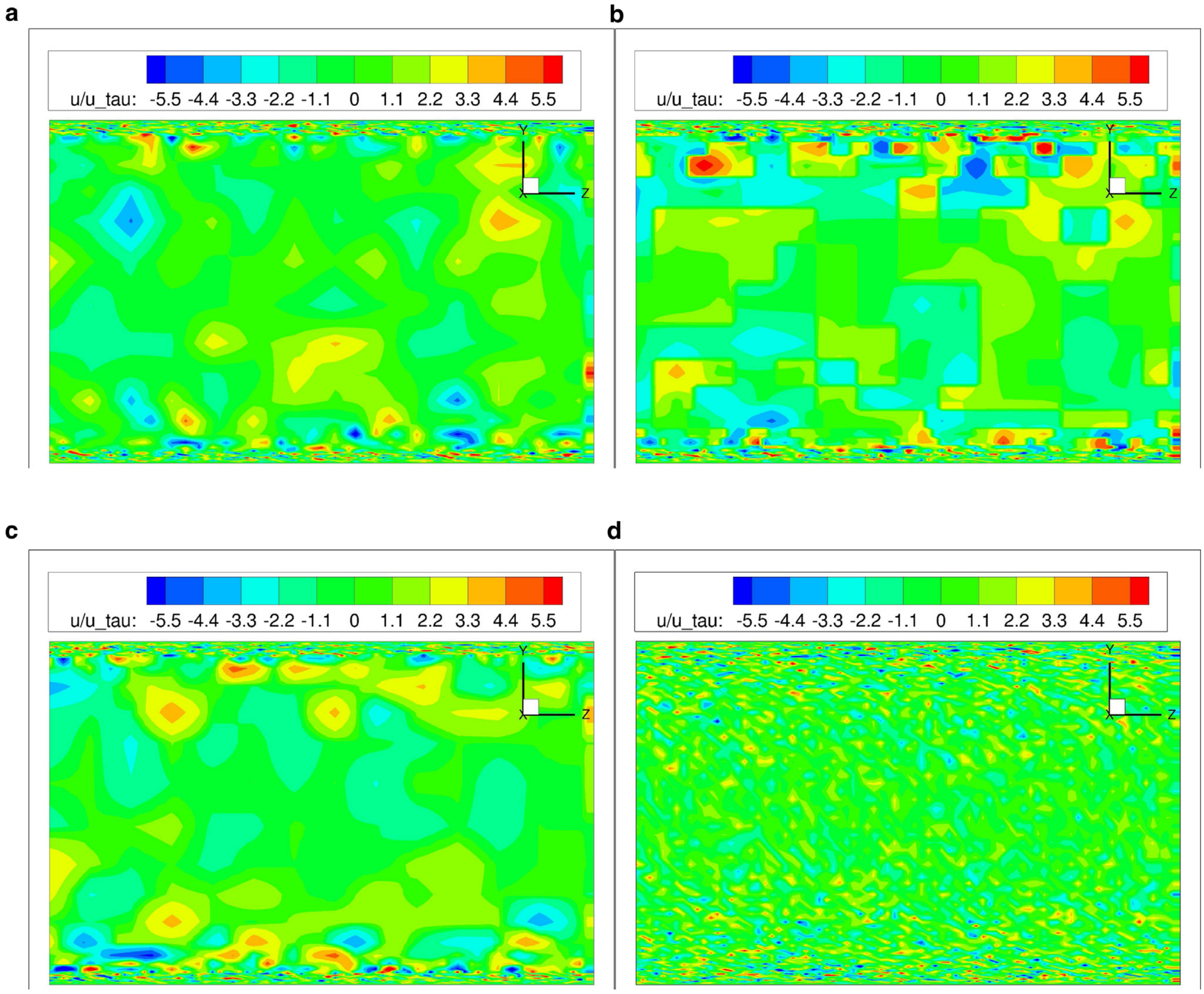

Fig. 10. Contour plot of u/u_τ in the y-z-plane for one time step from the synthetic turbulence for (a) linear, (b) square, (c) smooth square interpolation and (d) without interpolation. (For interpretation of the references to colour in this figure legend, the reader is referred to the web version of this article.)

turbulence without extension is very similar but smoother (cf. Fig. 3).

In the integral length scales in z-direction a significant difference can be seen between the synthetic turbulence without extension (Fig. 4) and with extension (Fig. 8) (the presented profiles are averaged over 50 realisations of the respective synthetic turbulence). While the integral length scales in z-direction from the synthetic turbulence without extension were all of the size of the grid spacing in z-direction, the integral length scales from the synthetic turbulence with extension varies over the channel height, exhibiting small values near the walls and higher values in the middle of the domain. The integral length scale from the DNS for w (black, double dotted in Fig. 8) was used to determine the coarser grid on which the synthetic turbulence was generated. The integral length scales for w from the synthetic turbulence are larger than those from the DNS. The largest values are reached by the smooth square interpolation. The linear interpolation gives slightly smaller values, and the values in the square interpolation are about half of those from the smooth square interpolation. For u the linear and the smooth square interpolation give values in a similar order of magnitude as the estimates from the DNS data. For v and w the profiles for the linear and smooth square interpolation are about a factor of 4 larger, and the profile for the square interpolation is about a factor of 2 larger than the estimates from the DNS data. Overall the extension of the turbulence generator provides a more realistic shape of the profiles and leads to an increase in the integral length scale in y- and z-direction.

In Fig. 9 the 1D-spectra in x-direction are shown for the three different interpolation methods. It can be seen that for the linear interpolation (Fig. 9, a) the spectrum follows the prescribed model spectrum like in the case of the synthetic turbulence without extension (Fig. 2). However for some frequencies the energy is smaller than in the prescribed model spectrum, creating frequent drops in the spectrum. This is caused by the deviations from the prescribed Reynolds stresses shown in Fig. 6. In Fig. 9(b) the spectrum for the square interpolation is shown. It is much noisier than the spectrum for the synthetic turbulence without extension and the spectrum for the linear interpolation. In order to smooth the noise an average over intervals of 20 wavenumbers was applied. It shows that the averaged spectrum follows the prescribed model spectrum for most parts of the frequency range. However, in the large frequencies an increase in energy can be observed. This increase is caused by the additional fluctuations introduced by the square interpolation due to the discontinuities when the velocity changes its sign. The spectrum from the smooth square interpolation looks similar to the one from the square simulation. But

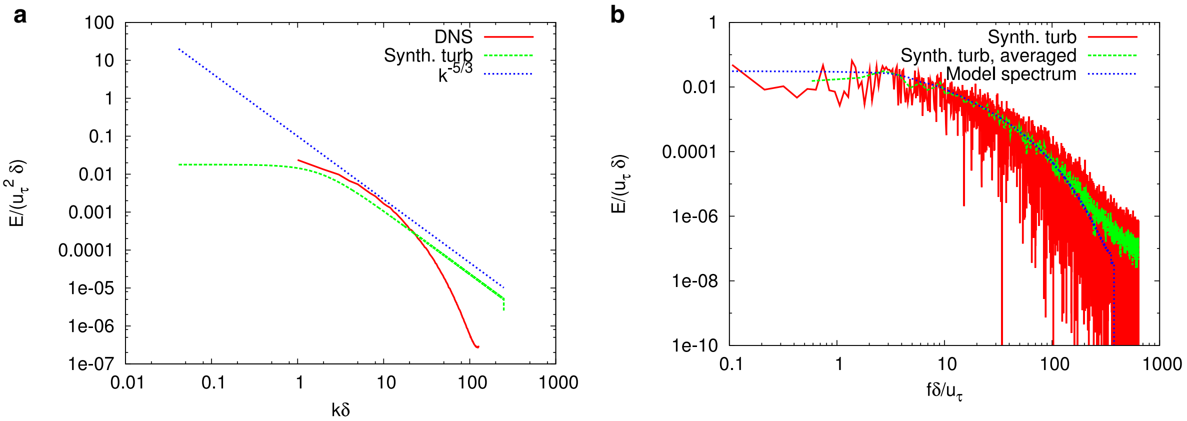

Fig. 11. (a) Normalised energy spectrum in x-direction for u from the DNS (red, solid line) compared to the model spectrum (green, dashed). For comparison the $k^{-5/3}$ slope of the inertial subrange is shown in blue (dotted). (b) Normalised energy spectrum from the synthetic turbulence when using the model spectrum derived from the DNS (red, solid line), spectrum from synthetic turbulence averaged over intervals of 20 wavenumbers (green, dashed) and model spectrum derived from the DNS (blue, dotted) at $y/\delta = 0.47$ averaged over z. (For interpretation of the references to colour in this figure legend, the reader is referred to the web version of this article.)

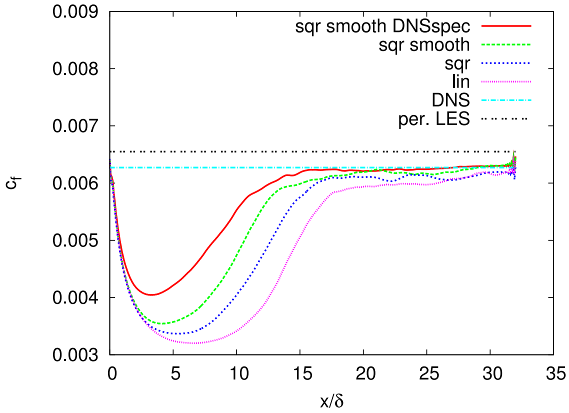

Fig. 12. Time and span averaged skin-friction coefficient along the channel from LES with synthetic turbulence using linear (pink, dotted), square (blue, short dashed) and smooth square (green, dashed) interpolation. Additionally, the result for the run with smooth square interpolation and DNS-spectra is depicted in red (solid line). For comparison the c_f value from the DNS and periodic LES is shown in light blue (dash-dotted) and black (double dotted), respectively. (For interpretation of the references to colour in this figure legend, the reader is referred to the web version of this article.)

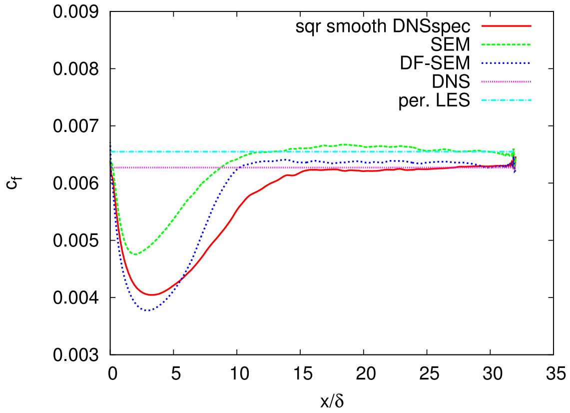

Fig. 13. Comparison of the time and span averaged skin-friction coefficient along the channel from LES with synthetic turbulence using smooth square interpolation and the DNS spectra (red, solid line), SEM and DF-SEM. For comparison the c_f value from the DNS (pink, dotted) and the periodic LES (light blue, dash-dotted) is shown. (For interpretation of the references to colour in this figure legend, the reader is referred to the web version of this article.)

due to the absence of discontinuities in the velocities there is no increase in energy in the large frequencies. This spectrum follows the model spectrum better than the one from the square interpolation. In all three cases the interpolation leads to deviations from the model spectrum and therefore also from the spectrum computed from the synthetic turbulence without extension.

In an instantaneous contour plot of u in a $y - z$-plane from the synthetic turbulence generator with extension (Fig. 10, a-c) it can be seen that, unlike in the version without extension (Fig. 10, d), the turbulent eddies become larger in y- and z-direction towards the middle of the domain. For the linear and smooth square interpolation method the field looks very similar and smooth. However, the velocity field from the square interpolation looks very unnatural and shows a lot of sharp edges due to the discontinuities introduced by the linear interpolation of the squares. The consequences of the differences between the different interpolation types are investigated in the next chapter where LES results from a channel flow for all three interpolation types are compared.

3.4. Application to LES of the channel flow

Based on the simulation setup described in Section 3.1, Large-Eddy Simulations of the plane channel flow at $\mathrm{Re}_\tau \approx 395$ were performed using the extended synthetic turbulence generator with the three interpolation methods described in Section 2.2. Note that the model spectra used for the synthetic turbulence are designed for high Reynolds numbers. Since the channel flow only has a bulk Reynolds number of about 7000 the model spectra do not match the real spectra very well (Fig. 11a compares the model spectra with the spectra calculated from the DNS of Moser et al., 1999). Therefore, a fourth simulation was performed using the actual spectra from the DNS. Since the DNS spectra can not resolve the largest scales, the spectral energy was simply considered to be constant from the lowest frequency resolved by the DNS onwards (see Fig. 11b). The results in this section are compared to the DNS data and an LES with periodic boundary conditions.

A measure for the performance of synthetic turbulence is the adjustment length of the channel flow downstream of the synthetic inlet plane. It indicates which distance it takes the flow to

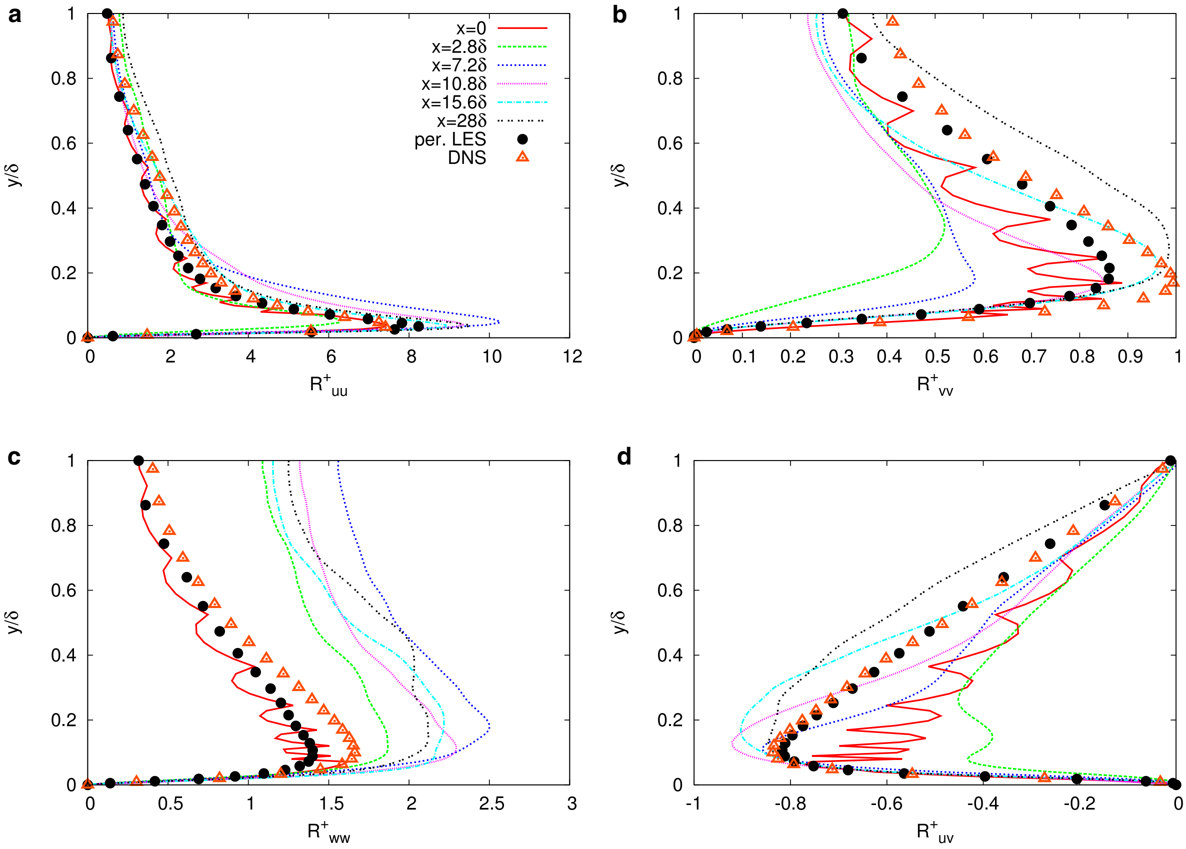

Fig. 14. Profiles of normalised Reynolds stresses for the components R^+_{uu} (a), R^+_{vv} (b), R^+_{ww} (c) and R^+_{uv} (d). Depicted are the results for the Reynolds stresses from the LES at the inlet of the channel (red, solid line), at 2.8 δ (green, long dashed), 7.2 δ (blue, short dashed), 10.8 δ (pink, dotted), 15.6 δ (light blue, dot-dashed), 28 δ (black, double dotted). The results from the DNS and periodic LES are shown as orange triangle and black dots, respectively. For better visibility only every second data point from the DNS and periodic LES is shown. The legend in (b), (c) and (d) is the same as in (a). (For interpretation of the references to colour in this figure legend, the reader is referred to the web version of this article.)

develop realistic turbulence. Often this is measured in terms of the skin-friction coefficient c_f at the channel wall since it is influenced by the Reynolds stress distribution in the flow. Fig. 12 shows the time- and spanwise-averaged skin-friction coefficient over x for all four simulations. In all four cases an immediate drop of c_f can be noticed right after the synthetic turbulence enters the channel. Depending on the interpolation type it takes different distances to recover to a constant value. The worst performance is shown by the linear interpolation. This was expected since the deviation of the Reynolds stresses was the largest in this case. It takes the turbulent flow around 18 δ to return to a more or less constant value. That value is reached at about $c_f = 5.9 \times 10^{-3}$ (slightly increasing until the end of the channel), which is lower than the reference value of $c_f = 6.55 \times 10^{-3}$ from the periodic LES. For the interpolation of the squares an improvement of the results can be noticed. The drop in c_f is less pronounced and the distance to recover to a constant c_f is less than in the case of the linear interpolation. A constant value is reached after about 17 δ and with $c_f = 6.1 \times 10^{-3}$ the value is closer to the reference value. Apparently, the strong gradients visible in the $y - z$-plane in Fig. 10 (b) are not disadvantageous for the simulation, when comparing to the results from the linear interpolation. It could also be that a potential negative effect of the strong gradients is compensated by a much better agreement in the covariances, compared to the linear interpolation. A further improvement can be seen when using the smooth interpolation of the squares. The drop in c_f is even less pronounced than in the square interpolation. The adjustment length is about 16 δ and the constant value of c_f is slightly larger than for the square interpolation. This improvement might be due to the smoother flow field, but it could also be caused by the larger integral length scales in z-direction which might compensate the slightly worse agreement in the covariances. However, the best result is achieved when using the smooth square interpolation with the energy spectra from the DNS as input for the synthetic turbulence. Those spectra are better suited for the low Reynolds numbers in the channel flow, and therefore a further improvement over the simulation with the smooth square interpolation and the model spectra can be observed. The adjustment length is now reduced to about 15 δ and a constant value of skin-friction is reached at around $c_f = 6.25 \times 10^{-3}$ which is almost identical with the result of the DNS but is still lower than the reference value from the periodic LES.

Since the synthetic turbulence with the smooth square interpolation using the original DNS spectra gave the best results further analysis is only done for this simulation. A comparison of the development of c_f along the channel for the present method with the synthetic-eddy method (SEM, Jarrin et al., 2006) and the divergence-free synthetic-eddy method (DF-SEM, Poletto et al., 2011) can be seen in Fig. 13. The simulations for the SEM and DF-SEM were conducted with the same mesh and parameter settings in TAU as the simulations using the presented synthetic turbulence method. In the comparison of the c_f value it can be

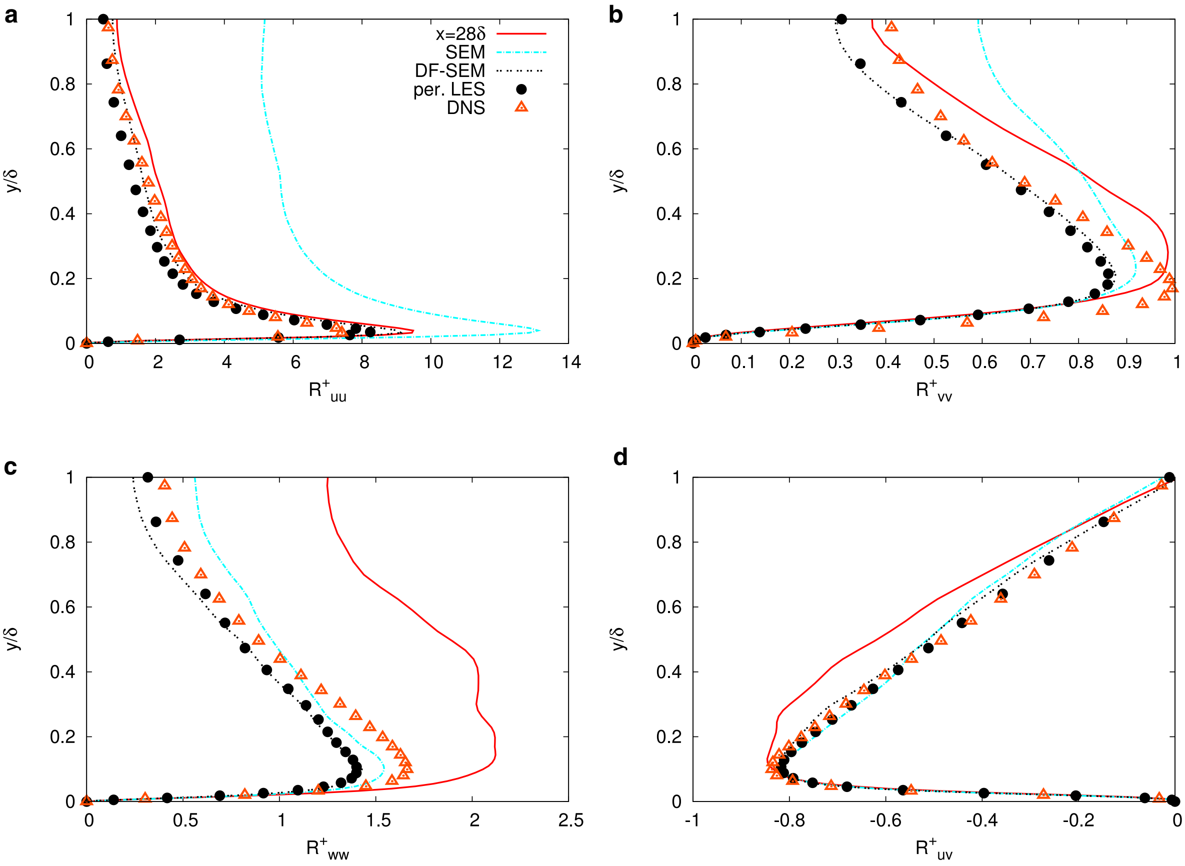

Fig. 15. Profiles of normalised Reynolds stresses for the components R^+_{uu} (a), R^+_{vv} (b), R^+_{ww} (c) and R^+_{uv} (d). Depicted are the results for the Reynolds stresses from the LES using the present method at 28 times the channel half height (red, solid line). For comparison the results of the LES at 28 times the channel half height using SEM (light blue, dot-dashed) and DF-SEM (black, double dotted), as well as the results from the periodic LES (black dots) and DNS (orange triangles) are shown. For better visibility only every second data point from the DNS and periodic LES is shown. The legend in (b), (c) and (d) is the same as in (a). (For interpretation of the references to colour in this figure legend, the reader is referred to the web version of this article.)

seen that, out of the three methods, the SEM performs the best. The initial drop in c_f is significantly less than in the other two methods and with around 10 δ the adjustment length is similar to the DF-SEM and shorter than in the present method. It also recovers to a higher value of c_f. While in the case of the present method and the DF-SEM the c_f value recovers to the value of the DNS, the SEM recovers to the slightly higher value of the periodic LES, which should be the reference value for this simulation.

In Fig. 14 the components R^+_{uu} (a), R^+_{vv} (b), R^+_{ww} (c) and R^+_{uv} (d) of the normalised Reynolds stresses are shown. The figure compares the Reynolds stresses from the DNS and periodic LES with profiles from the LES with synthetic turbulence using the smooth square interpolation and the DNS spectra at several different locations along the channel. As already shown in Fig. 6 (c) the Reynolds stresses from the synthetic turbulence at the inlet fit the Reynolds stresses from the DNS quite well. However, due to the smooth square interpolation the absolute values are a bit smaller than those from the DNS making them fit better with the profiles from the periodic LES. For the shear stress a significant difference with both the DNS data as well as the periodic LES data can be seen at the inlet.

The *uu*-component of the Reynolds stress near the wall initially decreases in the section of the channel where c_f is dropping (represented by the profile at 2.8 δ). After the minimum is reached and the values of c_f are increasing a rise in R_{uu} can be observed near the wall which leads to Reynolds stresses exceeding those from the DNS and periodic LES. Towards the region where c_f is constant R_{uu} is decreasing and stabilises at around 15 δ reaching values close, but slightly larger, than those from both the DNS and the periodic LES. For R_{vv} the values near the wall are increasing throughout the channel reaching values close to the profiles of the DNS and periodic LES at around 15 δ. Small differences are visible between the profiles at 15 δ and 28 δ. In the profiles of R_{ww} big differences between the LES with synthetic turbulence and the profiles from the DNS and the periodic LES are visible throughout the domain. Even in the first part of the channel R_{ww} already increases significantly and reaches a maximum at around 7.2 δ. After that it decreases slightly reaching values which are still significantly larger than the reference profiles. For the shear stress an initial decreasing of the absolute value of R_{uv} can be seen until c_f reaches its minimum. After that the absolute value of the shear stress increases reaching values slightly larger than the reference profile.

To evaluate the performance of the presented synthetic turbulence method, in Fig. 15 the Reynolds stress profiles at $x = 28$ δ are compared to the profiles from the LES using SEM and DF-SEM, respectively. For R_{uu} a very good fit can be seen in both the present method and the DF-SEM. However the profile from the SEM shows significantly larger values. In the profiles of R_{vv} again the DF-SEM shows a very good fit with the reference profiles, while the present method shows values slightly larger than the periodic LES. The

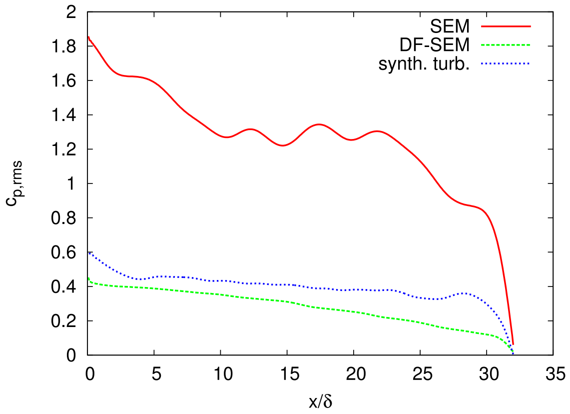

Fig. 16. Root mean square of the pressure coefficient for the LES with SEM (red, solid line), DF-SEM (green, dashed) and the present method (blue, dotted). (For interpretation of the references to colour in this figure legend, the reader is referred to the web version of this article.)

profile from the SEM shows a better fit closer to the wall but towards the middle of the channel the values are significantly larger than for both the DF-SEM and the present method. For the *ww*-component a much better performance of the SEM and DF-SEM can be seen, compared to the present method. While the present method produces values of R_{ww} much larger than in the reference, the profiles of the SEM and DF-SEM are in good agreement with the reference. The DF-SEM again has a better fit than the SEM. Regarding the shear stress all three methods show good agreement with the reference profile with the profile of the present method deviating more than those of the SEM and DF-SEM.

The most notable deviations in the comparison of the Reynolds stresses were observed for the present method in the *ww*-component, and for the SEM in the *uu*-component. Although it is difficult to identify the reason for these deviations, they might be caused by pressure fluctuations due to sound waves in the domain which result from the divergence of the velocity field at the inlet. In Fig. 16 the root mean square of the pressure coefficient along the channel is shown for the present method, the SEM and the DF-SEM. It can be seen that the SEM introduces much larger pressure fluctuations than the other two methods. However, due to the divergence-free formulation of the DF-SEM the pressure fluctuations are lower for the DF-SEM than for the present method. Further analysis would be necessary to investigate if there might be a connection between the pressure fluctuations and the significant deviations in R_{uu} for the SEM and R_{ww} for the present method.

4. Conclusions

The method by Auerswald and Bange (2015) for generating synthetic turbulence has been improved and tested in large-eddy simulations of a plane channel flow. The method uses an alternative approach for generating anisotropic profiles of the Reynolds stresses. Unlike the widely used Cholesky decomposition this approach does not change the other turbulence statistics. While the original method for generating the synthetic turbulence was able to reproduce the given input statistics with very high precision it lacked control over the length scales in *y*- and *z*-direction. The turbulence in *y*- and *z*-direction was uncorrelated which led to unrealistically small length scales in these directions.

To improve the length scales and generate turbulence on more realistic scales an extension to the turbulence generator was introduced. By generating the turbulence not on all grid points but skipping a certain number of grid points in *y*- and *z*-direction, depending on the length scales in the respective directions, larger and more realistic length scales could be generated. For interpolating the generated synthetic turbulence on the skipped grid points, three different interpolation methods (linear, square and smooth square) were tested, and the resulting turbulence was studied. Even though deviations in the energy spectrum and the covariances could be seen for all three interpolation types (to different extends), the improvement of the statistics in *y*- and *z*-direction improved the quality of the synthetic turbulence significantly.

In LES of the turbulent channel flow overall satisfying results were achieved, although a dependency of the simulation on the synthetic turbulence statistics was observed. Using the original DNS spectra clearly reduced the transition length to fully-developed turbulence and improved the behaviour of the skin-friction. The linear interpolation method with its large deviations from the given Reynolds stress profiles performed the worst. The differences in the skin-friction coefficient between the square and the smooth square interpolation may be due to the differences in the integral length scales. The results clearly show a dependency of the results on the statistical properties of the synthetic turbulence.

The present method could not perform as well as the SEM and DF-SEM in terms of adjustment length. In terms of the value of c_f similar results to the DF-SEM were achieved but the SEM was closer to the c_f value of the periodic LES.

In the comparison of the three methods with respect to the Reynolds stress profiles, good agreements with the reference simulation were seen in all three methods, even though the DF-SEM was clearly fitting the best. The simulation using the SEM had large deviations from the reference profile in the *uu*-component of the Reynolds stress tensor while the present method had large deviations in the *ww*-component. It is not clear what causes these deviations but it might be related to pressure fluctuations due to the divergence of the velocity at the inlet plane.

Even though the present method could not show a better fit with the periodic LES than the SEM and DF-SEM in the simulation of the channel flow, it provides an improvement in terms of flexibility. It allows to control a larger number of statistical parameters (1D energy spectrum in *x*-direction, normal and shear stresses, length scales in *x*-, *y*- and *z*-direction of *u*, *v* and *w*) independently, which could be an advantage given the observed sensitivity of the simulation results to the prescribed statistics. Furthermore, the flexibility of the new method was not exploited to the fullest extent. Simulation results could possibly be improved if the input statistics would be adjusted to compensate for the deviations introduced by the interpolation, and length scales for the velocity components in *y*- and *z*-direction could be set independently. In the present study no effort was taken towards that. Furthermore, better simulation results might also be achieved if the input statistics for the synthetic turbulence generator would be taken from the periodic LES instead of the DNS, since these are the statistics that are expected to develop in the simulation.

In future studies this method could be used to further investigate the dependency of the simulation results on the statistics of the inflowing turbulence, since it allows to systematically change single statistical parameters independently from the others. That way more insight into the relevance of different statistical parameters for the synthetic turbulence and how to choose them properly could be obtained. Further analysis on the comparison to the SEM and DF-SEM would also be necessary. Since in the SEM and DF-SEM, only the Reynolds stresses and length scales can be prescribed, an analysis of other statistical properties of the turbulence generated by the SEM and DF-SEM, similar to the one provided for the present method, would be insightful. In a comparison study the present method could be used to produce the same statistics like the SEM and DF-SEM and it could be investigated if the performance of the methods are similar with comparable turbulence statistics.

Acknowledgements

The authors acknowledge the support of the “Deutsche Forschungsgemeinschaft DFG” (German Research Foundation) which funded this research.

References

Adamian, D., Travin, A., 2011. An efficient generator of synthetic turbulence at ransles interface in embedded les of wall-bounded and free shear flows. In: Kuzmin, A. (Ed.), Computational Fluid Dynamics 2010. Springer Berlin Heidelberg, pp. 739–744.

Auerswald, T., Bange, J., 2015. A new method to generate anisotropic synthetic turbulence for LES. Simulation of Wing and Nacelle Stall, Notes on Numerical Fluid Mechanics and Multidisciplinary Design. Springer.

Batten, P., Goldberg, U., Chakravarthy, S., Batista de Jesus, A., 2012. Large eddy stimulation using simple eddy-viscosity rans data. In: Eberhardsteiner, J., Böhm, H.J., Rammerstorfer, F.G. (Eds.), CD-ROM Proceedings of the 6th European Congress on Computational Methods in Applied Sciences and Engineering (ECCOMAS 2012), September 10–14, 2012, Vienna, Austria.

Batten, P., Goldberg, U., Chakravarthy, S., 2004. Interfacing statistical turbulence closures with large-eddy simulation. AIAA J. 42 (3), 485–492.

Blazek, J., 2005. Computational Fluid Dynamics: Principles and Applications, Second ed. Elsevier.

Deardorff, J.W., 1970. A numerical study of three-dimensional turbulent channel flow at large reynolds numbers. J. Fluid Mech. 41, 453–480.

Ducros, F., Nicoud, F., Poinsot, T., 1998. Wall-adapting Local Eddy-Viscosity models for simulations in complex geometries. In: Proc. Conf. on Num. Meth. Fluid Dyn., Oxford, UK.

Jameson, A., 1991. Time dependent calculations using multigrid, with applications to unsteady flows past airfoils and wings. AIAA 91-1596.

Jarrin, N., Benhamadouche, S., Laurence, D., Prosser, R., 2006. A synthetic-eddy-method for generating inflow conditions for large-eddy simulations. Int. J. Heat Fluid Flow 27 (4), 585–593. Special Issue of The Fourth International Symposium on Turbulence and Shear Flow Phenomena - 2005 Special Issue of The Fourth International Symposium on Turbulence and Shear Flow Phenomena - 2005

Jarrin, N., Prosser, R., Uribe, J.-C., Benhamadouche, S., Laurence, D., 2009. Reconstruction of turbulent fluctuations for hybrid rans/les simulations using a synthetic-eddy method. Int. J. Heat Fluid Flow 30, 435–442.

Kamruzzaman, M., Lutz, T., Herrig, A., Krämer, E., 2012. Semi-empirical modeling of turbulent anisotropy for airfoil self-noise predictions. AIAA J. 50 (1), 46–60.

Keating, A., Piomelli, U., 2004. Synthetic generation of inflow velocities for large-eddy simulation. 34th AIAA Fluid Dynamic Conference and Exhibit, 28 Jun–1 Jul 2004, Portland, Oregon.

Kok, J., 2009. A high-order low-dispersion symmetry-preserving finite-volume method for compressible flow on curvilinear grids. J. Comp. Phys. 228 (18), 6811–6832.

Kraichnan, R.H., 1970. Diffusion by a random velocity field. Phys. Fluids 13, 22–31.

Launder, B.E., Reece, G.J., Rodi, W., 1975. Progress in the development of a reynolds-stress turbulence closure. J. Fluid Mech. 68, 537–566.

Moser, R.D., Kim, J., Mansour, N.N., 1999. Direct numerical simulation of turbulent channel flow up to Re_τ=590. Phys. Fluids 11, 943–945.

Poletto, R., Revell, A., Craft, T.J., Jarrin, N., 2011. Divergence free synthetic eddy method for embedded les inflow boundary conditions. Seventh International Symposium On Turbulence and Shear Flow Phenomena (TSFP-7). Begell House Inc.

Probst, A., Reuß, S., 2015. Scale-resolving simulations of wall-bounded flows with an unstructured compressible flow solver. Progress in Hybrid RANS-LES Modelling. Notes on Numerical Fluid Mechanics and Multidisciplinary Design, Springer International Publishing, Vol. 130.

Radespiel, R., Turkel, E., Kroll, N., 1995. Assessment of Preconditioning Methods. Technical Report DLR-FB 95-29.

Schwamborn, D., Gerhold, T., Heinrich, R., 2006. The DLR TAU-Code: recent applications in research and industry. In: Wesseling, P., Oñate, E., Périaux, J. (Eds.), ECCOMAS CFD. TU Delft, The Netherlands.

Shur, M.L., Spalart, P.R., Strelets, M.K., Travin, A.K., 2014. Synthetic turbulence generators for rans-les interfaces in zonal simulations of aerodynamic and aeroacoustic problems. Flow Turbul. Combust. 93 (1), 63–92.

Smirnov, A., Shi, S., Celik, I., 2001. Random flow generation technique for large eddy simulations and particle-dynamics modeling. J. Fluids Eng. 123, 359–371.

Spalart, P.R., Allmaras, S.R., 1992. A one-equation turbulence model for aerodynamic flows. AIAA, Aerospace Sciences Meeting and Exhibit, 30th.

Spalart, P.R., Jou, W.-H., Strelets, M., Allmaras, S.R., 1997. Comments on the feas1ibility of les for wings, and on a hybrid rans/les approach. In: Proceedings of First AFOSR International Conference on DNS/LES.

Swanson, R.C., Turkel, E., 1992. On central-difference and upwind schemes. J. Computat. Phys. 101, 292–306.